Axialisation of Particles in a Penning-type Trap by the Application of a Rotating Dipole Electric Field and its Application to Positron Accumulation

Christopher Aled Isaac MPhys

Submitted to Swansea University in fulfilment of the requirements for the Degree of
Doctor of Philosophy

Swansea University
Prifysgol Abertawe

2010

Declarations and Statements

Declaration

This work has not previously been accepted in substance for any degree and is not being concurrently submitted in candidature for any degree.

Signed .... (candidate)

Date ....

Statement 1

This thesis is the result of my own investigations, except where otherwise stated. Where correction services have been used, the extent and nature of the correction is clearly marked in a footnote(s).

Other sources are acknowledged by footnotes giving explicit references. A bibliography is appended.

Signed .... (candidate)

Date ....

Statement 2

I hereby give consent for my thesis, if accepted, to be available for photocopying and for inter-library loan, and for the title and summary to be made available to outside organisations.

Signed .... (candidate)

Date ....

Abstract

An experimental and theoretical study of the behaviour of particles in a 2-stage buffer gas accumulator has been undertaken. A mathematical model has been developed for the axialisation of a particle in a Penning-type trap via the asymmetric application of a rotating dipole electric field in the presence of a cooling mechanism which conforms to a Stokes' viscous drag form. This model has been compared with experimental results obtained using a 4-segment electrode installed in a 2-stage N_2 buffer gas positron accumulator with the addition of SF_6 cooling gas.

It was found that the application of the rotating wall electric field during the accumulation stage decreases the loss rate to a value consistent with the positron annihilation rate on the cooling gas, giving a 7-fold increase in the potential storage capability of the Swansea accumulator.

I Fam a Dad

Diolch am dy gariad a chefnogaeth diamod

Contents

List of Figures

List of Tables

Acknowledgements

I feel that I owe the greatest thanks to Ashley, without whom I have little doubt I would not have stuck at the PhD. I have not always been the easiest to live with, and yet he has continued to show me love and support throughout not only my PhD, but also my undergraduate studies.

I am indebted to my many colleagues whom have helped me learn, maintain and use the Swansea positron beam-line. Firstly, Peter Watkeys whom introduced me to the basics on the system. Secondly, my thanks must go to Christopher Baker who taught me the most important lesson of all: 'While it works, use it, because it won't work for long'. I must also thank Serena Kerrigan whom I have had the pleasure of studying alongside since the start of my time at university. And finally the newest member of the positron group, Tim Mortensen, who has assisted in the taking of much of the data presented in this thesis. I am also grateful to the department technical staff, Mr Hugh Thomas and Mr Julian Kivell, for their their excellent technical skills which have aided in the development and maintenance of the equipment.

I would like to show my gratitude to Dr Richard Lewis for enduring my many rants during my PhD. It has also been nice to have someone to converse with in the language of our country.

I would like to thank Dr Dirk van der Werf whom I no longer consider only my supervisor but also a friend. When something in the lab stopped working, you could guarantee it would begin to work as Dirk entered the room; maybe this was magic, or the equipments attempt to make me look foolish.

I will be eternally grateful to Prof Michael Charlton for his support and encouragement. He delivered my very first lecture as an undergraduate and continues to inspire me to this day.

Finally, I would like to thank all of my friends whom have kept me moderately, or maybe slightly, sane over the years. I apologise that I cannot name you all individually, however, I hope that you all know how grateful I am.

Notation

$\mathbf{v}$	Vectors are given in bold typeface
$\hat{\boldsymbol{z}}$	Unit vectors are given using the hat notation
$\mathcal{M}$	Matrices are given in calligraphic typeface
$\dot{x}, \ddot{x}$	Derivatives with respect to time are given by the dot notation
a^*	Complex conjugates are denoted with the asterisk notation
$\mathrm{Re}[a]$	The real parts of a complex number
$\mathrm{Im}[a]$	The imaginary part of a complex number
$\angle\,[a]$	The angle of a complex number $\arctan(\mathrm{Im}[a]/\mathrm{Re}[a])$
$\lvert a \rvert$	Absolute values
(x, y, z)	Cartesian coordinates
(z, r, θ)	Cylindrical coordinates
$\mathbf{r}$	The radial vector $\mathbf{r} = x\hat{\boldsymbol{x}} + y\hat{\boldsymbol{y}}$
$\mathbf{i}$	The imaginary unit $(\sqrt{-1})$
$\exp(x)$	The Exponential function e^x
π	Pi 3.14159...
∇	The gradient operator
∇^2	The Laplace operator
∞	Infinity
$I_n(x)$	The modified Bessel function of the first kind of order n, argument x
ϵ_0	The permittivity of free space
μ_0	The permeability of free space
k_B	The Boltzmann constant
e	The electron charge

Chapter 1

Introduction

“A new scientific truth does not triumph by convincing its opponents and making them see the light, but rather because its opponents eventually die and a new generation grows up that is familiar with it”

— *Max Plank (1948)*

Although speculations regarding the existence of an antimatter had existed previously, it was not until the unification of special relativity and quantum mechanics that it was realized that antimatter was a real entity. This subject has been in existence for around 90 years and yet it still holds a number of mysteries waiting to be solved. A great effort has been devoted to controlling antimatter; from humble beginings with the positron, e^+, to the now, more exotic positronium, Ps, antiproton, $\bar{p}$, and more recently antihydrogen, $\bar{\mathrm{H}}$. Modern antimatter related experiments can manipulate antiparticles using various techniques such as moderation, accumulation, rotating wall compression, bright beam formation and high field effects such as cyclotron cooling.

The studies presented in this thesis are concerned with just two of these: accumulation and rotating wall compression. Using these it will be shown that an increased yield of positrons in smaller clouds can be achieved with modest modifications to existing accumulators. To begin, an introduction is given into the history of antimatter physics along with some details on the recent and current interests of the Swansea positron group which have led to these studies, followed by an outline of the contents of this thesis.

1.1 Historical Background and Introductory Remarks

1.1.1 The antiworld

In Arthur Schuster's letter "Potential Matter – A Holiday Dream" [1] he postulates the existence of an antimatter as a source of antigravity. In this flight of fancy he predicts that his antiatoms would gravitationally repel matter and yet be indistinguishable from it. Despite this being accredited as the first time the idea of antimatter had ever been conceived, the gravitational interaction between matter and antimatter has yet to be measured. Although experiments to determine this are a little way off yet, inroads have been made into studying other differences and similarities between matter and antimatter.

The first prediction of the existence of antimatter came from Paul Dirac in 1931. While attempting to make a relativistic formulation of quantum mechanics he found negative solutions for the energy values for an electron [2]. In quantum mechanics such solutions cannot be neglected as unphysical and so he considered a sea of possible energy states, both positive and negative. The negative energy states would normally be occupied so that, by the Pauli exclusion principle, an ordinary electron of positive energy would be unable to fall into them.

Under normal circumstance the negative energy states would be unobservable, however Dirac questioned how one of these energy states would manifest itself were it to be unoccupied? He showed that such a hole would appear as a positive particle which he initially believed to account for the existence of the proton. A number of eminent physicists of the time pointed out that if that were the case then a proton would annihilate with an electron and atoms would self annihilate. Dirac conceded that his holes would be a new, as yet unobserved, particle which he termed the antielectron. Among his predictions for the properties of the antielectron were its stability in vacuum and a possible mechanism by which experimentalists could produce such a particle. He also concluded that the proton should also have these negative energy states and so antiprotons should also exist.

A little over two years later Carl Anderson published his paper entitled "The Positive Electron" in which he presented photographs showing cosmic ray tracks in a vertical Wilson chamber [3]. In some 1300 of the photographs he examined, he observed 15 tracks produced by a positive particle with a track length and curvature which was inconsistent with that of a proton, the only known positive particle at the time. Anderson was able to place experimental limits on the mass and charge of his newly discovered particles which suggested that they were of a comparable charge and mass to that of the electron. He gave his positive electrons the name positron and, by extension, he used the term negatron to refer to a free electron*. Later in 1933, Blackett and Occhialini realised that Anderson's positrons and Dirac's antielectrons were one and the same [4].

Stjepan Mohorovičić is credited with the prediction of the existence of the bound state of an electron and a positron. His 1934 paper was the first to show that the binding energy of a positron to an electron is half that of the binding energy of hydrogen [5]. The remainder of the work in this paper is a mis-guided attempt to use positrons and electrons to build a new table of elements, the first three of which he named electrum (Ec), nobelium (Nb) and slavium (Sl). Mohorovičić derived predicted emission spectra for these elements and tried to use them as an explanation for unidentified spectral lines in the emission spectra of some stars. It was not until 1945 that Arthur Ruark published a paper in which he put forward the now accepted name of positronium† [6]. By looking at the distribution of lifetimes of positrons in gas mixtures Martin Deutsch was able to provide the first definitive proof for the abundant formation of positronium [7].

In 1955 Chamberlain *et al.* were the first to observe the antiproton in an experiment [8]. They produced antiprotons by colliding high energy protons, accelerated by the Bevatron synchrotron, into a copper target with energies above

---

[*] The term 'negatron' was never adopted by the wider scientific community

[†] Positronium may be identified with Mohorovîčić's first isotope of electrum

4.3 GeV[‡]. Although this provided the final ingredient for the production of atomic antimatter, it was many of years before this goal was realised.

In 1996 CERN announced that the PS210 collaboration had successfully produced 11 antihydrogen atoms by colliding high energy antiprotons into a Xenon target [9]. The antiprotons collided with the Xenon nuclei with sufficient energy to create a positron–electron pair and, on occasion, the antiproton would capture the positron forming antihydrogen. This result was called into doubt when, in 1998, Blanford *et al.* reported the production of antihydrogen at the Fermilab antiproton accumulator [10]. The formation mechanism was identical to the PS210 experiment but the target was replaced with a hydrogen gas jet. They found a formation cross section of 1.12±0.14 pb which was consistent with the prediction of Bertulani and Baur [11]. The same calculation gives a prediction for the PS210 experiment of 671 pb while their experiment, if correct, gave a cross section of at least 6000 pb.

The $\bar{\mathrm{H}}$ produced using high energy antiproton beams was not suited to spectroscopic studies due to its high momentum and sparseness. In 2002 the ATHENA collaboration at CERN reported the production of 20,000 cold[§] antihydrogen atoms [12]. By forming a positron plasma and an antiproton cloud, they produced antihydrogen via the mixing of the two species in a so-called nested Penning trap, as illustrated in figure 1.1.

Cold antihydrogen antiatoms produced in this manner have the potential to be used for spectroscopic studies. The standard model of particle physics is underpinned by CPT symmetry; the laws of physics should be invariant under the simultaneous inversion of charge (C), parity (P) and time (T). In essence this means that matter and antimatter should be indistinguishable with the exception of mutual annihilation. Spectroscopic measurements of the 1S–2S transition of antihydrogen have the potential to offer the most precise test of CPT symmetry to date, however, prior to this antihydrogen must be trapped in a neutral atom trap. Lasers capable of cooling and trapping antihydrogen are not yet available and so magnetic traps are being developed. In a magnetic field gradient the

---

[‡] In older documentation the unit of energy GeV would be written as BeV (Billions of electron volts)

[§] The term cold, in this respect, refers to a low energy and momentum.

magnetic moment of an atom may align itself with the field; such atoms will tend toward regions of higher magnetic field and are thus called high-field seekers. If the magnetic moment of the atom is aligned opposite to the field it will tend toward regions of lower magnetic field and is therefore called a low-field seeker. As it is not possible to produce a magnetic maximum in free space, it is only possible to magnetically confine low-field seekers in all 3 spatial dimensions. For a magnetic trap with a well depth ΔB, only atoms with a kinetic energy less than $\mu_B \Delta B$, where in the case of ground state (anti)hydrogen μ_B is the Bohr magneton, will be trapped. Thus only ground state antihydrogen with a kinetic energy corresponding to a temperature of 0.67 KT^{-1} or lower has the potential to be trapped. One of the aims of the ALPHA [13] and ATRAP [14] collaborations, located at the antiproton Decelerator (AD) at CERN, is to first trap antihydrogen and subsequently to perform spectroscopic measurements of the energy levels.

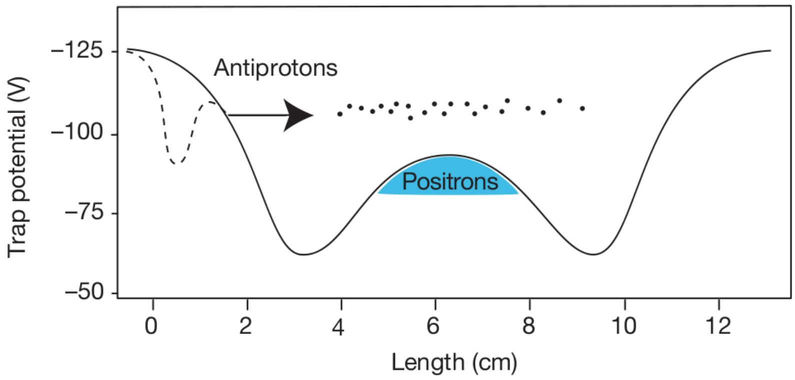

Figure 1.1: The mixing scheme used by the ATHENA collaboration. The trapping potential is plotted against length along the trap. The dashed line is the potential immediately before antiproton transfer. The solid line is the potential during mixing. This figure originally appeared in [12].

1.1.2 Manipulation of charged particle clouds

Inspired by the geometry of F.C. Penning's vacuum gauges, H.G. Dehmelt designed a trap capable of storing charged particles which he named the Penning trap [15]. In short, a Penning trap is a cylindrically symmetric trap which confines charged particles axially using a static electric field, and radially using a static magnetic field. In the radial plane the motion of such a trapped particle is described by the superposition of a fast circular motion which usually has a small radius, the cyclotron motion, and a slower circular motion with a larger radius, the magnetron motion. In the axial direction of the trap the particle exhibits simple harmonic motion termed an axial bounce motion. As the theory presented in chapter 3 will show, a particle in an ideal Penning trap may be confined indefinitely, however in reality small misalignments and imperfections of the electric and magnetic fields, as well as the vacuum quality, limit the confinement time. A number of methods have been developed to overcome these limitations, some of which are detailed here.

The cyclotron and axial motions of a particle in a Penning trap are relatively easy to damp, either by the use of a cooling gas or by cyclotron radiation in a strong magnetic field; the magnetron motion, on the other hand, is quasi-stable. In fact, as explained in section 3.1, the removal of energy from the magnetron motion actually increases the magnetron radius. Dehmelt showed that the normally decoupled motions of a charged particle in a trap become coupled by the use of superimposed fields at specific frequencies [16], for example, the radial expansion can be counteracted by the application of a field at the combined sum of the magnetron frequency and the axial bounce frequency [17]. Such a field will increase both the energy of the magnetron motion, and the energy of the axial bounce. It is therefore necessary to use one of the aforementioned methods to damp the axial motion.

If a sufficiently cold and dense cloud of charged particles is contained in a trap it is termed a non-neutral plasma. A plasma is defined as a many-body collection of charged particles which display a collective behaviour; that is, the interaction between the individual particles cannot be neglected. In the case of a conventional or neutral plasma such as an ionised gas, there is overall charge neutrality. On short length scales however, the ions and electrons may have a distribution such as to cause significant self-generated electric and magnetic fields and therefore exhibit collective behaviour. This allows for phenomenon such as plasma waves and instabilities. Collective behaviour is displayed in a plasma over a length scale characterised by the Debye length, λ_D, which is given by

$$\lambda_D = \sqrt{\frac{\epsilon_0 k_B T}{n e^2}}, \tag{1.1}$$

where T and n are the thermodynamic temperature and charge density of the plasma respectively. If a test charge were to be placed into a plasma, it is the Debye length which describes the characteristic distance over which the charge would be screened or shielded from the remainder of the plasma. For a collection of charged particles to display collective behaviour the dimensions of the cloud must be several Debye lengths.

When in a magnetic field, the self-generated electric field of a plasma will cause it to rotate as a result of a so-called E×B drift. In the zero temperature limit, a low density plasma in a magnetic field, B, will rotate as a rigid body at a frequency given by

$$f_r = \frac{ne}{2\pi\epsilon_0 B} \tag{1.2}$$

where n is the plasma density. In theory a non-neutral plasma in a penning trap will be confined indefinitely due to the conservation of angular momentum in a cylindrically symmetric trap [18], however analogous to the case of a single charged particle in a Penning trap, this is not in practice the case.

The compression of a non-neutral plasma was first demonstrated by the Driscoll group using magnesium ions [19] and, shortly after, using electrons [20]. In both experiments a split ring electrode was used to apply a "rotating wall" electric field asymmetrically over the plasma, achieving compression to densities in excess of 10^9 cm^{-3}. They observed that the compression rate exhibited peaks when the rotating wall frequency coincided with the Trivelpiece-Gould plasma modes[¶]. Although this method is effective in compressing non-neutral plasmas, it has the undesirable effect of heating the plasma. Greaves and Surko found that they were able to counteract this effect by the addition of a suitable cooling gas such as SF_6, CF_4 or CO_2 [22].

Using large amplitude rotating wall electric fields, coupled with a source of cooling, Danielson and Surko found that they were able to compress plasmas to

---

[¶] The Trivelpiece-Gould modes are space charge waves present in finite length plasmas [21].

densities in excess of 10^{10} cm^{-2}, not only at the specific frequencies previously observed, but over a whole range of frequencies. In this strong drive regime the plasma density would tend to a value such that the natural rotation frequency of the plasma, as given by equation 1.2, would equal the applied rotating wall frequency. Using this method Danielson and Surko were able to control their plasma densities simply by setting their rotating wall frequency [23].

Recently, Greaves and Moxom have published a paper entitled "Compression of trapped positrons in a single particle regime by a rotating electric field" [24]. In the experiment a cloud of charged particles was radially compressed in a Penning-type trap by the application of a rotating quadrupole electric field. Prior to this publication, only clouds of charged particles which qualified as plasmas had been compressed using this method. By applying the rotating wall asymmetrically over a cloud of positrons, compression was observed across a range of frequencies near the bounce frequency of the trap. As can be seen in Figure 1.2, at low rotating wall amplitudes compression occured over a narrow range of frequencies, while higher amplitudes resulted in compression occuring over a broad range of frequencies, extending below the bounce frequency of the trap. No compression was reported at frequencies above the bounce frequency. The authors suggested that the effects they observed may be explained in terms of the already understood effect of bounce resonance transport [25], however this theory is built on plasma equations and has not been developed for the single particle limit.

The studies presented in this thesis are of a similar nature to those performed by Greaves and Moxom, however using a rotating dipole electric field. Some preliminary results have been presented elsewhere [26, 27] however they represented a convoluted measurement in which the electric field was applied during the cloud formation (accumulation) stage. The current studies comprise a more direct measurement in which a true compression rate is measured and compared with a mathematical model of the compression mechanism.

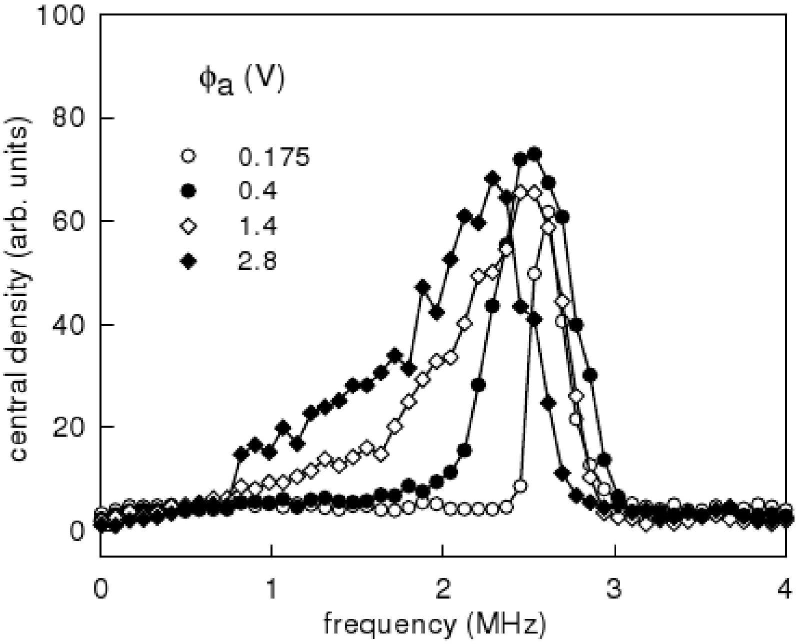

Figure 1.2: The frequency dependence of the central density as a function of applied rotating wall frequency for various amplitudes, ϕ_a, as measured by Greaves and Moxom [24].

1.2 Research Interests of the Swansea Positron Group

A major goal of the Swansea positron group is to investigate methods to produce positronium and study the Rydberg states to aid the ALPHA collaboration. An atom is considered to be in a Rydberg state if it has a high principal quantum number, n. Such atoms are particularly interesting because they have a number of novel properties, some of which are listed in table 1.1. It is believed that a highly efficient way to produce antihydrogen is via the charge exchange collision between an antiproton and positronium in a Rydberg state resulting in the creation of an antihydrogen atom and a surplus electron [28] as

$$\bar{\mathrm{p}} + \mathrm{Ps}^* \longrightarrow \bar{\mathrm{H}}^* + \mathrm{e}^-. \tag{1.3}$$

The cross section for this reaction scales as the orbital radius square, which from table 1.1, gives a n^4 dependence. In addition to this, the radiative lifetime of the positronium in the Rydberg states goes as n^3 and thus will offer a longer time-scale for the reaction to occur.

Table 1.1: A selection of properties of Rydberg atoms [29].

Property	n dependence
Binding energy	n^{-2}
Energy between adjacent n states	n^{-3}
Orbital radius	n^2
Geometric cross section	n^4
Dipole moment	n^2
Polarizablility	n^7
Radiative lifetime	n^3
Fine-structure interval	n^{-3}

1.2.1 Laser-Ps Studies

A tunable Ti:Sapp laser will be used to excite the positronium from the 1S to the 2P state using a wavelength of approximately 243 nm. While in the 2P state a second laser will excite the positronium into one of the Rydberg states. Subsequently a third photon will then ionise the positronium and, using a small charged particle trap, the ionisation products may be captured and subsequently measured, providing direct evidence of the formation of the excited state positronium [26]. The system of lasers are detailed further in [30]; however of key importance is the 10 Hz repetition rate of the laser system. The Swansea two-stage accumulator, described in section 2.2, was designed to operate optimally at a matching repetition rate.

1.2.2 High Magnetic Field Studies

In 2000 Estrada *et al.* found that bombarding a gas covered surface with positrons in a high magnetic field (> 5 T) produced a fraction of positronium in Rydberg states with an efficiency of around 2×10^{-3} [31]. As well as the possible use of this positronium for antihydrogen formation, it offers a possible UHV compatible method of accumulating positrons. The weakly bound Rydberg states are field ionised by modest electric fields and the resultant ionisation products, namely the positrons, may be trapped in potential wells.

Studies into this effect have been performed on the Swansea positron beamline and have been reported in detail elsewhere [27, 32]. A number of candidate gases were studies and various magnetic fields. The highest measured Rydberg positronium yield was around 5×10^{-6} per incident positron. This result was more akin to the result obtained by Jelenković *et al.*, whom observed an efficiency of 6×10^{-6}[33], than Estrada's value.

1.2.3 Production of Cold Positrons

The quantity and final temperature of antihydrogen produced by the mixing method is dependent on the temperatures of the antiproton and positron clouds [34]. Using their current apparatus ALPHA estimated that they have a magnetic trap depth of 0.78 K for antihydrogen in its ground state [13] and so control of the quantum state and temperature of the antihydrogen is critical. Currently, positrons are cooled to ambient temperature either by cyclotron cooling in high magnetic fields or by collisions on a suitable buffer gas.

A method to produce extremely cold positron clouds, in the mK regime, is being investigated at Swansea. Positrons will be mixed with magnesium ions in a high (5 T) magnetic field. Positrons cool rapidly in high magnetic fields via cyclotron radiation and will, in turn, sympathetically cool the magnesium ions. The ions will then be cooled using laser cooling as has already been demonstrated by others [35]. The laser cooled magnesium ions will then sympathetically cool the positrons. Jelenković *et al.* have already demonstrated this principle by producing a positron cloud consisting of 10^3 positrons cooled by laser cooled beryllium ions [33].

1.2.4 Positron and Electron Plasma Mixing

The dynamics of positron–electron mixing is markedly different from the electron-ion case as the former is an example of an equal mass system. One of the interests of the Swansea group is to investigate such a system, primarily as a method of positronium production. Overlap of a positron plasma and an electron plasma is not possible using a nested Penning trap and so initially only one of the species will be in the plasma regime. An electron plasma will be formed in a cylindrical Penning trap in a high (5 T) magnetic field and a positron cloud will be transferred from the two-stage accumulator and re-trapped in the vicinity of the electron cloud. Recombination processes will be studied by mixing the two species in a manner similar to the method ATHENA used to produce antihydrogen, illustrated in figure 1.1. The amount of positronium formed will be determined either through annihilation, by monitoring gamma-ray emission using external detectors, or via field-ionisation in a suitable traps. It can be envisaged that in the future attempts will be made to simultaneously trap both positrons and electrons in the same spatial region creating a neutralised positron–electron plasma, but this will require the development of a new trap.

1.3 Thesis Outline

The second chapter begins with an outline of the apparatus and some operational procedures. A new control system which has been developed as part of these studies is also outlined. In concluding, a novel technique for determining the width of a cloud of charged particles is presented. The third chapter introduces some theoretical aspects relevant to these studies including the confinement of a charged particle in a Penning-type trap. The operation of a two-stage buffer gas accumulator is discussed and some of the characteristic parameters are presented.

The fourth chapter constitutes the bulk of the new work presented in this thesis. A theoretical model for a particle in a Penning-type trap with the asymmetric application of a rotating dipole electric field is developed and compared with experimental results taken using the Swansea two-stage positron accumulator. In the fifth chapter the effect of the application of the rotating wall electric field during accumulation is investigated. The final chapter summarises the conclusions which may be drawn from these studies and suggests future work to be carried out.

Chapter 2

Apparatus and Methods

"*Re Specialists:* Everyone is becoming better and better at less and less, and eventually someone is going to be superb at nothing"

— *Kenneth Williams (1987)*

This chapter outlines the important features of the Swansea positron beamline, along with some of the operational procedures. Section 2.1 gives an overview of the system and positron source. Section 2.2 provides a physical description of the accumulator and the control systems used for its operation; this is complementary to the theoretical description of the operation of the accumulator which is presented in section 3.2.

A description of the control system developed for these studies is presented in section 2.3. The sequencer software controls timing, digital output and analogue output as well as the acquisition of signal traces (digitisation). The final section in this chapter (section 2.4) describes the methods used to characterise the radial extent of the positron clouds. This includes a phosphor screen and a novel method which takes advantage of the fact that a non-interacting cloud of particles in a Penning trap has a Gaussian profile in the radial plane (proved later, in section 3.1).

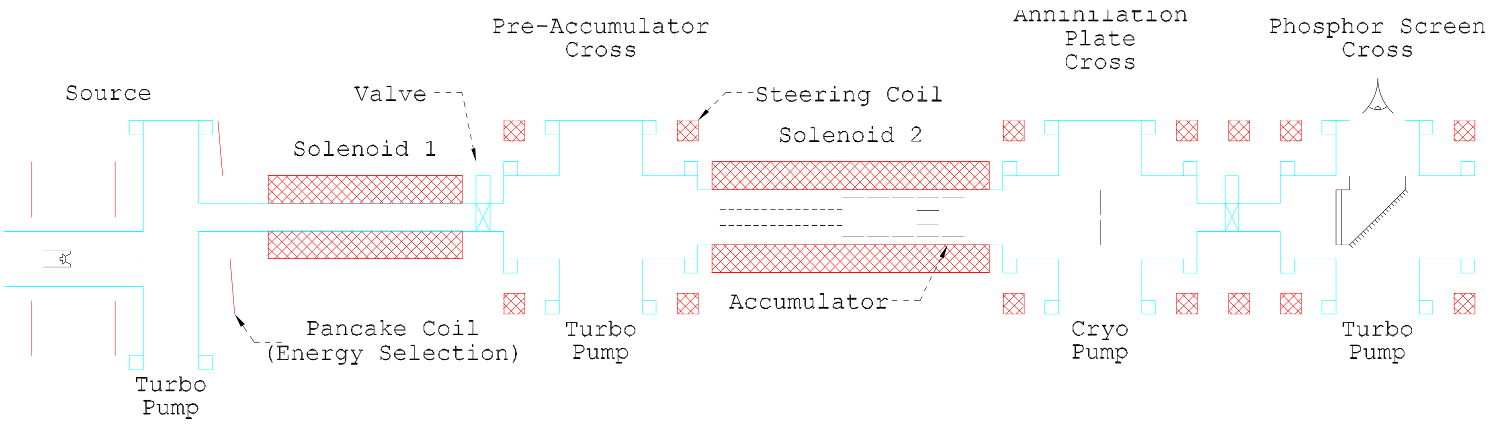

Figure 2.1: A schematic of the system used in these studies. A summary of the pumping and pressure specifications may be found in table 2.1.

2.1 System Overview

Further technical details about the Swansea positron beam-line may be found in [36, 26, 27]. Figure 2.1 shows a schematic of the parts of the Swansea positron beamline relevant to these studies.

2.1.1 Positron Source and Moderation

Sodium-22 emits β^+ particles with a branching ratio of around 90 %* with a half-life of 2.6 years: a convenient lifetime for beam-line applications. The simplified β^+ decay channel of ^{22}Na is

$$\begin{aligned} {}^{22}Na &\rightarrow {}^{22}Ne^* + e^+ + \nu_e && (2.1a) \\ {}^{22}Ne^* &\rightarrow {}^{22}Ne + \gamma_{(1.274\ MeV)}. && (2.1b) \end{aligned}$$

The β^+ particles emitted from ^{22}Na have a broad energy spread from 0 eV up to 544 keV. However a large number of applications require positrons with a narrow energy distribution. In addition to this, only a small fraction of the emitted positrons possess energies which may be manipulated using the modest electric and magnetic fields (V$\lesssim$ 2 kV, B$\lesssim$ 1 T) available in many laboratories. The technique of positron moderation may be adopted to improve this situation.

The first successful positron moderation was reported in 1958 by W. H. Cherry. During a study of secondary electron emission by positrons he found an anomalously high number of positrons with an energy in the range 0–5 eV when β^+ particles, emitted from a ^{64}Cu source, bombarded a chromium-on-mica surface. His results represented a moderation efficiency† of 10^{-8}; extremely small by today's standards. Had Cherry published his results in a widely read journal this may have generated a large interest, however he only presented his results in his thesis and thus they were relatively unknown at the time.

Although some progress was made, positron moderation received an increased interest when, in 1968, Canter *et al.* reported a moderation efficiency of 3×10^{-5} [37].

---

*The remaining 10 % of the branching ratio is electron capture.

†The moderation efficiency is defined in this case as the ratio of the number of emitted low energy positron to the number of incident β^+.

The moderator system they used was produced by burning magnesium ribbon in air and collecting the resultant oxide on gold. In the intervening years a number of different materials were found to have increasing positron moderation efficiencies, culminating in 1983 when Vehanen *et al.* pioneered the use of what has now become the most commonly used metal moderator, tungsten, with their original publication boasting an efficiency of $(3.2{\pm}0.4){\times}10^{-3}$ [38]. The majority of the early moderators were materials with surfaces which have a negative positron work function. In a simplistic view the positrons entering such moderators lose energy via inelastic collisions until they are thermal. Provided they are not lost via annihilation, the positrons then diffuse through the material to the surface where the negative positron work function may cause them to be ejected from the material.

It might be expected that a material with a positive positron work function would show no such emission however this is not, necessarily, the case. The rare gas solids (RGS) are wide band-gap insulators which have positive positron work functions. Positrons implanted into such materials with a kinetic energy of several keV lose energy via inelastic collisions involving electronic excitation and ionisation. In such an insulator once the positron energy is too low it is unable to lose further energy by electron–hole, exciton or positronium production and so can only loose energy by creating relatively low energy phonons ($E_{phonon} \lesssim 5.4$ meV for neon). As the positron does not thermalise it has a large diffusion length and so can reach the surface with sufficient energy to overcome the work function and escape [39]. To date, the most efficient positron moderator found is solid neon [40] with efficiencies of a few percent. It was found by Lynn *et al.* [41] that positron moderation was improved by the use of a conically shaped moderator, a fact which was verified for the RGS moderators by Khatri *et al.* [42].

Figure 2.2 shows the source assembly used in the Swansea beam-line. It is thermally connected to a cold-head (SHI Cryogenics RDK-408L2) capable of temperatures as low as 4.2 K but is kept electrically isolated by a sapphire disc and PEEK isolators. The pressure in the source chamber is increased to $2{\times}10^{-3}$ mbar as neon is admitted into the chamber by the use of a piezoelectric valve connected to a PID feedback control circuit. Over the course of approximately 30 minutes a layer of neon is grown onto the source assembly. During growth the positron count rate is measured using a CsI counter unit which detects the radiation as the positrons annihilate on the (closed) valve located immediately after the first solenoid (See figure 2.1). A typical moderator growth curve is shown in figure 2.3. The measured count rate is suppressed by scattering and annihilation on the uncondensed neon gas during growth and so as the gas is removed and the chamber returns to a base pressure of around 1×10^{-9} mbar, a jump is observed in the count rate which then slowly increases as the moderator stabilises.

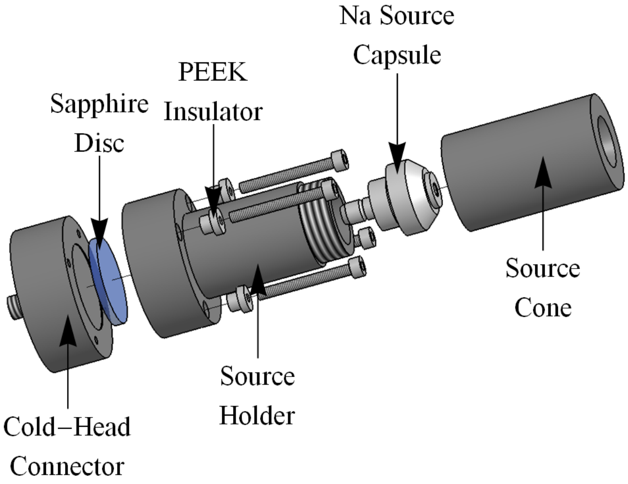

Figure 2.2: The source assembly used on the Swansea positron beam-line. The sapphire disc which electrically isolates the source capsule and cone is shown in blue.

The source and cone are held at an electric potential of 50 V, thus accelerating the moderated positrons. The 30 mT magnetic fields produced by the pancake coils (detailed in section 2.1.2.1) are unable to steer the high energy positrons across a step in the beam-line (see figure 2.1) and thus they do not form part of the main beam. A measurement of the kinetic energy distribution of the low energy positrons is shown in figure 2.4. This was taken by applying varying blocking potentials on the accumulator electrodes (see figure 2.5) and measuring the resultant number of positrons annihilating on the plate in the annihilation plate cross. The negated derivative of this measurement gives the energy profile of the beam.

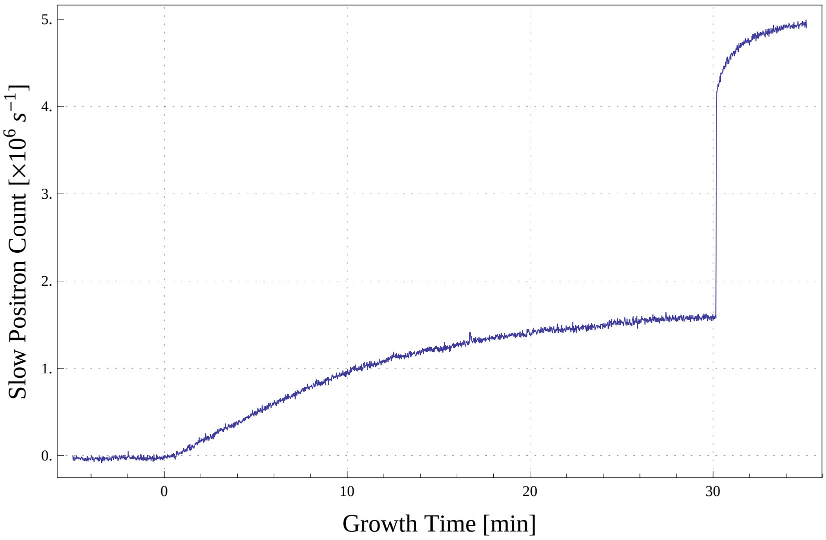

Figure 2.3: A typical moderator growth curve. The neon gas was admitted into the chamber, raising the pressure to 3×10^{-3} mbar, for approximately 30 minutes. Subsequently, there is a sudden increase in positron yield due to decreased attenuation as the gas is pumped out giving a final count rate of 5×10^6 slow e^+ s^{-1}.

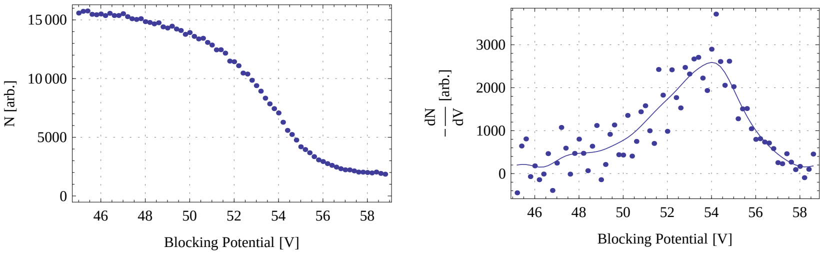

Figure 2.4: A measurement of the moderated positron beam energy distribution. The left figure gives the complementary cumulative distribution function (CCDF) for the distribution of the low energy positrons. The right figure is the negated derivative of the CCDF giving the energy distribution of the particles in the low energy beam. The solid line is a smoothed line to guide the eye.

2.1.2 Magnetic Fields

The beam is confined radially using a series of coils and solenoids placed at strategic positions along the beam-line. On occasion, small corrections to the beam steering are made by adjusting the positions and angles of the coils.

2.1.2.1 Pancake Coils

A pancake coil, consisting of a spirally wound wire, may be seen as a stack of current loops of increasing radius. From Ampere's law the magnetic field strength at the centre of a pancake coil can be approximated by

$$|B| = I \sum_{m=0}^{N} \frac{\mu_0}{2\left(r_0 + m r_\delta\right)}, \tag{2.2}$$

where I is the current through the pancake coil, r_0 is the inner radius of the coil, r_δ is the thickness of each layer and N is the number of layers in the stack.

The pancake coils on the Swansea positron beam-line consist of two such coils sandwiched together with $r_0 = 76$ mm, $r_\delta = 2$ mm and $N = 80$ giving a magnetic field strength at the centre of 0.722 mT A^{-1}. Given that the coils are usually used with a current of 40 A results in a magnetic field strength at the centre of 28.9 mT.

2.1.2.2 Steering Coils

The steering coils are made using 5 mm diameter wire. Using an average of the radius of the coils, Ampere's law gives the magnetic field strength in the centre of such a collection of current loops as

$$|B| = IN \frac{\mu_0}{r_{in} + r_{out}}, \tag{2.3}$$

where I is the current through the coil, r_{in} is the inner radius of the coil, r_{out} is the outer radius of the coil and N is the number of loops in the coil.

The steering coils on this system have an inner and outer radius of 258 mm and 300 mm respectively, and consist of 400 loops. This gives a magnetic field strength at the centre of 0.9 mT A^{-1}. Given that the coils are usually used with a current of 7 A, this provides a magnetic field strength at the centre of 6.3 mT.

2.1.2.3 Solenoids

There are two solenoids on the beam-line which have been directly wound onto the vacuum tubes. By Ampere's law the magnetic field strength is approximately uniform within the solenoid and given by

$$|B| = IN\mu_0 \frac{N_L}{L}, \tag{2.4}$$

where I is the current through the solenoid, L , N_L and N are the length, total number of turns per layer and number of layers on the solenoid respectively.

For the first solenoid on this system (solenoid 1 in figure 2.1) $L = 890$ mm, $N_L = 220$ turns per layer and $N = 4$. This gives a magnetic field strength of 1.254 mT A^{-1}. Given that the solenoid is usually energised with a current of 20 A, a magnetic field strength at the centre of 25.1 mT is obtained.

The second solenoid on this system (solenoid 2 in figure 2.1) was wound such that $L = 680$ mm, $N_L = 170$ turns per layer and $N = 4$. This gives a magnetic field strength of 1.257 mT A^{-1}. Given that the solenoid is usually used with a current of 40 A, the magnetic field strength at the centre is 50.3 mT.

2.1.3 The Vacuum System

A summary of the pump types and base pressures of the various pumping crosses relevant to these studies is shown in table 2.1. The source chamber has a base pressure of 10^{-9} mbar when pumped using a water cooled turbo-molecular pump (Pfeiffer TMU-520 500 ls^{-1} N_2) backed out by a scroll pump (Edwards XDS210). The pressure is measured using a cold-cathode ion gauge calibrated for N_2 connected via a PID control circuit to a Piezoelectric valve for moderator growth (detailed in section 2.1.1). The narrow pumping restriction, immediately after the source chamber, minimises the amount of nitrogen travelling from the accumulator and condensing onto the source.

The pre-accumulator cross has another turbo-molecular pump (Leybold 340M

400 ls^{-1} N_2). The typical base pressure in this cross is 10^{-8} mbar as measured with a cold-cathode ion gauge. It is the pressure on this gauge which is usually quoted as the accumulator buffer gas pressure however as shown in [26] due to the manner in which the nitrogen is allowed into the accumulator, the pressure in the first stage is typically two orders of magnitude higher.

The annihilation plate cross is pumped by a cryo-pump (SHI-APD6 800 ls^{-1} N_2). It has a typical base pressure of 10^{-8} mbar as measured with a cold-cathode ion gauge. It is the pressure as measured here which is usually quoted as the cooling gas pressure as the accumulator cooling gas is administered directly into the cross. The phosphor screen cross is pumped by an oil-free magnetically levitated turbo-molecular pump (Leybold 340M 400 ls^{-1} N_2) backed out by a scroll pump (Edwards XDS210). The pressure in this cross never exceeds 10^{-6} mbar since damage may be caused to the phosphor screen due to the high voltage applied to it.

Table 2.1: Vacuum specifications in the system.

Section	Pump Type	Base Pressure [mbar]
Source	Turbo	10^{-9}
Pre-accumulator Cross	Turbo	10^{-8}
Plate Cross	Cryo	10^{-8}
Phosphor Screen Cross	Turbo	10^{-8}

2.2 Accumulator

The Swansea two-stage accumulator consists of two different diameter cylindrical Penning traps. The first stage is comprised of 15 electrodes of length 24 mm with inside diameter 10 mm. The second stage has 5 larger electrodes of length 50 mm with inside diameter 41 mm. These are kept electrically isolated by the use of sapphire balls (diameter 2 mm) which fit into indents in the electrodes.

For normal operation the accumulator requires 8 different operating potentials as shown in figure 2.5. The remaining small electrode potentials are provided by a series potential divider to give successively lower voltages ranging from ‘grad high’ to ‘grad low’ in equal divisions. A PID feedback control circuit maintains

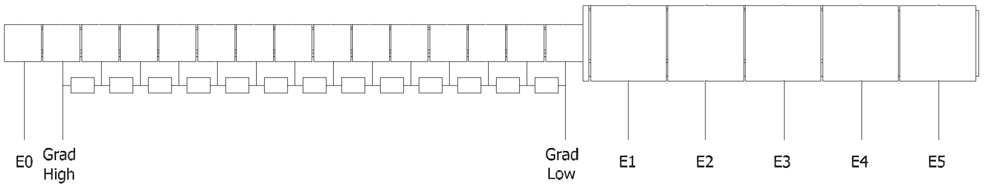

Figure 2.5: The accumulator assembly and electrical connections required for normal accumulator operation. E0, Grad High and Grad Low are the electrical connections required for the high pressure region (first stage) and E1-E5 are the electrical connections for the lower pressure region (second stage). Nitrogen buffer gas is admitted into the accumulator via a small hole in the centre electrode of the first stage.

a constant nitrogen pressure (as measured on a capacitance pressure gauge) at one end of a long narrow tube which admits the nitrogen into the first stage of the accumulator via a small hole in the central electrode. The actual pressures in the accumulator may be determined from the pumping speeds and restrictions as detailed in [26].

To facilitate the studies presented in this thesis a so-called rotating wall electrode has been installed (shown in an exploded view in figure 2.6). Electrode 4, E4, consists of two halves; it is one of these halves which has been split into four quadrants forming a rotating wall electrode. Sinusoidally varying voltages are applied in quadrature to each of the segments to produce a rotating wall electric field (detailed in section 3.3). This AC signal is superimposed on the DC voltage used for normal accumulator operation by the use of passive filters. The system of phase-splitters used to produce the four AC signals cause an attenuation of the voltages of 0.623±0.016 (as measured).

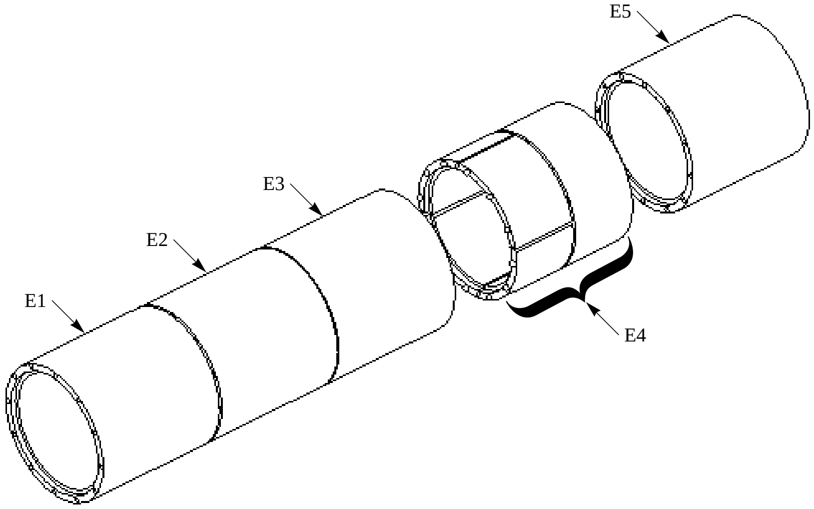

Figure 2.6: Exploded view of the second stage of the accumulator with the rotating wall electrode forming one half of electrode 4 (E4).

2.3 Timing and Analogue Output Control

As part of these studies a new measurement system was created using National Instruments (NI) hardware and software. NI Labview is a graphical programming package which allows quick and relatively straightforward development of measurement and control systems. This package, coupled with the NI hardware modules available, has been used to produce a system for the control and data acquisition from the Swansea beam-line apparatus.

The system used for the experiments presented here may be broken down into three components: a sequencer manages the timing requirements of the experiments; analogue output cards provide electric potentials and a digitiser acquires and saves the resultant data. The data are analysed post acquisition with a series of mathematical scripts written in Mathematica. A flowchart showing the different elements of the system is given in figure 2.7.

2.3.1 Sequencer

The sequencer card used is a National Instruments PCI-7813R (RIO 3 million gate FPGA) card with software drivers written by Dr Will Bertsche. The drivers allow the card to be programmed to produce digital (TTL) pulses with timing resolution down to 12.5 ns[‡] on up to 80 digital output lines. A further 10 digital input lines may be called upon for timing synchronisation with other pieces of hardware (a functionality which is not used in these studies).

The card is controlled by the use of a series of medium level command lines (ML) which are compiled into low level commands (or state lines) that are downloaded directly onto the FPGA for real-time execution. Each ML line contains the following information:

State Time (Double) Controls the output duration, including transition time, of the state line;

Infinite Timeout (Boolean) If the state line is waiting for a trigger on one of the trigger input lines, should the state be allowed to hang for an "infinite"

[‡] This allows a minimum duration for a sequence command line of 37.5 ns (LOW-HIGH-LOW).

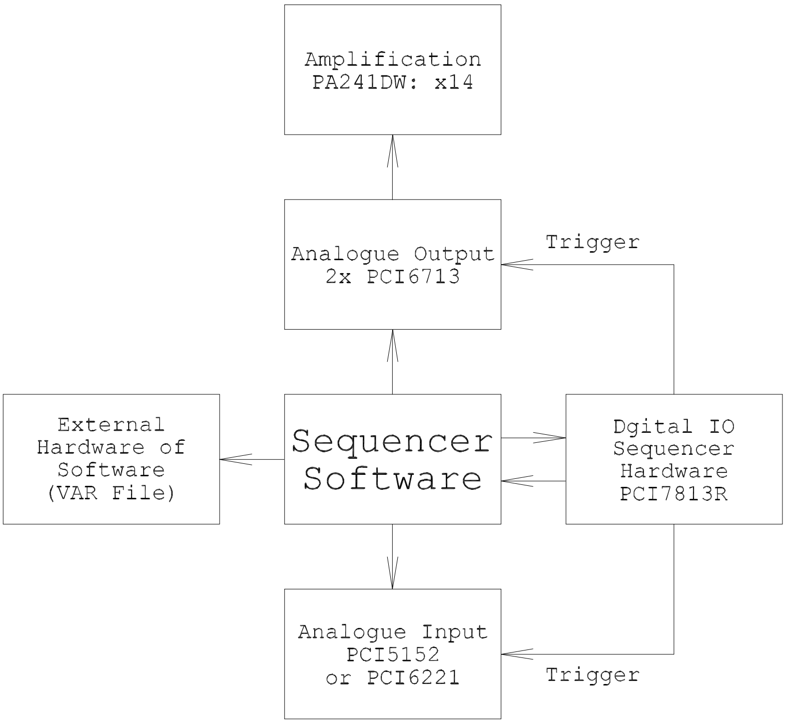

Figure 2.7: A flow chart showing the key elements of the sequencer system used to perform experiments.

time?;

DO Lines (Array of Booleans) The states (high/low) for the TTL outputs of the FPGA during this state line;

Trigger In Lines (Array of Booleans) The state required for the digital input lines to match before the state line should end;

Timeout Is Error? (Boolean) If the state does not have an infinite timeout and the state time is exceeded should the sequence continue to run or be terminated with an error generated;

Loop Count (Integer) It is possible to create looping state lines. The state lines will loop between this state and the next (non-nested) loop return state line this number of times;

Loop Return (Boolean) The return signal for a loop. The drivers also support nested loops (loops within loops).

The TTL standard, as used by the FPGA, is not able to drive a 50 Ω terminated signal into the high state and so a buffer has been made to increase the current capability of the TTL signals to drive 50 Ω terminated lines.

2.3.2 Analogue Output

The system has two NI PCI-6713 cards each having 8 analogue outputs with an output resolution of up to 1 MS/s. The outputs are bipolar with a range of ±10 V in 12 bit resolution and are accessible via BNC connectors on a NI-BNC2120 connector block. In their factory default mode the cards produce an output value which can only be changed on the regular clock ticks provided by a settable internal clock. Thus an output of 1 ms at 1 V followed by an output of 1 s at 2 V would require 1001 value lines to be written to the card. In this mode output sequences requiring many different time scales result in huge numbers of output states which can easily fill the on-board memory of the cards; a problem which is overcome by the integrated system.

The low voltage analogue signals are passed through amplifiers with gains of 14. The amplifiers, which are produced by Aarhus University, are built on a PA241DW high voltage operational amplifier circuit. Overall, the amplifying circuit has a transition time (10-90%) of ~ 3 μs. Thus, analogue output in the range of ± 140 V may be employed on this apparatus with a timing resolution down to 3 μs.

2.3.3 Digitisation

Originally measurements were digitised by the use of an NI PCI-5152 2 GS/s (8 bit) digitiser card, however part way through these studies this card failed and a much slower PCI-6221 card capable of 250 kS/s with 16 bit resolution was installed. The digitiser software written allows many of the common functionalities of a digital oscilloscope such as peak-to-peak measurements and averaging. One advantage of this digitiser system over a conventional oscilloscope is the ability to record at a repetition rate of over 50 Hz and to record each of the traces for post-acquisition averaging. This allows a more flexible system for error and uncertainty analysis.

The digitised signals are typically processed post-acquisition using a series of scripts written as Mathematica notebooks, however the output is in an ASCII tab separated value (.TSV) format which may be interpreted by most programs.

2.3.4 Integration into a single system

The hardware was configured so that the three elements could be integrated into a single measurement system. Software was written to allow easy use of this integrated system and a certain degree of automation can be achieved. The user supplies the following settings either in a sequence line, as shown in figure 2.8, or in an ASCII file:

Duration The duration of the output state;

DO States The digital output states;

DI States The digital input states;

Label A non-functional label;

AO Steps The number of steps which should be taken to produce the analogue output as it is possible to ramp the analogue output in a number of steps rather than a single transition. If this is set to zero then the higher timing resolution capability of the digital output may be accessed;

Device 1 AO The target analogue output for the first NI PCI-6713 analogue output card;

Device 2 AO The target analogue output for the second NI PCI-6713 analogue output card.

Figure 2.8: An example of a GUI sequence line used to control the timing and output.

The software has been written to interface with additional hardware as required. Prior to the execution of a sequence a value is written to a global variable along with a Boolean flag indicating if the variable has been acknowledged. Once this variable has been acknowledged the flag is set to true and the execution of the sequence may commence. The sequencer has been successfully integrated with the laser system, phosphor screen, rotating wall function generator, buffer gas pressure control and vacuum valve control using this system.

Subroutines have also been written which facilitate the creation of sequences and the global variable settings programmatically. Using these is it possible to automatically create large numbers of sequences with varying parameters. As an example, a typical frequency scan as shown in chapter 4 requires 1111 sequences and thus these subroutines are invaluable.

The regular internal clock of the analogue output cards was replaced by a digital signal from the sequencer. Thus, each different output state would require only one set of values independent of the output duration, thereby overcoming the memory issue stated earlier.

In summary, the system is capable of:

- Analogue output in the range of ±140 V with a timing resolution of 3 μs;
- TTL digital output with a minimum state duration of 37.5 ns and timing resolution of 12.5 ns;
- Sequence synchronisation (via TTL Input) with a minimum state duration of 37.5 ns and timing resolution of 12.5 ns;
- Signal digitisation;
- Interfacing with other hardware.

2.4 Radial Diagnostics

2.4.1 Phosphor Screen

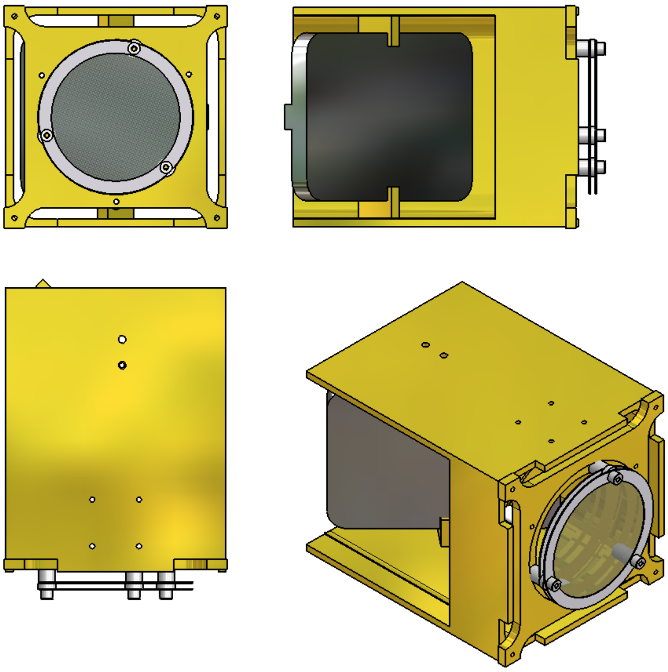

Figure 2.9: A drawing of the phosphor screen assembly used as part of these studies. (Model by Serena Kerrigan).

A phosphor screen assembly (see figure 2.9) is located in a pumping cross after the accumulator as shown in figure 2.1. The assembly houses a grid for particle energy selection, a phosphor screen and a 45 degree planar mirror to reflect an image of the back of the phosphor screen to a window located in the side of the pumping cross. When charged particles are accelerated into the phosphor of type P43 (Gd_2O_2S:Tb), light is emitted in the range of 360 - 680 nm (maximally at 545 nm), with a 90–10% decay time of 1 ms [43]. This is captured using a Santa Barbara Instrument Group ST-7XE camera. This particular camera is designed primarily for astronomical imaging with a telescope and is therefore not able to be triggered by a hardware signal. Given the very small light yield produced by a single positron cloud, and the relatively high background, the signal is integrated (exposed) for 1000 s (10,000 clouds at a 10 Hz trap repetition cycle each containing around 10^4 positrons). An additional background image without the presence of the cloud signals is also taken for 1000 s. Thus a complete image of a positron cloud with this system takes 2000 s.

The images are fitted with a two-dimensional Gaussian of the form

$$N(x,y) = \frac{A}{2\pi\sigma^2}\exp\left(-\frac{(x-x_0)^2+(y-y_0)^2}{2\sigma^2}\right) \tag{2.5}$$

where (x_0, y_0) is the centre of the cloud in Cartesian coordinates, and σ is related to the width of the cloud, with the full width half maximum (FWHM) being equal to $2\sigma\sqrt{2\ln(2)}$.

2.4.2 Hole Masking Method

2.4.2.1 Theory

It will be shown in section 3.1.2 that a thermalised cloud of non-interacting charged particles in a Penning-type trap has a 2-dimensional Gaussian distribution, $N(r)$, in the radial plane. This is confirmed by phosphor screen images such as the example shown, together with a fit of the form given by equation 2.5, in figure 2.10.

The 1000 s required for a phosphor screen image (assuming a background

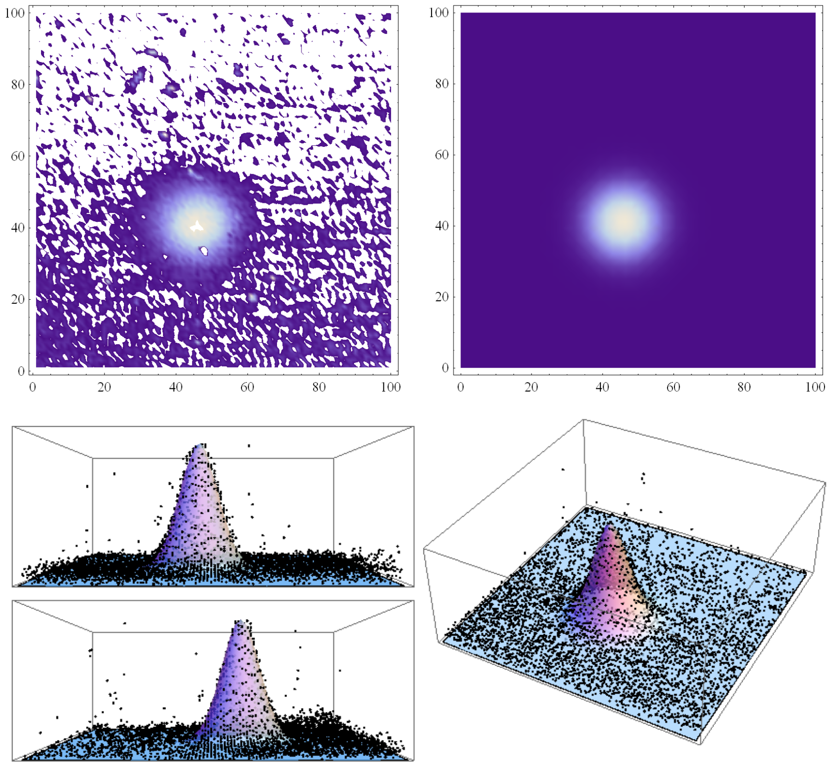

Figure 2.10: Top-left: an image of a cloud of positrons taken with the phosphor screen. Top-right: a 2D fit to the positron cloud distribution of the form given in equation 2.5. Bottom: 3d scatter plots of the pixel intensity from different viewpoints; the surface represents the 2D fit.

image has already been taken) is not very practical for the studies presented in this thesis as a very large number of measurements was required. Thus, an alternative method of determining the radial extent of the positron cloud has been developed using a plate with a circular aperture of radius r_0 to mask the cloud. By measuring the number of positrons annihilating on the plate, N_{mask}, along with the number of positrons escaping through the hole, N_{trans}, it is possible to determine the width of the cloud using:

$$N_{trans} = \int_0^{r_0} 2\pi r N(r)\,dr = N_0\left(1 - \exp\left(-\frac{r_0^2}{2\sigma^2}\right)\right) \tag{2.6a}$$

$$N_{mask} = \int_{r_0}^{\infty} 2\pi r N(r)\,dr = N_0 \exp\left(-\frac{r_0^2}{2\sigma^2}\right). \tag{2.6b}$$

In figure 2.11, the geometrical interpretations of N_{mask} and N_{trans} may be seen. Thus, combining equations 2.6 and rearranging gives

$$\frac{\sigma}{r_0} = \frac{1}{\sqrt{2\ln\left(1 + \frac{N_{trans}}{N_{mask}}\right)}}. \tag{2.7}$$

The uncertainty in which may be calculated from

$$\left(\frac{\Delta\sigma}{r_0}\right)^2 = \frac{N_{trans}^2 \Delta N_{mask}^2 + N_{mask}^2 \Delta N_{trans}^2}{8N_{mask}^2 (N_{mask} + N_{trans})^2 \ln\left(\frac{N_{mask}+N_{trans}}{N_{mask}}\right)^3}, \tag{2.8}$$

where Δ denotes the uncertainty in a quantity. A plot of the function given in equation 2.7, as shown in figure 2.12, shows that this method is most suited to clouds with a radius in the range $2r_0 \leq \sigma \leq 8r_0$ as this is the region in which the function has a reasonable sensitivity to variations in N_{trans}/N_{mask}.

N_{mask} and N_{trans} are measured by using the caesium-iodide detectors positioned as illustrated in figure 2.13. The annihilation plates are centred in their respective pumping crosses. As the positron cloud traverses the system the first caesium-iodide detector measures N_{mask} and the second measures N_{trans}.

It was anticipated that obtaining a very high degree of accuracy when aligning the hole and cloud centre would be problematic. Vertical alignment could be

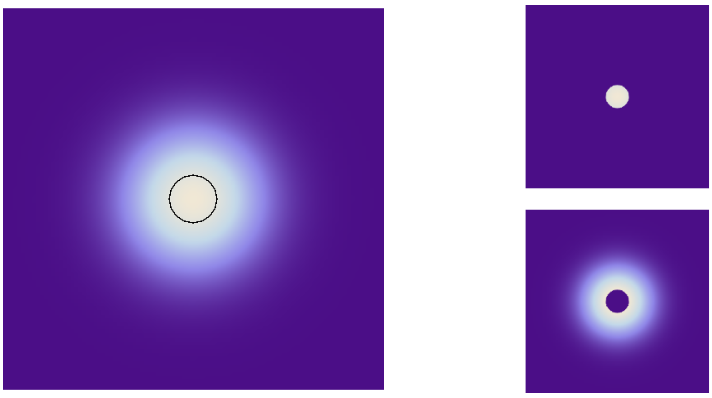

Figure 2.11: Simulated plots of an idealised cloud with a Gaussian profile. The upper right image represents the transmitted signal (N_{trans}) while the lower right image represents the masked signal (N_{mask}).

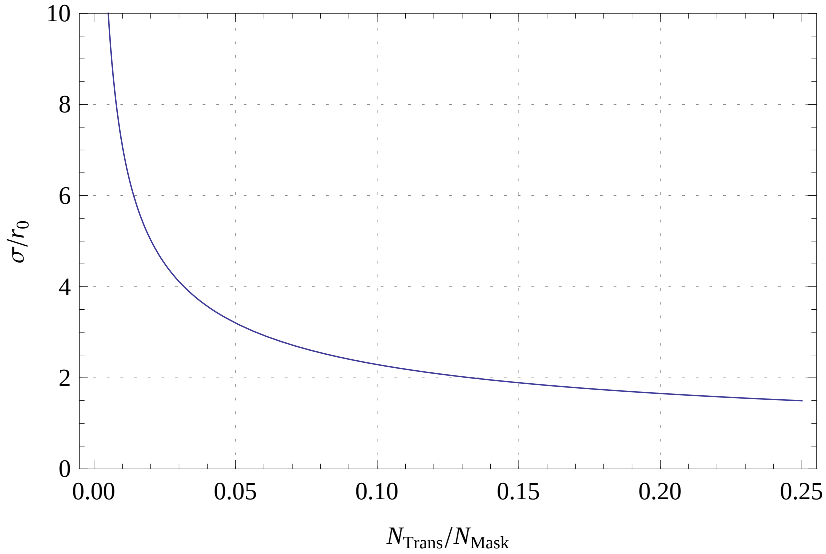

Figure 2.12: A graph showing the relationship between the cloud width to hole radius ratio ($\frac{\sigma}{r_0}$) and the transmitted to masked signal ratio ($\frac{N_{trans}}{N_{mask}}$) determined from equation 2.7.

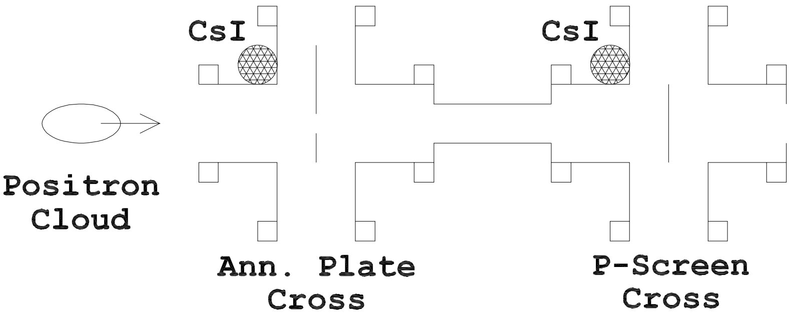

Figure 2.13: A schematic showing the implementation of the hole method on the Swansea positron beam-line.

achieved by moving the plate on a linear manipulator. In the horizontal direction, however, the alignment could only be changed by moving the large steering coils. In figure 2.14 the numerically calculated effect of a misalignment of the hole with respect to the centre of the ejected cloud is shown. It can be concluded that this method still gives reasonable estimates with an error less than few percent provided that $\frac{\sigma}{r_0}$ is greater than the size of the misalignment.

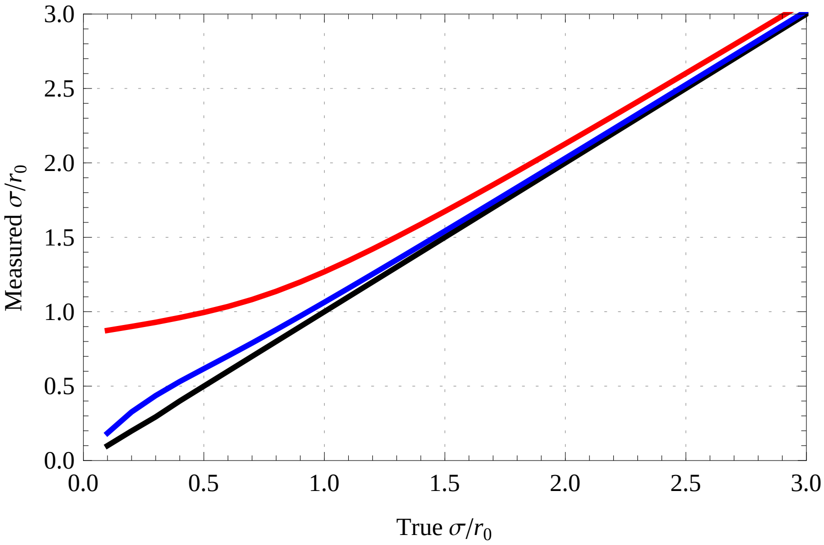

Figure 2.14: Figure showing the effect of varying severities of misalignment on the calculated cloud width. (No misalignment – Black, 0.5σ misalignment – Blue, σ misalignment – Red.

Care has been taken to verify the alignment of the positron clouds with the hole centre by the use of images from the phosphor screen. The hole was positioned in the centre of the cross (see figure 2.1) and the cloud position adjusted by moving the appropriate steering coils. Figure 2.15 shows images of positron clouds taken using the phosphor screen both with and without the masking in place. The centres of the features were determined using a 2D-fit implemented in Mathematica. This gives the centres, (x_0, y_0) in units of pixels, of the masked and unmasked features as (25.8±0.5, 23.7±0.5) and (27.7±0.3, 27.3±0.3) respectively. Given the screen calibration at the time of 1 pixel = 0.129±0.001 mm gives a hole-cloud misalignment of 0.52±0.07 mm.

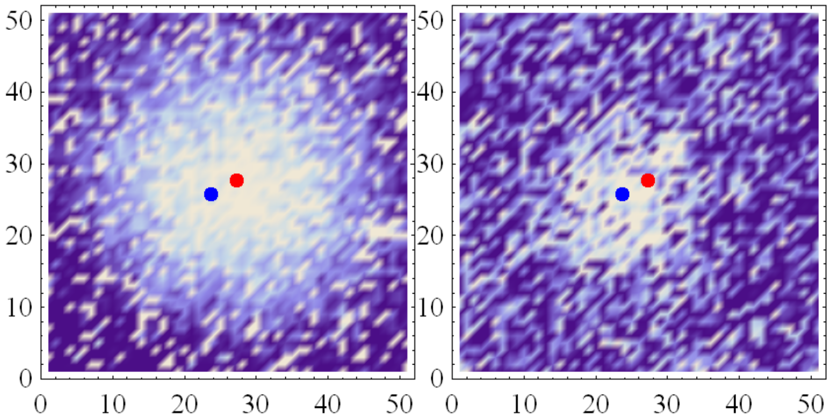

Figure 2.15: Images of positron clouds taken using the phosphor screen. Left: Unmasked. Right: Masked by the hole. The red dot is the fitted centre of the cloud and the blue dot is the fitted centre of the hole. The scale shown is in units of pixels.

In order to verify this method of determining the radial extent of the cloud a frequency scan was performed using both the method above and fitting to phosphor screen images for comparison. Frequency scans are detailed in section 4.2.1 however, in short, they are used here to produce positron clouds of varying radii (σ) and particle number (N_0). Figure 2.16 shows the width of the clouds during a measurement using both the phosphor screen and the hole method which has been described herein.

Thus the masking method described herein offers a reliable method of determining the radial width of a cloud of non-interacting charged particles in

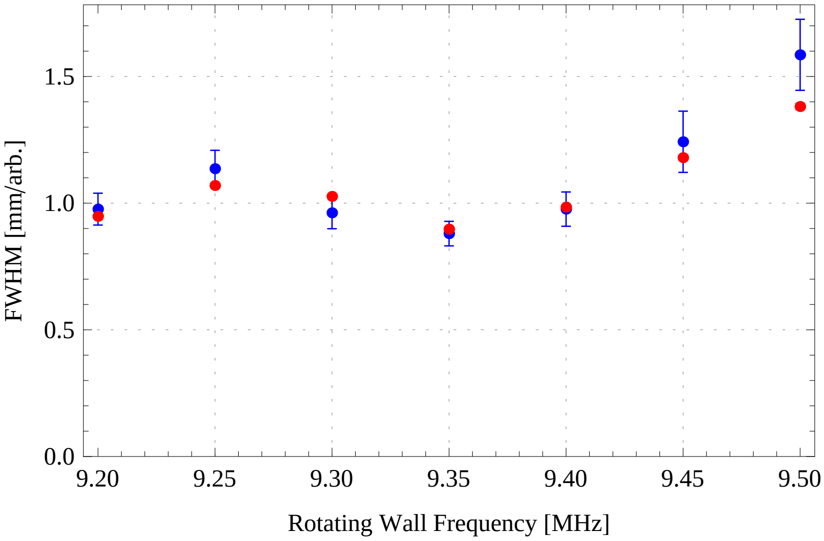

Figure 2.16: A comparison of the hole-masking method of determining the cloud size σ (blue) and fitted images taken using the phosphor screen (red). The uncertainties associated with the fitted images are too small to be visible on the plotted scale. The sizes have been normalised to the weighted means of the data-sets to eliminate calibration errors.

a Penning-type trap. It is a far more rapid method than using the phosphor screen, reducing the acquisition time by a factor of 10^4 assuming averaging over 10 measurements is used.

Chapter 3

Background Theory

“Nature has given man one tongue, but two ears, that we may hear twice as much as we speak”

— *Epictetus (c. AD 100)*

In section 3.1 the motion of charged particles in Penning-type traps is presented. Such traps are commonly used in experiments for the storage of charged particles. Section 3.2 details the operation of a specific type of trap: a two-stage buffer gas positron accumulator. The accumulation of positrons has facilitated the studies of many-positron effects* as well as the formation of very narrow mono-energetic positron beams, suited to atomic physics and scattering measurments. Two-stage positron accumulators are generally smaller and therefore both cheaper and easier to fabricate than their three-stage counterparts. The final section (section 3.3) presents the electric field for a segmented cylindrical electrode and shows, with appropriately applied potentials, how this may be used to form a rotating wall electric field.

---

*A many-positron effect is defined as a physical effect involving more than a single positron, such as is the case with positron plasmas.

3.1 Charged Particles in Penning-Type Traps

A Penning-type trap uses static electric and magnetic fields to confine charged particles or alternatively clouds of charged particles consisting of only a single sign of charge. Although the term has not been readily accepted by the physics community the system of a charged particle confined in a Penning-type trap is sometimes referred to as geonium, since all potentials are with respect to ground and thus the particle may be considered bound to the earth [44]. Penning traps have been used in many high precision experiments including:

- The first trapping of anti-protons [45] and the subsequent measurement of the anti-proton to proton mass ratio to a fractional uncertainty of 4×10^{-8} [46].
- The most precise measurement to date of the electron g-factor [47] of $g/2 = 1.001\ 159\ 652\ 193\ (4)$. This may be compared with a value of $g/2 = 1.001\ 159\ 652\ 459\ (135)$ given by QED with corrections to the eighth order [48];
- The measurement of the positron g-factor to a similar accuracy [47] : Comparison of this value with the electron g-factor has given the most precise test of CPT invariance using leptons to date;
- The confinement of a single positive Barium ion was achieved [49], facilitating molecular spectroscopic studies of trapped ions [50].

The conventional Penning trap design by Dehmelt uses hyperbolic electrodes, as illustrated in figure 3.1, to produce a quadrupole electric field in the trap. This potential may be expressed as

$$\phi(x,y,z) = \frac{V_0}{2d^2}\left(z^2 - \frac{1}{2}x^2 - \frac{1}{2}y^2\right), \tag{3.1}$$

where V_0 is the voltage applied to the electrodes and d is a length parameter associated with the trap geometry. This potential is shown in figure 3.2. Another Penning-type trap is the Penning-Malmberg trap. This uses three cylindrical electrodes to produce an electric potential minimum as illustrated in figure 3.3.

A number of techniques may be employed to enhance the quadratic term and minimise higher order terms in the expansion of this minimum including intermediate compensation electrodes to produce other cylindrical-Penning trap geometries. The cylindrical form of Penning-traps are easier to fabricate than the original hyperbolic Penning traps and have the advantage of being open ended and therefore easier to load with particles.

All of these trap types are submerged in a uniform magnetic field which lies parallel to the axis of cylindrical symmetry of the trap (conventionally in the $\hat{\boldsymbol{z}}$ direction).

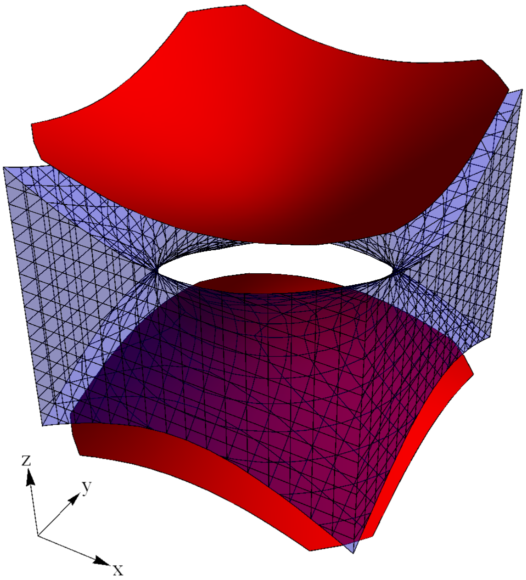

Figure 3.1: A 3-dimensional plot showing the electrodes used in a Penning trap to produce a quadrupole potential.

The motion of a charged particle of mass m and charge q in the non-relativistic limit in an electromagnetic field is described by the Lorentz equation

$$m\ddot{\mathbf{x}} = q\left(\mathbf{E} + \dot{\mathbf{x}} \times \mathbf{B}\right), \tag{3.2}$$

where $\mathbf{E}$ and $\mathbf{B}$ are the electric and magnetic fields at the location $\mathbf{x}$. Inserting the electric field $\mathbf{E} = -\nabla\phi$ where the electric potential, ϕ, is given by equation 3.1 and the magnetic field $\mathbf{B} = B\hat{\boldsymbol{z}}$, equation 3.2 may be separated into axial, z, and

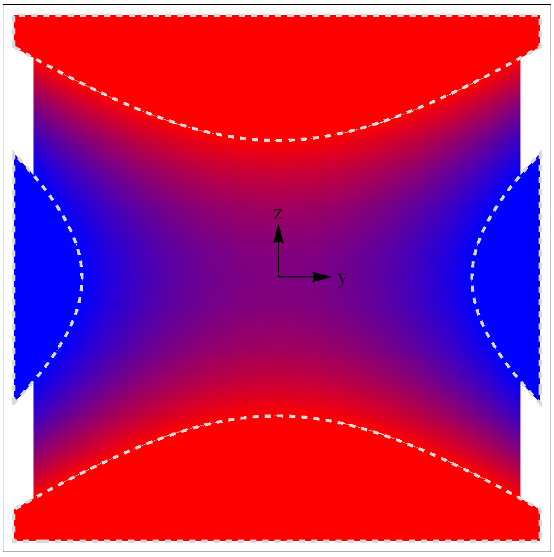

Figure 3.2: A cross section of the electric field produced by the Penning trap geometry. The blue electrodes represent the end-caps, while the red electrode is a cross section of the ring electrode. The gradient illustrates the quadrupole field, with red being the lower potential and blue being higher potential.

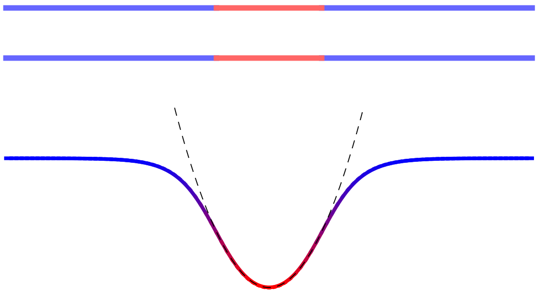

Figure 3.3: A schematic of a cylindrical-Penning Trap. The end electrodes (blue) are held at a higher potential while the central electrode (red) is held at a lower potential. The colour scheme is such that this can be compared with figure 3.1. The dotted line is a quadratic fit to the potential minimum.

radial, $\boldsymbol{r}$, equations as

$$\ddot{\boldsymbol{r}} - \Omega_c \hat{\boldsymbol{z}} \times \dot{\boldsymbol{r}} - \frac{1}{2}\omega_z^2 \boldsymbol{r} = 0, \tag{3.3a}$$

$$\ddot{z} + \omega_z^2 z = 0, \tag{3.3b}$$

where Ω_c and ω_z are the cyclotron and axial bounce frequencies respectively. These are defined as

$$\Omega_c = \frac{qB}{m}, \tag{3.4a}$$

$$\omega_z^2 = \frac{qV_0}{md^2}. \tag{3.4b}$$

3.1.1 The Solution in Cartesian Coordinates

The motion of charged particles in a Penning-type trap is most easily understood in Cartesian coordinates. Re-writing equations 3.3 in Cartesian coordinates gives

$$\ddot{x} = \frac{\omega_z^2}{2}x + \Omega_c \dot{y} \tag{3.5a}$$

$$\ddot{y} = \frac{\omega_z^2}{2}y - \Omega_c \dot{x} \tag{3.5b}$$

$$\ddot{z} = -\omega_z^2 z. \tag{3.5c}$$

Using the definition

$$\Lambda = x + \mathbf{i}y, \tag{3.6}$$

equations 3.5a and 3.5b can be combined to give

$$\ddot{\Lambda} = \frac{\omega_z^2}{2}\Lambda - \mathbf{i}\Omega_c \dot{\Lambda}. \tag{3.7}$$

This equation may be solved by making the substitution $\Lambda = e^{-\mathbf{i}\omega t}$ giving the characteristic equation

$$2\omega^2 - 2\Omega_c \omega + \omega_z^2 = 0, \tag{3.8}$$

which has roots

$$\omega_{\pm} = \frac{1}{2}\left(\Omega_c \pm \sqrt{\Omega_c^2 - 2\omega_z^2}\right). \tag{3.9}$$

The positive root refers to the modified cyclotron frequency (ω_c) and the negative root referring to the magnetron frequency (ω_m)[†]. This shows that a requirement for confinement is that $\Omega_c^2 > 2\omega_z^2$.

The solutions to equations 3.5a and 3.5b are thus

$$x = |A_+|\cos(\omega_+ t + \phi_+) + |A_-|\cos(\omega_- t + \phi_-), \tag{3.10a}$$

$$y = |A_+|\sin(\omega_+ t + \phi_+) + |A_-|\sin(\omega_- t + \phi_-). \tag{3.10b}$$

The solution to equation 3.5c is trivial:

$$z = |A_z|\cos(\omega_z t + \phi_z). \tag{3.11}$$

The constants of integration $A_{\pm,z}$ and $\phi_{\pm,z}$ are determined by the initial position and velocity of the particle.

Thus, the motion of the particle is described by three well defined frequencies as illustrated in figure 3.4. The motion in the axial direction, $\hat{\boldsymbol{z}}$, is a periodic bounce at the frequency ω_z. In the transverse plane, $\boldsymbol{\rho}$, the particle follows a path described by an epicycloid; that is, the superposition of a fast circular motion with an angular frequency ω_c, and a slow circular motion with an angular frequency ω_m.

For trapped particles in a Penning-type trap there exists the hierarchy

$$\omega_m < \omega_z < \omega_c. \tag{3.12}$$

Table 3.1 gives examples of the modified cyclotron, magnetron and axial bounce frequencies of various ions in a Penning-type trap with typical trap parameters.

[†] The notation $\omega_{\pm}$ and (ω_c, ω_m) are used interchangeably where the former often yields compact mathematical formulae and the latter is more commonly used in experimental applications.

Table 3.1: Typical modified cyclotron, axial bounce and magnetron angular frequencies for various charged particles in a Penning trap with $V_0/d^2 = 2 \times 10^5$ Vm^{-1} and $B = 40$ mT.

	ω_c [rad s^{-1}]	ω_z [rad s^{-1}]	ω_m [rad s^{-1}]
e^+	7.03×10^{10}	1.88×10^8	2.50×10^6
$^1H^+$	3.81×10^7	4.38×10^6	2.52×10^5
$^3Li^+$	1.25×10^7	2.53×10^6	2.55×10^5
$^{238}U^{91+}$	1.44×10^7	2.71×10^6	2.54×10^5
$^{198}Hg^+$	Not Trapped	3.11×10^5	Not Trapped

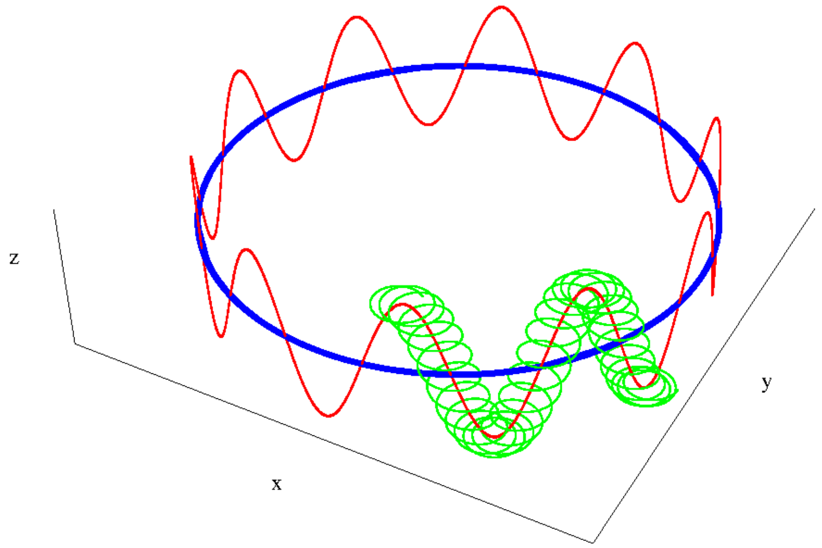

Figure 3.4: The three fundamental motions in a Penning trap: magnetron motion (blue), cyclotron motion (green) and axial bounce (red).

3.1.2 The Solution in $\mathbf{V}^{\pm}$ Coordinates

A different coordinate system may be used allowing the magnetron and cyclotron motions to be decoupled. These new coordinates allow further investigation of properties such as the energetics of the trapped particles to be carried out more easily as well as a so-called guiding centre approximation to be made on the particle motion which neglects the fast cyclotron motion. These coordinates are also used in chapter 4 to solve a more complicated system.

The magnetron and cyclotron motions are separated by the use of the vectors $\mathbf{V}^{\pm}$ defined as

$$\mathbf{V}^{\pm} = \dot{\boldsymbol{r}} - \omega_{\mp}\hat{\boldsymbol{z}} \times \boldsymbol{r}. \tag{3.13}$$

Differentiating equation 3.13 and inserting the result into equation 3.3a, as shown in appendix A, gives

$$\dot{\mathbf{V}}^{\pm} = \omega_{\pm}\hat{\boldsymbol{z}} \times \mathbf{V}^{\pm}, \tag{3.14}$$

so, $\mathbf{V}^{+}$ ($\mathbf{V}^{-}$) rotates about a circle with frequency ω_{+} (ω_{-}). Taking the cross product of the difference $(\mathbf{V}^{+} - \mathbf{V}^{-})$ and $\hat{\boldsymbol{z}}$ gives

$$\boldsymbol{r} = -\frac{\hat{\boldsymbol{z}} \times \left(\mathbf{V}^{+} - \mathbf{V}^{-}\right)}{\omega_{+} - \omega_{-}}. \tag{3.15}$$

Uniform circular motion is described by $\omega\boldsymbol{r} = -\hat{\boldsymbol{z}} \times \dot{\boldsymbol{v}}$, where ω and $\dot{\boldsymbol{v}}$ are the angular frequency and velocity of the circular motion respectively. Equation 3.15 therefore represents the superposition of two circular orbits: i.e. an epicycloid.

The Hamiltonian for the radial motion of the particle is equal to the sum of the kinetic energy of the particle and the repulsive electrostatic potential energy as

$$H_{\boldsymbol{r}} = \frac{1}{2}m\left(\dot{\boldsymbol{r}}^{2} - \frac{1}{2}\omega_{z}^{2}\boldsymbol{r}^{2}\right) \tag{3.16}$$

Using equation 3.15 and its derivative, the above equation becomes

$$H_{\boldsymbol{r}} = \frac{1}{2}m\left(\frac{\omega_{+}(\mathbf{V}^{+})^{2} - \omega_{-}(\mathbf{V}^{-})^{2}}{\omega_{+} - \omega_{-}}\right) = H^{+} + H^{-} \tag{3.17}$$

with H^{+} being the cyclotron Hamiltonian and H^{-} the magnetron Hamiltonian. The magnetron Hamiltonian has a negative sign leading to an unstable motion.

The potential form given in equation 3.1 shows that while a confining potential exists in the $\hat{\boldsymbol{z}}$ direction, a repulsive term exists in the radial ($\mathbf{r} = (x, y)$) plane. The magnetron motion of the particle may be viewed as a rotation about the top of a potential hill as illustrated in figure 3.5. If energy is removed from the magnetron motion the particle will become lower around the potential hill and thus the magnetron radius increases until the particle is eventually lost when it hits one of the electrodes.

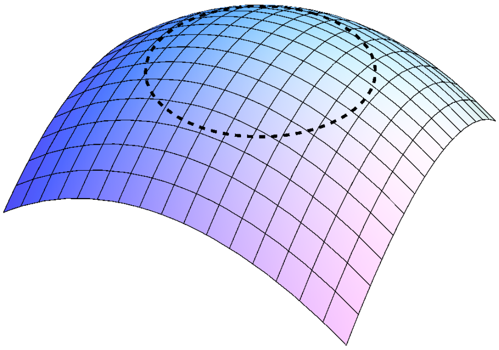

Figure 3.5: The magnetron motion may be viewed as a rotation about the top of a potential hill. If energy is removed the particle will circle around the hill at a lower energy with a larger radius.

The kinetic energy contained within the magnetron motion may be written as

$$E_m = \frac{1}{2} m \omega_m^2 A_m^2, \tag{3.18}$$

where A_m is the amplitude of the magnetron motion. This may be re-arranged to give the amplitude of the magnetron motion as a function of energy as

$$A_m = \sqrt{\frac{2E_m}{m\omega_z^2}}. \tag{3.19}$$

Assuming an ensemble of non-interacting particles with a thermal distribution, N_r,

$$\frac{N_r}{N_0} = \exp\left(-\frac{E_m}{k_B T}\right), \tag{3.20}$$

it may be concluded that,

$$\frac{N_r}{N_0} \propto \exp\left(-\frac{m\omega_m^2 A_m^2}{2k_B T}\right). \tag{3.21}$$

Therefore, a collection of thermal non-interacting particles in a Penning trap will have a Gaussian distribution in the radial plane. This model will hold only for a low density cloud and fails as the cloud densities and temperatures approach the plasma regime.

3.1.3 Damping the Motion of the Trapped Particles

Trapped particles may be cooled by inelastic collisions with a suitable cooling gas. This may be modelled by a Stokes' viscous drag term,

$$\ddot{\mathbf{x}} = -\frac{q}{mK}\dot{\mathbf{x}}, \tag{3.22}$$

where K is defined as the particle mobility in the gas at the given temperature and pressure. The effect of this term is to modify equations 3.5 to be

$$\begin{aligned} \ddot{x} &= \frac{\omega_z^2}{2}x + \Omega_c \dot{y} - \kappa \dot{x}, && (3.23a)\\ \ddot{y} &= \frac{\omega_z^2}{2}y - \Omega_c \dot{x} - \kappa \dot{y}, && (3.23b)\\ \ddot{z} &= -\omega_z^2 z - \kappa \dot{z}. && (3.23c) \end{aligned}$$

where $\kappa = q/(Km)$. Using the definition $\Lambda = x + \mathbf{i}y$ allows equation 3.23a and 3.23b to be combined giving

$$\ddot{\Lambda} = \frac{\omega_z^2}{2}\Lambda - (\kappa + \mathbf{i}\Omega_c)\dot{\Lambda}. \tag{3.24}$$

The substitution $\Lambda = e^{-\mathbf{i}\omega t}$ gives a characteristic equation with roots given by

$$\omega_\pm = \frac{1}{2}\left(\Omega_c \pm F_+ - \mathbf{i}\left(\kappa \pm F_-\right)\right), \tag{3.25}$$

where

$$F_{\pm} = \frac{1}{\sqrt{2}} \left(\sqrt{\left(\Omega_c^2 - 2\omega_z^2 - \kappa^2\right)^2 + 4\Omega_c^2\kappa^2} \pm \left(\Omega_c^2 - 2\omega_z^2 - \kappa^2\right) \right)^{\frac{1}{2}} . \tag{3.26}$$

Assuming Ω_c, $\omega_z >> \kappa$ this simplifies to

$$\omega_{\pm} \approx \frac{\Omega_c \pm \sqrt{\Omega_c^2 - 2\omega_z^2}}{2} \left(1 \mp \mathbf{i} \frac{\kappa}{\sqrt{\Omega_c^2 - 2\omega_z^2}} \right) . \tag{3.27}$$

The full solution may be written as

$$x = |A_+| e^{-\alpha_+} \cos(\tilde{\omega}_+ t + \phi_+) + |A_-| e^{\alpha_-} \cos(\tilde{\omega}_- t + \phi_-), \tag{3.28a}$$

$$y = |A_+| e^{-\alpha_+} \sin(\tilde{\omega}_+ t + \phi_+) + |A_-| e^{\alpha_-} \sin(\tilde{\omega}_- t + \phi_-), \tag{3.28b}$$

where

$$\alpha_{\pm} = \frac{1}{2} \left(F_- \pm \kappa \right) , \tag{3.29a}$$

$$\tilde{\omega}_{\pm} = \frac{1}{2} \left(\Omega_c \pm F_+ \right) . \tag{3.29b}$$

The amplitude of the cyclotron motion decays in time with a time constant of α_+ however, as stated earlier, the removal of energy from the magnetron motion causes the amplitude to increase in time with a time constant of α_-. This behaviour is shown in figure 3.6 by the blue solid line[‡]. As $\alpha_+ >> \alpha_-$ the magnetron motion is often considered to be quasi-stable.

Equation 3.23c is solved trivially by

$$z = A_z e^{-\kappa t} \cos\left(\omega_z t + \phi_z\right) . \tag{3.30}$$

The axial motion is therefore described by a damped harmonic oscillator.

[‡] The values of damping coefficient and frequencies used to produce this image are not typical for a particle in a Penning-type trap but were chosen to illustrate the important features over reasonable length scales.

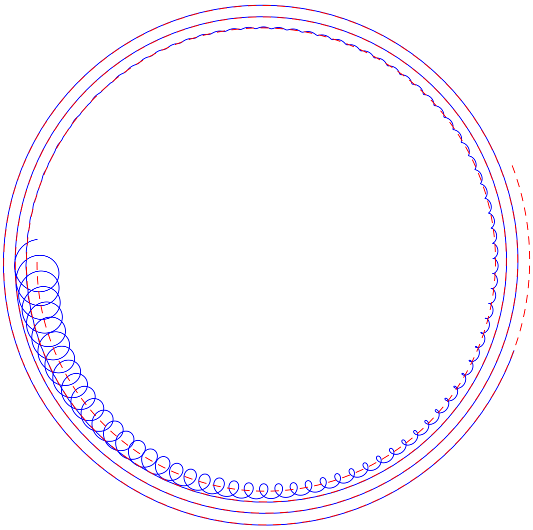

Figure 3.6: The motion of a charged particle in a Penning trap with buffer gas cooling modelled as a Stokes' viscous drag term. The solid blue line is the full motion, while the red dashed line represents a guiding centre approximation.

3.1.4 Guiding Centre Approximation

For most particles in Penning-type traps the cyclotron motion is far faster and of a smaller radius than the magnetron motion. It is often possible to maintain the mean behaviour of a particle in the Penning-type trap while neglecting the fast cyclotron motion: a guiding centre approximation. As an example, the motion of a charged particle in a Penning-type trap in the presence of a frictional or drag term is presented. A Stokes' viscous drag term modifies equation 3.14 to

$$\dot{\mathbf{V}}^{\pm} = \omega_{\pm}\hat{\boldsymbol{z}} \times \mathbf{V}^{\pm} - \kappa\left(\mathbf{V}^{\pm} + \frac{\omega_{\mp}}{\omega_{+} - \omega_{-}}\left(\mathbf{V}^{+} - \mathbf{V}^{-}\right)\right). \tag{3.31}$$

As stated, in a guiding centre approximation the faster cyclotron motion is neglected. Thus the above simplifies to

$$\dot{\mathbf{V}^{-}} = \omega_{-}\hat{\boldsymbol{z}} \times \mathbf{V}^{-} + \kappa\left(\frac{\omega_{-}}{\omega_{+} - \omega_{-}}\right)\mathbf{V}^{-}. \tag{3.32}$$

This represents a slowly expanding circular motion, as shown in figure 3.6 by the red dashed line.

3.2 Positron Accumulation

The Surko-type positron accumulator uses a series of cylindrical electrodes, similar to the cylindrical Penning trap, to produce an electric potential well confining the positrons axially, while a uniform magnetic field provides radial confinement. The classic Surko design uses three stages of varying diameter electrodes with differential pumping to produce three pressure regimes.

The Swansea positron group and Greaves and Moxom simultaneously developed the use of a smaller two-stage accumulator [51, 52]. The design of the Swansea accumulator, detailed in section 2.2, was governed by its physical application; namely to maximise the positron yields at a 10 Hz repetition rate to match that of the laser system (detailed in section 1.2.1).

The accumulator is usually operated in an accumulate-hold-expel sequence as illustrated in figure 3.7. Upon expulsion, the positrons annihilate on a target

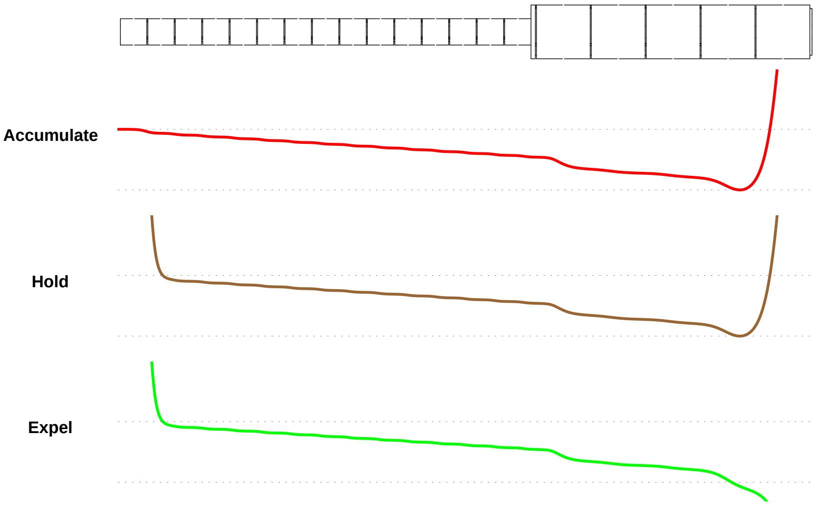

Figure 3.7: Schematic of the cylindrical electrodes of the Swansea two-stage positron accumulator with the axial electrical potentials at each stage of operation: accumulate; hold; expel.

placed in the path of the ejected cloud and the resultant gammas are detected using a CsI coupled to a photodetector.

During accumulation, positrons enter the accumulator over the small potential lip and, using the correct nitrogen buffer gas pressure, will collide with a nitrogen molecule during their first pass of the accumulator. Each collision results in an average energy loss by the positron of ~ 9 eV due primarily to the electronic excitation of the nitrogen molecules [53]. Trapping is negligible for positrons with an energy less than 8 eV; above 11 eV the formation of positronium is as efficient at causing the loss of positrons as electronic excitation is at trapping them. Thus a small trapping window of a few eV wide exists for efficient trapping.

Given a positron trapping rate $R = I_0\epsilon$ e$^+$ s^{-1} (where I_0 is the intensity of the incoming beam and ϵ is the positron capture efficiency) and a positron lifetime of τ the number of accumulated positrons as a function of time is given by the differential equation

$$\frac{dn}{dt} = R - \frac{n}{\tau}, \tag{3.33}$$

such that the number of accumulated positrons within the trap at any time is given by

$$n(t) = R\tau\left(1 - e^{-\frac{t}{\tau}}\right). \tag{3.34}$$

An example of an accumulation curve following equation 3.34 is shown in figure 3.8. Initially the trap fills at a constant rate before curving off towards saturation given by $n_\infty = R\tau$ when $t >> \tau$. Within 3τ the trap contains over 95% of the potential storage, n_∞.

Information regarding the operation of the positron accumulator may be determined from the pressure dependence of n_∞ and τ. The positron lifetime at low pressures is expected to be inversely proportional to buffer gas pressure (P) as

$$\tau = \frac{1}{\lambda} = \frac{1}{BP}. \tag{3.35}$$

The capture efficiency (ϵ) is expected to behave as

$$\epsilon = f\left(1 - e^{-DP}\right) \tag{3.36}$$

where f is a branching ratio of the cross sections of trapping processes (electronic

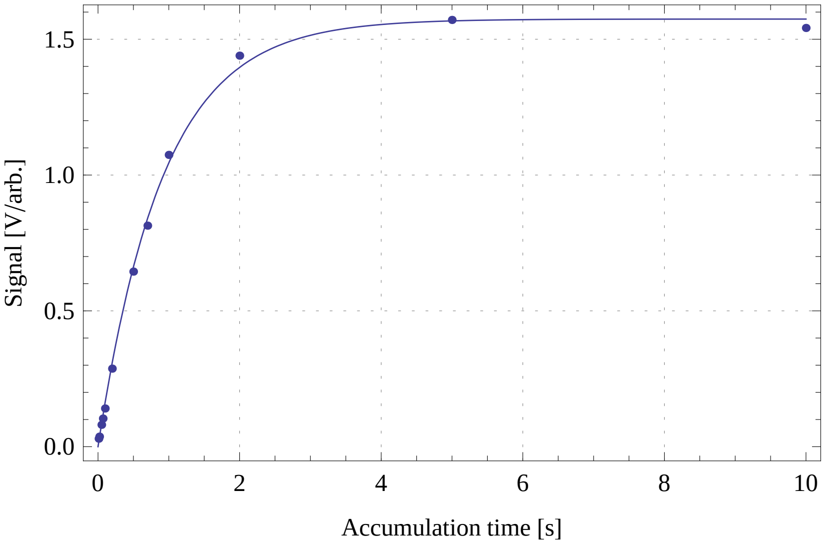

Figure 3.8: An example plot of the number of particles in the trap as a function of accumulation time, $n(t)$, and a fit of the form given in equation 3.34. Fitted parameters are $n_\infty = 1.574 \pm 0.017$ V/arb; $\tau = 0.917 \pm 0.027$ s.

excitation in the positron-N_2 collision case) to processes causing positron loss from the beam (e.g. positronium formation). The constant D is related to the total scattering cross section for positron-N_2 collisions. Thus, an ideal accumulator would have

$$n_\infty = I_0 \frac{f}{BP}\left(1 - e^{-DP}\right). \tag{3.37}$$

However, figure 3.12 shows that the Swansea two-stage accumulator does not follow this behaviour due to an additional loss mechanism. This is an as yet undetermined pressure-dependent loss term believed to originate from the transfer of the positrons from the first to the second stage of the accumulator. It has been found that this can be represented by the generic form $EP/(EP+F)$ where F is a constant and EP is the probability of capture in the second stage. This allows n_∞ to be written as

$$n_\infty = \frac{fI_0E}{B}\left(\frac{1 - e^{-DP}}{EP+F}\right). \tag{3.38}$$

Data recorded using the Swansea two-stage accumulator are shown in figures 3.9–3.12. The fitted parameters cannot be used to determine values for cross sections as the absolute pressure is not measured in the accumulator (as detailed in section 2.2). At high pressures the trap loss rate, λ, as shown in figure 3.10 shows a deviation from the expected linear behaviour given in equation 3.35. This deviation is reproducible and has been reported previously [54], however the cause remains unknown.

Clouds of cold positrons are useful for many applications, including the study of positron-molecule/atom interactions. Although nitrogen has been found to be a very efficient buffer gas to capture positrons it is an inefficient positron cooling gas. Once the positrons are trapped in the second stage they cool to room temperature by vibrational and rotational excitation of the background gas. Table 3.2 shows cooling times due to vibrational excitation as measured by Greaves and Surko using their three stage accumulator for various gases [55].

Figures 3.13 and 3.15 were produced by accumulating for 100 ms and subsequently lowering the exit potential (E5) to varying heights both with and without the presence of SF_6 as a cooling gas. Prior to accumulation the exit potential was grounded to ensure that the trap was empty. These figures therefore represent the complementary cumulative distribution function (CCDF) of the energy of the

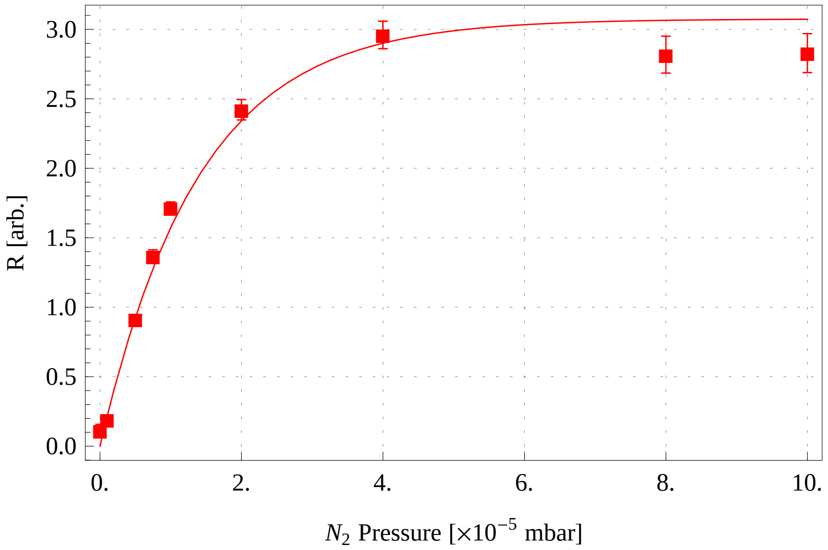

Figure 3.9: A plot of accumulation rate as a function of buffer gas pressure fitted with equation 3.36. Fitted parameters are $fI_0 = 3.07 \pm 0.18$ and $D = 71800 \pm 6300$.

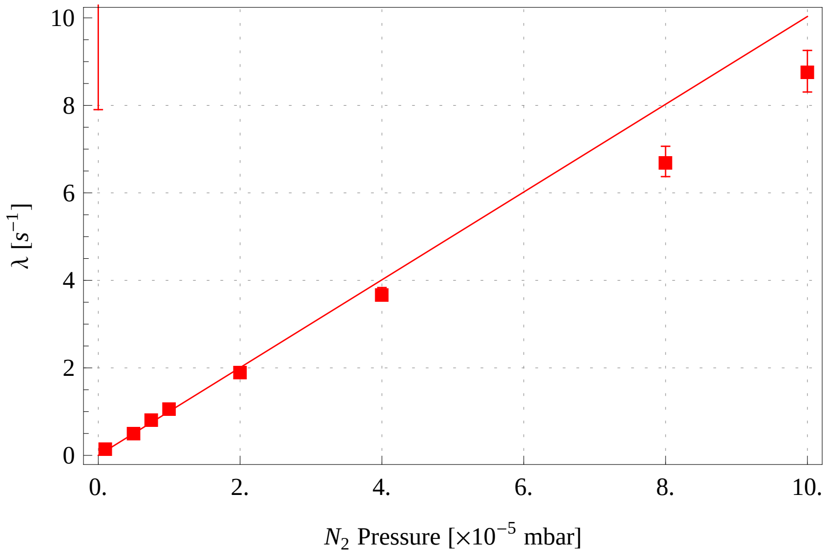

Figure 3.10: A plot of trap loss rate (λ) as a function of buffer gas pressure fitted with $\lambda = 1/\tau = BP$. Fitted parameters are $B = 100300 \pm 5300$ s^{-1} mbar^{-1}.

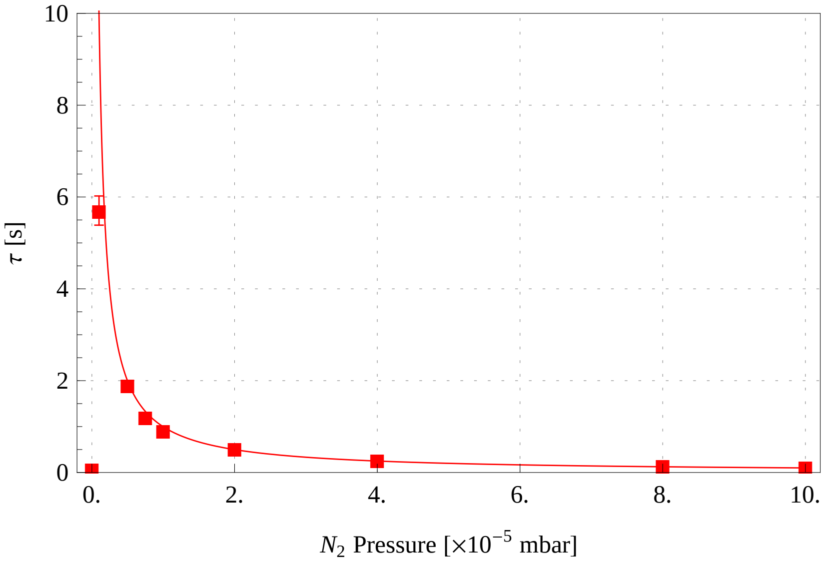

Figure 3.11: A plot of the trap lifetime (τ) as a function of buffer gas pressure fitted with equation 3.35. Fitted parameters are $B = 100300 \pm 5300$ s^{-1} mbar^{-1}.

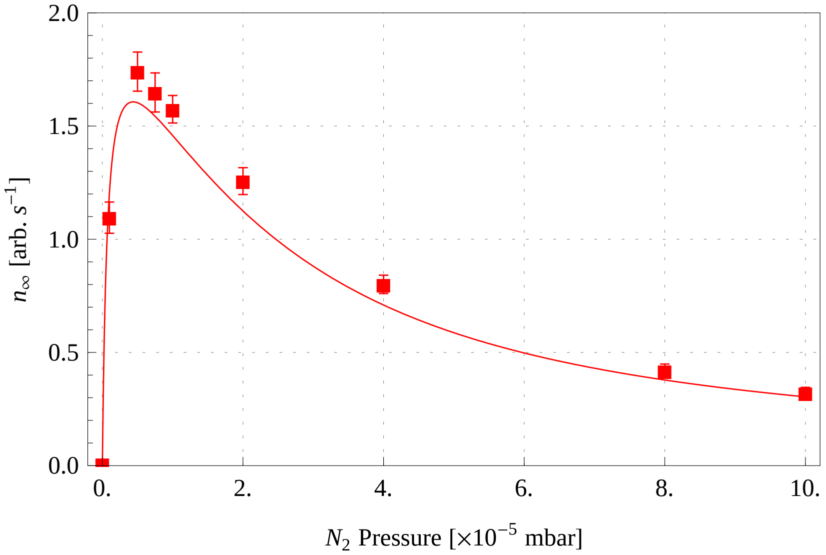

Figure 3.12: A plot of trap saturation, n_∞, as a function of buffer gas pressure fitted with equation 3.38.

Table 3.2: Positron cooling times (τ_c) and annihilation times (τ_a) for a selection of molecular gases at $2{\times}10^{-8}$ Torr and relative trapping efficiencies (ϵ). Data from [55].

Gas	τ_a (s)	τ_c (s)	ϵ
SF_6	2190	0.36	0.07
CF_4	3500	1.2	-
CO_2	3500	1.3	0.16
CO	2400	2.1	0.68
N_2	6300	115	1

positrons in the clouds. The negated derivative of a CCDF gives the energy distribution of the positrons in the clouds which are shown in figures 3.14 and 3.16 with and without SF_6 respectively. Figure 3.14 shows that at 10 Hz operation with SF_6 the accumulator produces a cloud with an energy distribution which has a width of approximatly 0.5 eV: higher than would be expected if the cloud reached room temperature (25 meV). This may be due to electronic noise from the amplifiers or the manner in which the particles are accelerated when released from the trap. Figure 3.16 illustrates the poor cooling effect of N_2 given that the energy distribution has a width of around 5 eV.

3.3 Rotating Wall Electric Fields

The electric potential, u, due to a segmented electrode can be derived using Laplace's equation. With appropriately applied voltages this electrode produces a rotating wall electric field often used to compress plasmas comprised of particles of a single sign of charge.

To calculate the electric potential, u, produced by a segmented electrode, Laplace's equation is solved for a segmented electrode between two end-cap electrodes as shown in figure 3.17. The boundary conditions for this system of electrodes may be defined in cylindrical coordinates (z, r, θ) as

$$u(z, r_0, \theta) = f(\theta)g(z), \tag{3.39}$$

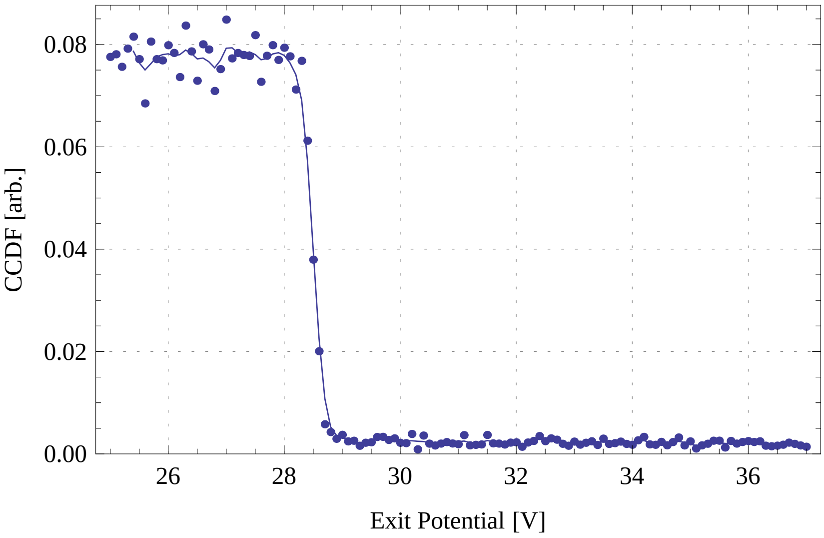

Figure 3.13: The cumulative energy distribution function of the positrons after 100 ms accumulation with both the SF_6 and N_2 pressures at $2{\times}10^{-5}$ mbar. The solid line is not a fit but a smoothed curve to guide the eye.

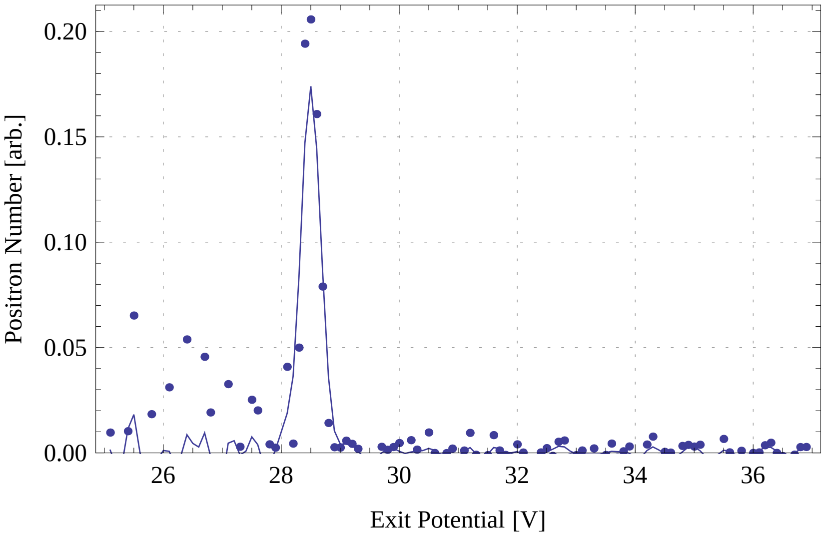

Figure 3.14: The energy distribution of the positrons after 100 ms accumulation with both the SF_6 and N_2 pressures at $2{\times}10^{-5}$ mbar. The solid line is not a fit but a smoothed curve to guide the eye.

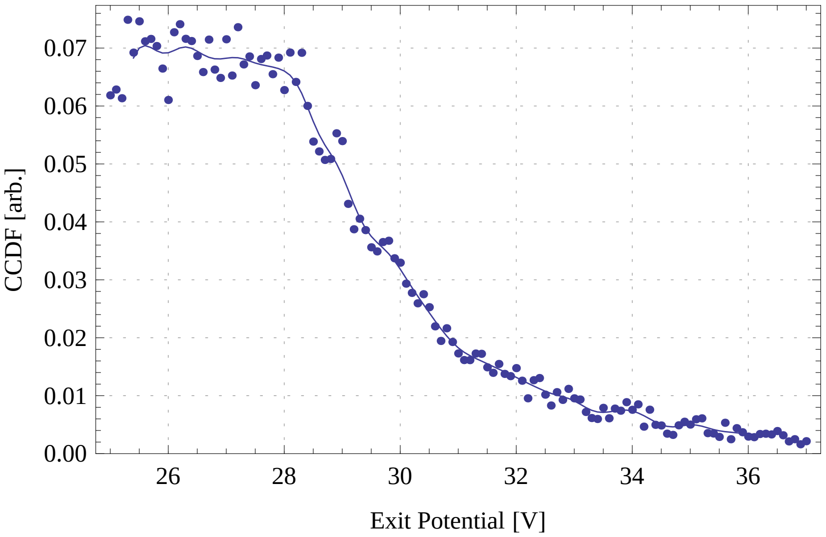

Figure 3.15: The cumulative energy distribution function of the positrons after 100 ms accumulation with the N_2 pressure at 2×10^{-5} mbar. The solid line is not a fit but a smoothed curve to guide the eye.

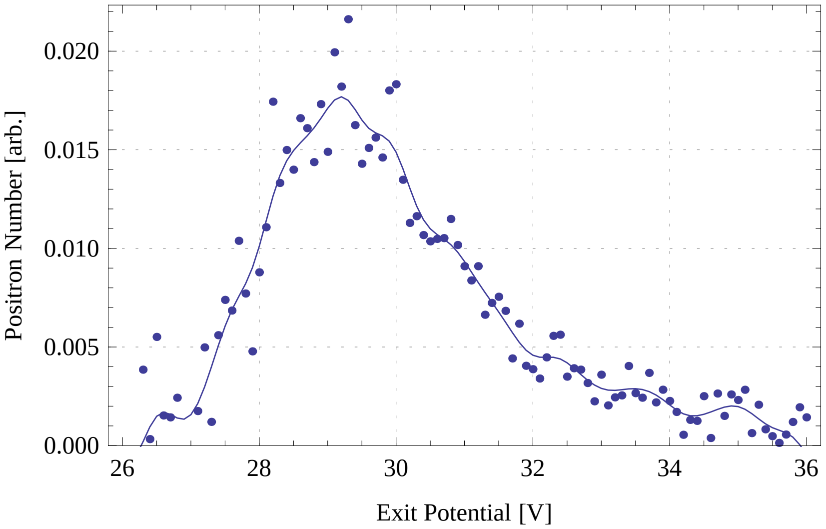

Figure 3.16: The energy distribution of the positrons after 100 ms accumulation with the N_2 pressure at 2×10^{-5} mbar. The solid line is not a fit but a smoothed curve to guide the eye.

Figure 3.17: The segmented electrode, used to produce a rotating wall electric field, for which the electric potential is solved in section 3.3. $V_{a,b}$ are the voltages applied to the segments as shown, z_0 is half the length of the segmented electrode, r_0 is the diameter of the electrodes and L is half the total length of the system: the segmented electrode and the end-caps.

where $f(\theta)$, as shown in figure 3.18, is

$$f(\theta) = \begin{cases} -V_a & -\pi \leq \theta < -\frac{3\pi}{4} \\ -V_b & -\frac{3\pi}{4} \leq \theta < -\frac{\pi}{4} \\ V_a & -\frac{\pi}{4} \leq \theta < \frac{\pi}{4} \\ +V_b & \frac{\pi}{4} \leq \theta < \frac{3\pi}{4} \\ -V_a & \frac{3\pi}{4} \leq \theta < \pi \end{cases} , \tag{3.40}$$

and $g(z)$, as shown in figure 3.19, is given by

$$g(z) = \begin{cases} 1 & |z| \leq z_0 \\ 0 & L > |z| > z_0 \end{cases} . \tag{3.41}$$

The analysis presented here is given explicitly for a four segment electrode but is easily extended to any number of segments by a suitable redefinition of $f(\theta)$.

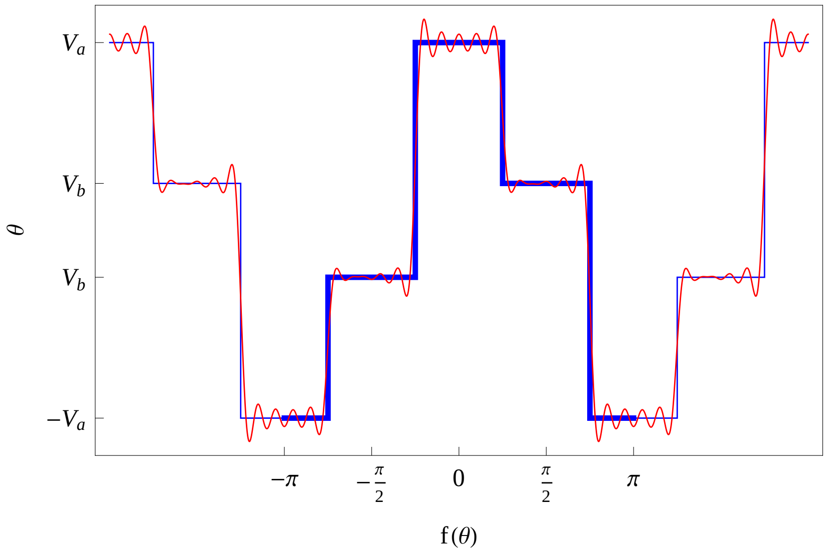

Figure 3.18: Graphical representation of the azimuthal boundary condition defining the rotating wall electrode, $f(\theta)$ (Blue) and its Fourier series, as given by equation 3.55 terminated at 20 terms (Red).

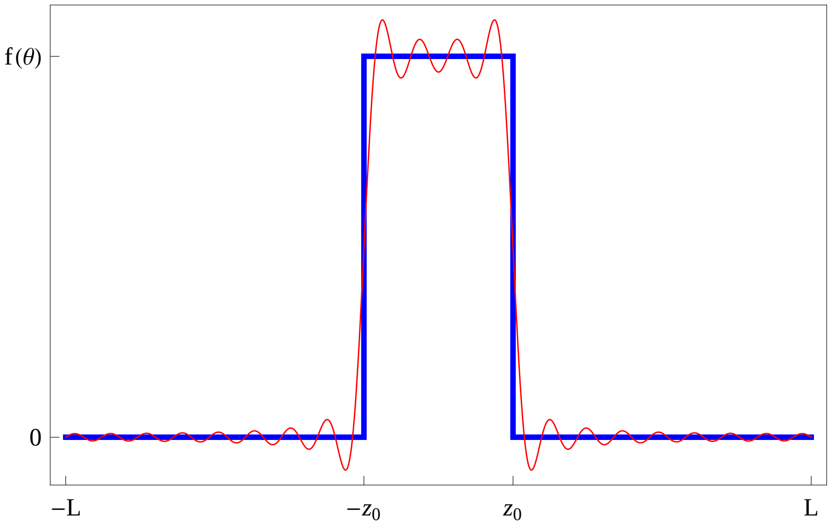

Figure 3.19: Graphical representation of the axial boundary condition defining the rotating wall electrode, $g(z)$ (Blue) and its Fourier series, as given by equation 3.54 terminated at 20 terms (Red).

3.3.1 The General Solution to Laplace's Equation

Laplace's equation states that the concentration of the electric potential ($\nabla^2 u$) is zero. In cylindrical coordinates this is written as

$$\nabla^2 u = \frac{1}{r}\frac{\partial}{\partial r}\left(r\frac{\partial u}{\partial r}\right) + \frac{1}{r^2}\frac{\partial^2 u}{\partial \theta^2} + \frac{\partial^2 u}{\partial z^2} = 0. \tag{3.42}$$

By separation of variables,

$$u(z, r, \theta) = Z(z)R(r)\Theta(\theta), \tag{3.43}$$

equation 3.42 may be written as,

$$\frac{\nabla^2 u}{u} = \frac{1}{R}\frac{1}{r}\frac{d}{dr}\left(r\frac{dR}{dr}\right) + \frac{1}{\Theta}\frac{1}{r^2}\frac{d^2\Theta}{d\theta^2} + \frac{1}{Z}\frac{d^2 Z}{dz^2}. \tag{3.44}$$

This equation is separable into three ordinary differential equations for $Z(z)$, $R(r)$ and $\Theta(\theta)$. First the equation governing $Z(z)$ is

$$\frac{1}{Z}\frac{d^2 Z}{dz^2} = \pm k^2. \tag{3.45}$$

The boundary condition given by equation 3.39 requires that $Z(z)$ tends to a finite value within a finite domain. This is satisfied only by the $-k^2$ and so the $+k^2$ may be dismissed as this would tend to zero as $z \to \infty$. The solution for $Z(z)$ is therefore

$$Z(z) = A\cos(kz) + B\sin(kz). \tag{3.46}$$

Secondly, the equation governing $\Theta(\theta)$ is

$$\frac{1}{\Theta}\frac{d^2\Theta}{d\theta^2} = \pm n^2. \tag{3.47}$$

Since, in cylindrical coordinates, θ is periodic in 2π the negative constant ($-n^2$) must be used with n an integer. This gives

$$\Theta(\theta) = a\cos(n\theta) + b\sin(n\theta). \tag{3.48}$$

The radial dependence is given by $R(r)$,

$$\frac{r}{R}\frac{d}{dr}\left(\frac{dR}{dr}\right) - (k^2r^2 + n^2) = 0 \tag{3.49}$$

which is one of Bessel's equations, with solutions discussed extensively in a number of texts (e.g. [56]). The solutions of interest for this problem are the modified Bessel functions of the first kind of order n, $I_n(x)$, such that

$$R(r) = I_n(kr). \tag{3.50}$$

Laplace's equation is linear and so any linear combination of the solutions given above is also a solution. All solutions of the form given by 3.43 must therefore be summed giving the general solution

$$\begin{aligned} u(z,r,\theta) &= \sum_{n=0}^{\infty}\sum_{m=0}^{\infty} I_n(k_m r)\left(A_{mn}\cos(k_m z) + B_{mn}\sin(k_m z)\right) \\ &\qquad \times \left(a_{mn}\cos(n\theta) + b_{mn}\sin(n\theta)\right). \end{aligned} \tag{3.51}$$

3.3.2 Applying the Boundary Conditions

Equation 3.51 may be simplified by the knowledge that the solution must be symmetric in $z \to -z$. The leads to the constants B_{mn} being zero. Also, as the potential must be zero at $z = L$ this requires

$$k_m = \frac{\left(m + \frac{1}{2}\right)\pi}{L}, \tag{3.52}$$

leading to

$$u(z,r,\theta) = \sum_{n=0}^{\infty}\sum_{m=0}^{\infty} I_n(k_m r) A_{mn}\cos(k_m z)\left(a_{mn}\cos(n\theta) + b_{mn}\sin(n\theta)\right). \tag{3.53}$$

The Fourier series expansions of equations 3.40 and 3.41, (shown graphically in figures 3.18 and 3.19) yield:

$$g(z) = \sum_{m=0}^{\infty} \frac{2}{k_m L} \sin(k_m z_0) \cos(k_m z) \tag{3.54}$$

and

$$\begin{aligned} f(\theta) \quad = \quad & \sum_{n=1}^{\infty} \frac{4}{n\pi} \Big(V_a \sin\left(\frac{n\pi}{2}\right) \cos\left(\frac{n\pi}{4}\right) \cos(n\theta) \\ & \qquad + V_b \sin\left(\frac{n\pi}{2}\right) \sin\left(\frac{n\pi}{4}\right) \sin(n\theta) \Big). \end{aligned} \tag{3.55}$$

Substituting the Fourier transforms of the boundary conditions into equation 3.53 and equating the coefficients of $\sin(n\theta)$, $\cos(n\theta)$ and $\cos(k_m z)$ in each term defines the coefficients a_{mn}, b_{mn} and A_{mn}. This gives the solution as

$$u(z, r, \theta) = \sum_{n=0}^{\infty} \sum_{m=0}^{\infty} A_{mn} I_n(k_m r) \cos(k_m z) \left(a_n \cos(n\theta) + b_n \sin(n\theta)\right) \tag{3.56}$$

with

$$a_n = \frac{4V_a}{n\pi} \left(\sin\left(\frac{n\pi}{2}\right) \cos\left(\frac{n\pi}{4}\right) \right), \tag{3.57a}$$

$$b_n = \frac{4V_b}{n\pi} \left(\sin\left(\frac{n\pi}{2}\right) \sin\left(\frac{n\pi}{4}\right) \right), \tag{3.57b}$$

$$A_{mn} = \begin{cases} 0 & n = 0 \\ \frac{2}{k_m L} \frac{\sin(k_m z_0)}{I_n(k_m r_0)} & n \neq 0 \end{cases}, \tag{3.57c}$$

with k_m defined by equation 3.52.

3.3.3 Small Radius Approximation for a Rotating Wall Electrode

In producing a rotating wall electric field, sinusoidally varying potentials are placed on the four segments in quadrature (i.e. each offset by a phase of 90° with respect to the previous one). Thus

$$
\begin{aligned}
V_a &= V_r \cos(\omega_r t) && \text{(3.58a)}\\
V_b &= -V_r \sin(\omega_r t). && \text{(3.58b)}
\end{aligned}
$$

Where V_r is the amplitude of the rotating wall. Note that the choice of a minus sign for V_b is a matter of convenience relating to the direction of rotation. The full rotating wall electric potential is shown in figure 3.20.

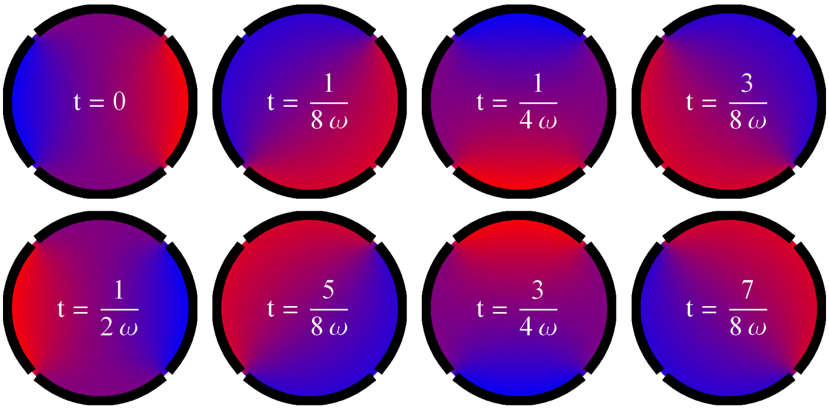

Figure 3.20: The complete electric potential produced by a rotating wall electrode evolving in time. Red represents a higher potential while blue represents a lower potential.

The expansion of a modified Bessel function of the first kind of order n is given by

$$I_n(x) = \sum_{l=0}^{\infty} \frac{1}{l!\Gamma(n+l+1)} \left(\frac{x}{2}\right)^{2l+n} \tag{3.59}$$

Since the sum in equation 3.56 runs over $1 \leq n \leq \infty$ the only term contributing to leading order r is when $n = 1$ and $l = 0$. Thus the small radius (leading r term) solution is a dipole electric field which may be written as

$$u(z, r \ll r_0, \theta) \approx V_r \left(\frac{2\sqrt{2}}{\pi L} \sum_{m=0}^{\infty} \frac{\cos(k_m z)\sin(k_m z_0)}{I_1(k_m r_0)} \right) r\cos(\omega_r t + \theta) \tag{3.60}$$

Figure 3.21 shows the electric potential at the centre of the rotating wall electrode. The electric field is spatially uniform and rotates about the electrode axis in time. This is represented by the white arrows of figure 3.21. This formalism is used in the next chapter to compare a theoretical model based on a rotating dipole electric field, with experimental results obtained using the rotating wall electrode installed in the accumulator (as detailed in section 2.2).

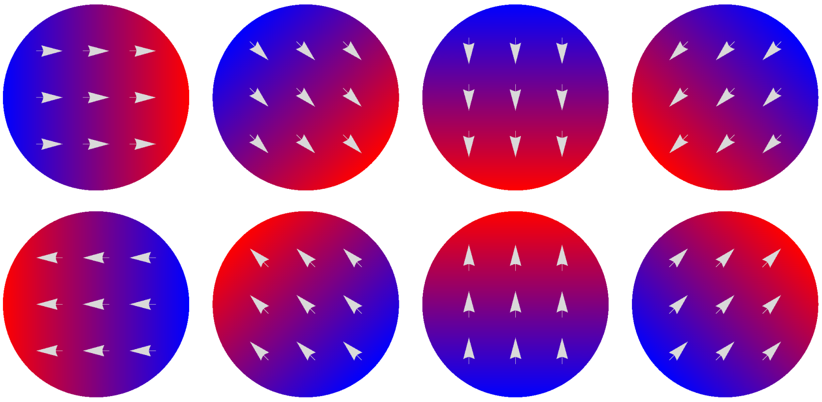

Figure 3.21: The electric potential produced at the centre of a rotating wall electrode showing a dipole behaviour. Red represents a more positive potential while blue, a more negative one. The white arrows represent the electric field.

Chapter 4

Charged Cloud Compression

"Prediction is very difficult, especially if it's about the future"

— *Neils Bohr*

Inspired by the work of Greaves and Moxom [24], a possible mechanism for particle axialisation in a Penning-type trap using a rotating electric field has been developed. Greaves and Moxom used an electrode split into eight segments to produce a rotating quadrupole field. The Swansea positron accumulator has only four segments and thus produces a rotating dipole field. In each case the rotating electric field is applied asymetrically over the cloud resulting in compression. A model has been developed for the case of the rotating dipole field to describe the compression process. This model is then used to account for some of the experimental results obtained using the Swansea positron accumulator.

4.1 Compression Model

As shown in section 3.3.3 a 4-segment electrode may, with the application of appropriate potentials, be used to produce a rotating dipole electric field in the radial plane. Laplace's equation, $\nabla^2 u = 0$, allows for three axial behaviours of a dipole potential: the uninteresting null, no potential; the constant, independent of z; the linear, proportional to z, referred to as the asymmetric. Greaves and Moxom found that applying the rotating wall electric field symmetrically over the cloud resulted in no compression [24] and therefore the assymetric case is considered in the analysis which follows.

The Penning trap potential, as given in equation 3.1, with a superimposed asymmetric rotating dipole is given by

$$\phi(z,r,\theta) = \frac{V_0}{2d^2}\left(z^2 - \frac{r^2}{2}\right) + \frac{m}{q} azr\cos\left(\theta + \omega_r t\right), \tag{4.1}$$

where ω_r is the angular frequency and a is the amplitude of the rotating dipole. Inserting this potential into the Lorentz equation along with the addition of a viscous drag term, as presented in section 3.1.3, gives

$$\begin{aligned} \ddot{z} + \omega_z^2 z - \mathbf{r}\cdot\mathbf{R} + \kappa\dot{z} &= 0, & \text{(4.2a)} \\ \ddot{\mathbf{r}} - \Omega_c \hat{\boldsymbol{z}} \times \dot{\mathbf{r}} - \frac{\omega_z^2}{2}\mathbf{r} + \kappa\dot{\mathbf{r}} + \mathbf{R}z &= 0, & \text{(4.2b)} \end{aligned}$$

where

$$\mathbf{R} = a\begin{bmatrix} \cos\left(\omega_r t\right) \\ -\sin\left(\omega_r t\right) \end{bmatrix}. \tag{4.3}$$

4.1.1 The Complete Solution in Cartesian Coordinates

Equation 4.2 may be written in Cartesian coordinates as

$$\begin{aligned} \ddot{x} &= \frac{\omega_z^2}{2}x - a\cos\left(\omega_r t\right)z + \Omega\dot{y} - \kappa\dot{x}, & \text{(4.4a)} \\ \ddot{y} &= \frac{\omega_z^2}{2}y + a\sin\left(\omega_r t\right)z - \Omega\dot{x} - \kappa\dot{y}, & \text{(4.4b)} \\ \ddot{z} &= -\omega_z^2 z - a\left(x\cos\left(\omega_r t\right) - y\sin\left(\omega_r t\right)\right) - \kappa\dot{z}. & \text{(4.4c)} \end{aligned}$$

By a transformation into coordinates which are co-rotating with the electric field given by,

$$\begin{aligned} x &= \left(\tilde{\xi}\cos\left(\omega_r t\right) + \tilde{\psi}\sin\left(\omega_r t\right)\right), && (4.5a)\\ y &= \left(\tilde{\psi}\cos\left(\omega_r t\right) - \tilde{\xi}\sin\left(\omega_r t\right)\right), && (4.5b)\end{aligned}$$

the equations of motion may be written as a set of coupled linear differential equations as

$$\begin{aligned} \ddot{\tilde{\xi}} &= \frac{1}{2}\left(2\omega_r^2 - 2\Omega\omega_r + \omega_z^2\right)\tilde{\xi} - \kappa\omega_r\tilde{\psi} - \kappa\dot{\tilde{\xi}} + \left(\Omega - 2\omega_r\right)\dot{\tilde{\psi}} - az, && (4.6a)\\ \ddot{\tilde{\psi}} &= \kappa\omega_r\tilde{\xi} + \frac{1}{2}\left(2\omega_r^2 - 2\Omega\omega_r + \omega_z^2\right)\tilde{\psi} - \left(\Omega - 2\omega_r\right)\dot{\tilde{\xi}} - \kappa\dot{\tilde{\psi}}, && (4.6b)\\ \ddot{z} &= -a\tilde{\xi} - \omega_z^2 z - \kappa\dot{z}, && (4.6c)\end{aligned}$$

or in matrix form, $\dot{\mathbf{x}} = \mathcal{M}\cdot\mathbf{x}$, as

$$\begin{bmatrix} \dot{\tilde{\xi}} \\ \dot{\tilde{\psi}} \\ \dot{z} \\ \ddot{\tilde{\xi}} \\ \ddot{\tilde{\psi}} \\ \ddot{z} \end{bmatrix} = \begin{bmatrix} 0 & 0 & 0 & 1 & 0 & 0 \\ 0 & 0 & 0 & 0 & 1 & 0 \\ 0 & 0 & 0 & 0 & 0 & 1 \\ b & -c & -a & -\kappa & d & 0 \\ c & b & 0 & -d & -\kappa & 0 \\ -a & 0 & -\omega_z^2 & 0 & 0 & -\kappa \end{bmatrix} \cdot \begin{bmatrix} \tilde{\xi} \\ \tilde{\psi} \\ z \\ \dot{\tilde{\xi}} \\ \dot{\tilde{\psi}} \\ \dot{z} \end{bmatrix}, \qquad (4.7)$$

where

$$\begin{aligned} b &= \frac{1}{2}\left(2\omega_r^2 - 2\Omega\omega_r + \omega_z^2\right), && (4.8a)\\ c &= \kappa\omega_r, && (4.8b)\\ d &= \Omega - 2\omega_r. && (4.8c)\end{aligned}$$

The matrix $\mathcal{M}$ has eigenvalues given by the characteristic equation

$$\begin{aligned} &a^2(b - \lambda(\kappa+\lambda)) + \left(\lambda(\kappa+\lambda) + \omega_z^2\right)\\ &\qquad \times\left(b^2 - 2b\lambda(\kappa+\lambda) + c(c - 2d\lambda) + \lambda^2\left(d^2 + (\kappa+\lambda)^2\right)\right) = 0. \qquad (4.9)\end{aligned}$$

This characteristic equation is a hexic (sixth order) polynomial in λ and by Galois theory its roots cannot be written in a closed analytic form. Its roots can however be investigated numerically. Figure 4.1 shows the typical form of the eigenvalues as the rotating wall angular frequency is changed. The shapes of these frequency responses are investigated further in the next section, however it is worth noting that the root corresponding to λ_5 in figure 4.1 has an imaginary part, representing a frequency, which is similar in magnitude to the cyclotron frequency.

The full solution to equations 4.6 may be written as

$$\mathbf{x} = \sum_{i=1}^{6} \gamma_i \mathbf{v}_i \exp\left(\lambda_i t\right) \tag{4.10}$$

where $\mathbf{v}_i$ is the eigenvector associated with the eigenvalue λ_i, and the γ_i are determined from the initial conditions.

4.1.2 An Approximate Solution in $\mathbf{V}^{\pm}$ Coordinates

As was shown in section 3.1.2, the magnetron and cyclotron motions of a charged particle in a Penning trap may be separated using the $\mathbf{V}^{\pm}$ coordinates defined by equation 3.13. The analysis presented in the previous section is now repeated in the $\mathbf{V}^{\pm}$ coordinates allowing approximations to be made more easily.

In the $\mathbf{V}^{\pm}$ coordinates equations 4.2 may be written as

$$\dot{V}_x^{\pm} = -\omega_{\pm} V_y^{\pm} - \kappa \left(V_x^{\pm} + \frac{\omega_{\mp}}{\omega_+ - \omega_-} \left(V_x^+ - V_x^- \right) \right) - az \cos\left(\omega_r t\right), \tag{4.11a}$$

$$\dot{V}_y^{\pm} = \omega_{\pm} V_x^{\pm} - \kappa \left(V_y^{\pm} + \frac{\omega_{\mp}}{\omega_+ - \omega_-} \left(V_y^+ - V_y^- \right) \right) + az \sin\left(\omega_r t\right), \tag{4.11b}$$

$$\ddot{z} = -\omega_z^2 z - \kappa \dot{z} + \frac{a}{\omega_+ - \omega_-} \Big(\left(V_y^- - V_y^+ \right) \cos\left(\omega_r t\right) - \left(V_x^+ - V_x^- \right) \sin\left(\omega_r t\right) \Big) \tag{4.11c}$$

Since $\mathbf{V}^+$ ($\mathbf{V}^-$) resonates at ω_+ (ω_-) it can be seen that only the V^- motion will be effected by rotating wall frequencies, ω_r, close to the axial bounce frequency, ω_z. Therefore, employing the guiding centre approximation by neglecting the rapid cyclotron motion shows the magnetron behaviour is governed

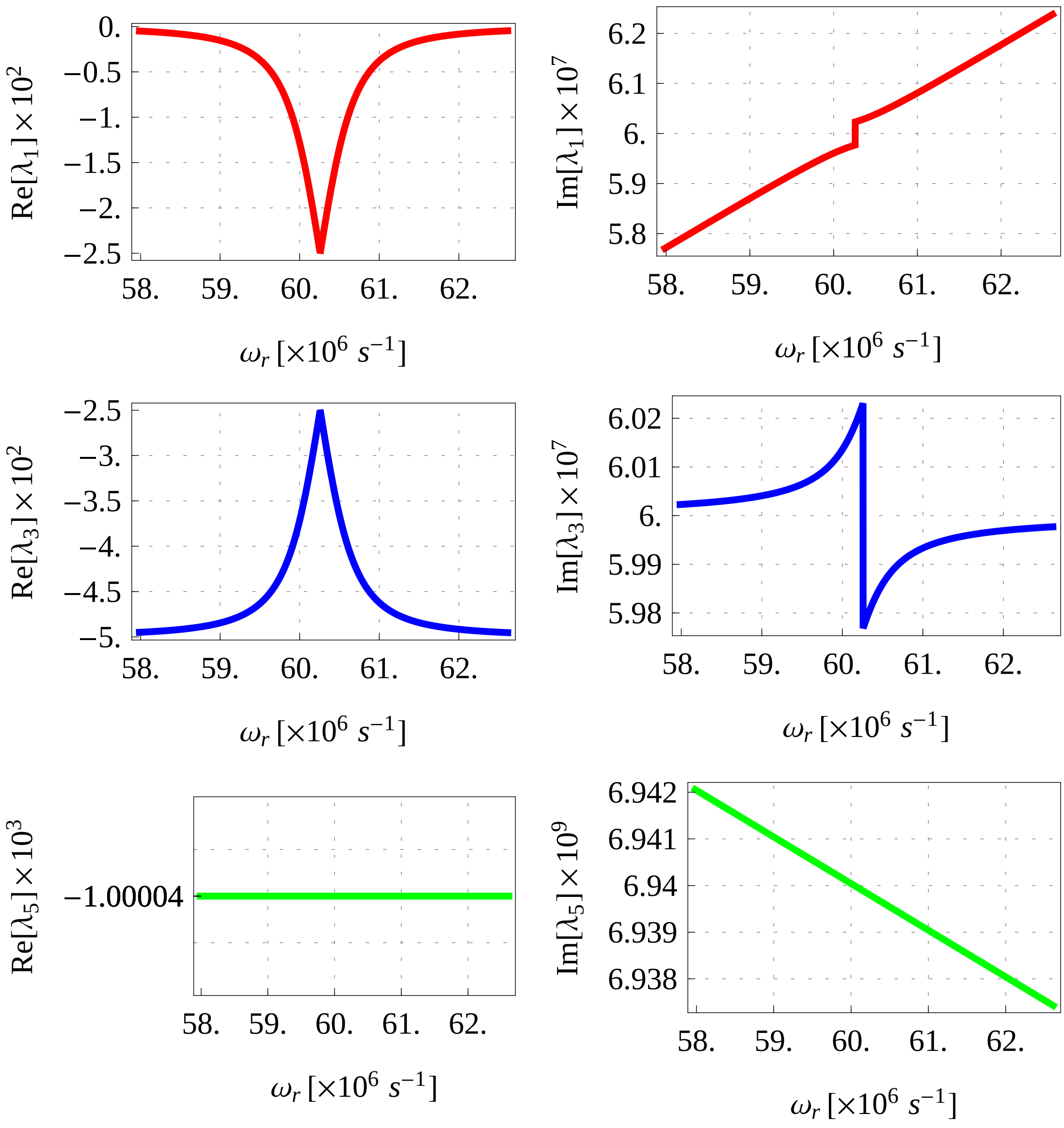

Figure 4.1: The roots of the hexic polynomial given in equation 4.9. As the roots always occur in complex conjugate pair, i.e.($\lambda_1 = \lambda_2^*$), only the positive solution for the imaginary part is shown. Model parameters were chosen to be experimentally realistic: $a = 3\times10^{14}$ s^{-2}; $\Omega = 7\times10^9$ s^{-1}; $\omega_z = 6\times10^7$ s^{-1}; $\kappa = 1000$ s^{-1}

by

$$\begin{aligned}
\dot{V}_x^- &= -\omega_- V_y^- + \kappa \frac{\omega_-}{\omega_+ - \omega_-} V_x^- - az\cos(\omega_r t) &\text{(4.12a)}\\
\dot{V}_y^- &= \omega_- V_x^- + \kappa \frac{\omega_-}{\omega_+ - \omega_-} V_y^- + az\sin(\omega_r t) &\text{(4.12b)}\\
\ddot{z} &= -\omega_z^2 z - \kappa\dot{z} + \frac{a}{\omega_+ - \omega_-}\left(V_y^- \cos(\omega_r t) + V_x^- \sin(\omega_r t)\right). &\text{(4.12c)}
\end{aligned}$$

Typically $\omega_+ >> \omega_- >> \kappa$, so the damping terms in equation 4.12a and 4.12b are very small and may therefore be neglected. As was noted earlier in section 3.1.3, the expansion of the motion the magnetron orbit is far slower than other time scales and may therefore be considered as quasi-stable.

A transformation into coordinates which co-rotate with the rotating wall electric field as given by,

$$\begin{aligned}
V_x^- &= \xi\cos(\omega_r t) + \psi\sin(\omega_r t) &\text{(4.13a)}\\
V_y^- &= \psi\cos(\omega_r t) - \xi\sin(\omega_r t), &\text{(4.13b)}
\end{aligned}$$

allows equations 4.12 to be written as a set of coupled linear ordinary differential equations as

$$\begin{aligned}
\dot{\xi} &= -(\omega_- + \omega_r)\psi - az, &\text{(4.14a)}\\
\dot{\psi} &= (\omega_- + \omega_r)\xi, &\text{(4.14b)}\\
\ddot{z} &= \frac{a}{\omega_+ - \omega_-}\psi - \omega_z^2 z - \kappa\dot{z}, &\text{(4.14c)}
\end{aligned}$$

or in matrix form $\dot{\mathbf{x}} = \mathcal{M}\cdot\mathbf{x}$ as

$$\begin{bmatrix} \dot{\xi} \\ \dot{\psi} \\ \dot{z} \\ \ddot{z} \end{bmatrix} = \begin{bmatrix} 0 & -(\omega_- + \omega_r) & -a & 0 \\ (\omega_- + \omega_r) & 0 & 0 & 0 \\ 0 & 0 & 0 & 1 \\ 0 & \frac{a}{\omega_+ - \omega_-} & -\omega_z^2 & -\kappa \end{bmatrix} \cdot \begin{bmatrix} \xi \\ \psi \\ z \\ \dot{z} \end{bmatrix} \tag{4.15}$$

with eigenvalues given by the characteristic equation

$$a^2(\omega_r + \omega_-) + (\omega_+ - \omega_-)\left(\lambda^2 + (\omega_r + \omega_-)^2\right)\left(\lambda(\lambda + \kappa) + \omega_z^2\right) = 0. \tag{4.16}$$

The solution to equations 4.14 may be written as

$$\mathbf{x} = \sum_{i=1}^{4} \gamma_i \mathbf{v}_i \exp\left(\lambda_i t\right), \tag{4.17}$$

where $\mathbf{v}_i$ is the eigenvector associated with the eigenvalue λ_i and the γ are determined from the initial conditions. Given that the coefficients of the polynomial in equation 4.16 are all real, the roots must appear in complex conjugate pairs. Using the identity

$$\alpha \exp\left(\beta t\right) + \alpha^* \exp\left(\beta^* t\right) = 2\left|\alpha\right|^2 \exp\left(\mathrm{Re}\left[\beta\right] t\right) \cos\left(\mathrm{Im}\left[\beta\right] t - \angle\left[\alpha\right]\right), \tag{4.18}$$

it may be seen that the motion in this rotating coordinate frame is given by a series of damped circular motions with frequencies and damping rates given by the imaginary and real parts of the eigenvalues respectively.

The characteristic equation is a quartic (fourth order) polynomial in λ, the roots of which may be written in a closed analytic form. However this is long and cumbersome and so it was felt that some numerical investigations would be worthwhile. A common approach in resonance type effects is to investigate the dependence of the system on the driving frequency: a frequency scan. Applying the same principle, using equation 4.16, graphs such as the one shown in figure 4.2 were produced. It was observed that the shapes of these graphs could be described by the function:

$$\lambda = \tilde{A}\left(1 \pm \left|\frac{\tilde{\omega}}{\sqrt{1+\tilde{\omega}^2}}\right|\right) \pm \mathbf{i}\left(\tilde{B}\left(\tilde{\omega} \pm \left|\sqrt{1+\tilde{\omega}^2}\right|\right) + \tilde{C}\right), \tag{4.19}$$

where the constant $\tilde{A}$ equals a quarter of the damping parameter, $\kappa/4$, and the constant $\tilde{C}$ is equal to the axial bounce frequency of the system, ω_z. Two additional parameters were introduced to allow the central position, ω_0, and width, δ, of the function to be varied. These were introduced as

$$\tilde{\omega} = \frac{\omega_r - \omega_0}{\delta}. \tag{4.20}$$

From equation 4.19 the full width at half maximum of this function may be

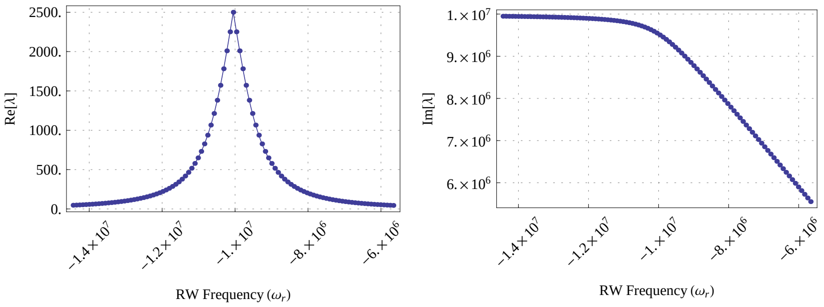

Figure 4.2: The real and imaginary parts of the roots of interest given by equation 4.16 (filled circles) along with a fit of the forms given by equations 4.23 giving δ=875.52±0.44 kHz (line). Other parameters were κ=10,000 s^{-1}; a=8.8×10^{13} s^{-2}; ω_z=10^7 s^{-1}; Ω=10^9 s^{-1}.

derived as

$$\mathrm{FWHM} = \frac{2}{\sqrt{3}}\delta. \tag{4.21}$$

The central frequency, ω_0, corresponds to the frequency at which the real part of the eigenvalues is extremised. This was found to lie at the negated sum of the magnetron and bounce frequencies as

$$\omega_0 = -\left(\omega_z + \omega_m\right). \tag{4.22}$$

The variation of the width parameter, δ, was determined by fitting the numerically calculated roots of equation 4.16 with the function given in equation 4.19 with varying system parameters: κ, a, ω_z and Ω. The damping parameter, κ, was found to have no effect on the response width, δ. The results of the remaining parameter variations were plotted on a log-log scale and fitted with a linear function to determine a power law dependence (see figure 4.3). In each scan the fixed parameters were chosen to be experimentally realistic values: damping parameter, κ=10,000 s^{-1}; amplitude a=500$^{e}/_{m}$=8.8×10^{13} s^{-1}; bounce frequency, ω_z=10^7 s^{-1}; cyclotron frequency, Ω=10^9 s^{-1}. From this it was determined that the width, δ, was proportional to the applied amplitude, a, and was inversely proportional to the root of the product of the bounce and cyclotron frequencies.

It was observed that the constant $\tilde{B}$ equals half the width parameter and so,

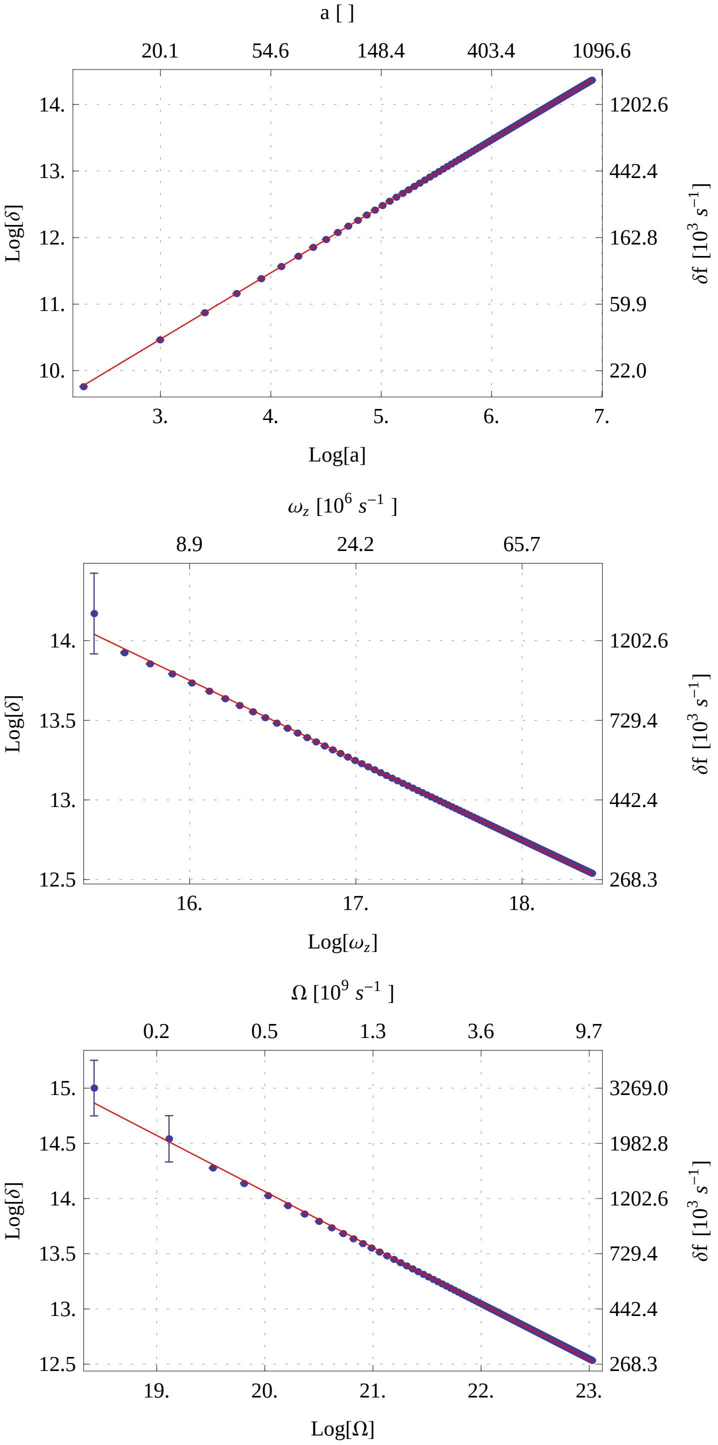

Figure 4.3: Fits to the frequency response width, δ, as system parameters were changed presented on a log-log scale. Top: Amplitude, a. Middle: Bounce frequency, ω_z. Bottom: Cyclotron frequency, Ω. The values from the linear fits may be seen in table 4.1.

Table 4.1: The gradients and intercepts of the linear fits shown in figure 4.3. The gradients of these fits yield the power law dependence of the frequency response width, δ on the varied parameters: a, ω_z and Ω.

Varied Parameter	Gradient	Intercept
Amplitude, a	0.99815±0.00055	7.4744±0.0036
Bounce Frequency, ω_z	-0.5025±0.0020	21.791±0.035
Cyclotron Frequency, Ω	-0.5076±0.0017	24.216±0.038

being careful to maintain the correct root associations*, the eigenvalues may be approximated by

$$\lambda = \frac{\kappa}{4}\left(-1 \pm_s \sqrt{\frac{\tilde{\omega}^2}{1+\tilde{\omega}^2}}\right) \pm_t \mathbf{i}\left(\frac{\delta}{2}\left(\tilde{\omega} \mp_s \tilde{\omega}\sqrt{\frac{1+\tilde{\omega}^2}{\tilde{\omega}^2}}\right) + \omega_z\right), \tag{4.23}$$

where

$$\tilde{\omega} = \frac{\omega_r + (\omega_z + \omega_-)}{\delta}, \tag{4.24a}$$

$$\delta = \frac{a}{\sqrt{\Omega\omega_z}}. \tag{4.24b}$$

Both the real and imaginary parts of this approximate solution have been plotted in figure 4.4.

Figure 4.5 follows the radial distance, $\sqrt{x^2+y^2}$, of a particle given the solution found. As reference, this figure also shows the damping rate related to λ_1 and λ_2 as assigned in figure 4.4. Thus, it is the damping of the slower oscillation, $\mathrm{Re}\left[\lambda_2\right]$, which gives a measure of the axialisation rate of the particle, while λ_2 gives the damping rate of the rapid oscillation. It is therefore possible to write the axialisation rate, or compression rate in the case of a cloud, as

$$\Gamma = \frac{\kappa}{4}\left(1 - \left|\frac{\tilde{\omega}}{\sqrt{1+\tilde{\omega}^2}}\right|\right). \tag{4.25}$$

This is a cusped shaped function and will be compared with experimental results

---

[*] The shorthand notation $\pm_{s,t}$ is used to distinguish between valid ± combinations.

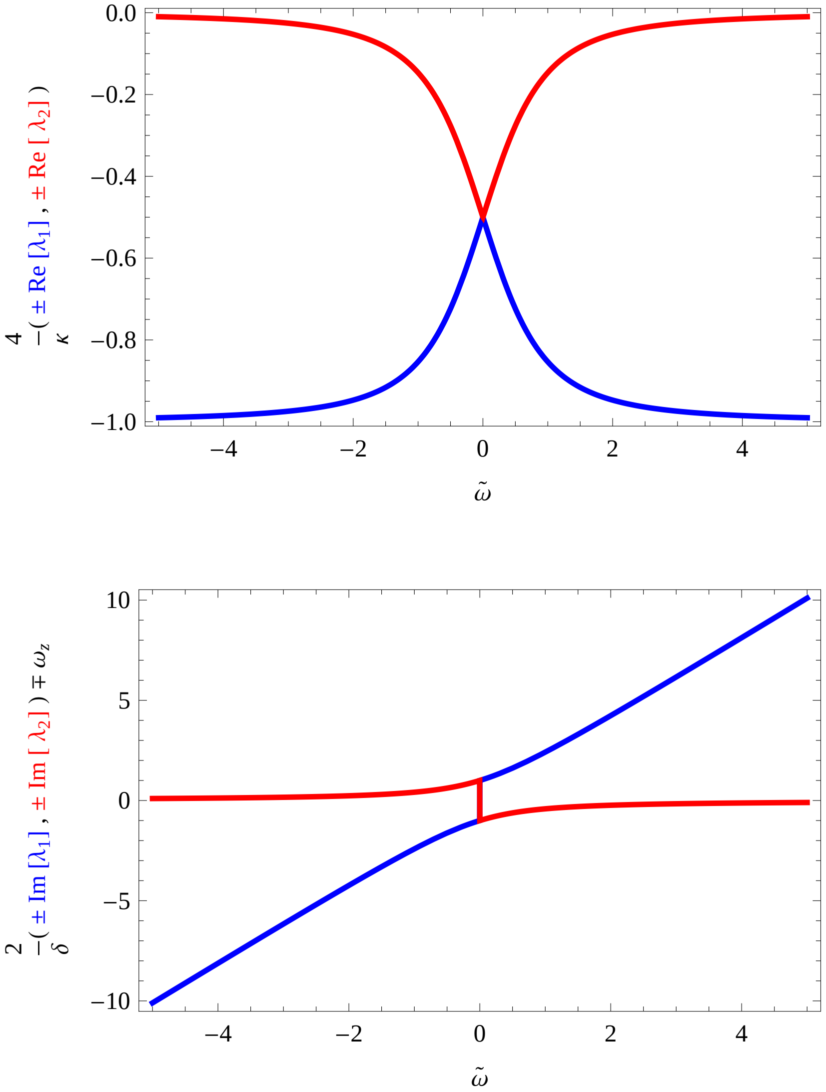

Figure 4.4: Approximate rotating wall eigenvalues as given by equation 4.23.

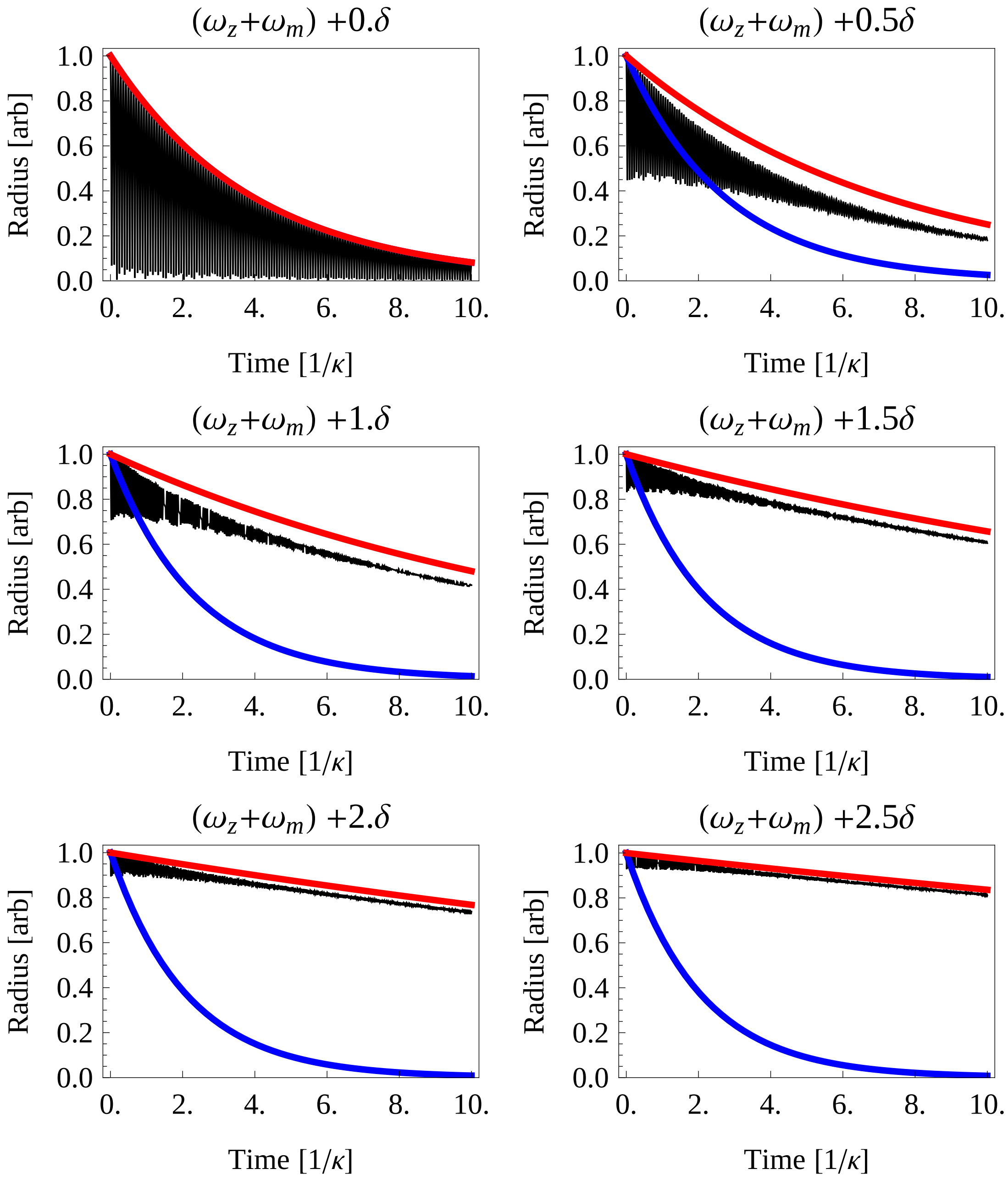

Figure 4.5: The time evolution of the radial distance of a particle from the axis of a Penning trap with a superimposed rotating dipole electric field (black). Also included is a plot of $\exp(\lambda_1 t)$ (blue) and $\exp(\lambda_2 t)$ (red) as labelled in figure 4.4.

taken using the rotating wall installed in the accumulator.

4.2 Experimental Results

The only published results of rotating wall compression observed in the single particle regieme are by Greaves and Moxom [24]. These investigators used a central density to characterise the compression observed during the application of an assymetric rotating quadrupole electric field over a positron cloud. Although they did not provide a definition of their central density it will clearly be a function of not only the cloud width but also the total number of positrons. The results presented here refer only to the cloud width, and are therefore not directly comparable with those of Greaves and Moxom. However the mechanism responsible for compression is expected to be the same in both experiments.

4.2.1 Methodology

The compression rates are measured using the following method. Initially a cloud containing around 10^4 positrons is accumulated over 100 ms using the potentials given in table 4.2 and a magnetic field of 50 mT. A buffer gas pressure of 2×10^{-5} mbar and cooling gas pressure of 2×10^{-5} mbar have been found to be the most effective for the compression experiments. The accumulated clouds initially have a radius of 3 mm[†] and a length of 5 mm (approximated from the potential and measured temperature). Such a cloud at room temperature (300 K) would have a Debye length, as given by equation 1.1, of 5 mm and is therefore not considered a plasma.

Accumulation is stopped and the rotating wall electric field is applied for a certain time, t, with a frequency f_{RW} and peak-to-peak amplitude V_{pp}. Subsequently, the cloud is ejected from the trap and the width, σ, of the cloud is determined using the method described in section 2.4.2. The cloud width, $\sigma(t)$, was found to decrease smoothly from its initial value with no rotating wall to a

---

[†] From figure 4.6 the half width at half maximum is $8\times\sqrt{2*\ln(2)}$ mm however this is the radius as measured in a magnetic field which is a factor of 10 lower than that in the accumulator and must therefore be divided by $\sqrt{10}$.

Table 4.2: The potentials applied to the accumulator electrodes indicated in figure 2.5 during accumulation, compression and expulsion, and chosen to maximise the positron yield.

	E0	Grad High	Grad Low	E1	E2	E3	E4	E5
Accumulation	45	44	38	35	34	33	28	140
Compression	100	44	38	35	34	33	28	140
Expulsion	100	44	38	35	34	33	28	0

constant value, implying that the particles could not be fully axialised (for an example see figure 4.6). The reason for this is as yet not fully understood but may be due to space-charge repulsion, asymmetries in the magnetic or electric field, or possibly scattering on the background gas. A plausible way in which this may be modeled is by the inclusion of a constant expansion term, γ, in addition to the compression rate, Γ, given by equation 4.25. The resulting evolution can then be described by the differential equation:

$$\dot{\sigma} = -\Gamma\sigma + \gamma, \tag{4.26}$$

which has the solution

$$\sigma(t) = \left(\sigma_0 - \frac{\gamma}{\Gamma}\right) \exp\left(-\Gamma t\right) + \frac{\gamma}{\Gamma}, \tag{4.27}$$

where σ_0 is the initial cloud radius. A fit of the form given in equation 4.27 is shown in figure 4.6.

The measurements, as described above, are repeated across a rotating wall frequency range centred around the axial bounce frequency. In figure 4.7 a typical result for $\Gamma(f_{RW})$ is shown up until till a certain frequency difference with respect to f_0. The compression curves can be fitted using equation 4.25 resulting in values for the damping factor, κ, central frequency, f_0, and frequency response width, δ.

At frequencies which result in no compression an attempt to fit $\sigma(t)$ often results in a false compression rate with a very large uncertainty associated with it, an example of which may be seen in figure 4.8. On occasion the errors associated with these false compression rates is artificially small and so has a large effect on weighted fitting algorithms. To overcome this problem two criteria are invoked

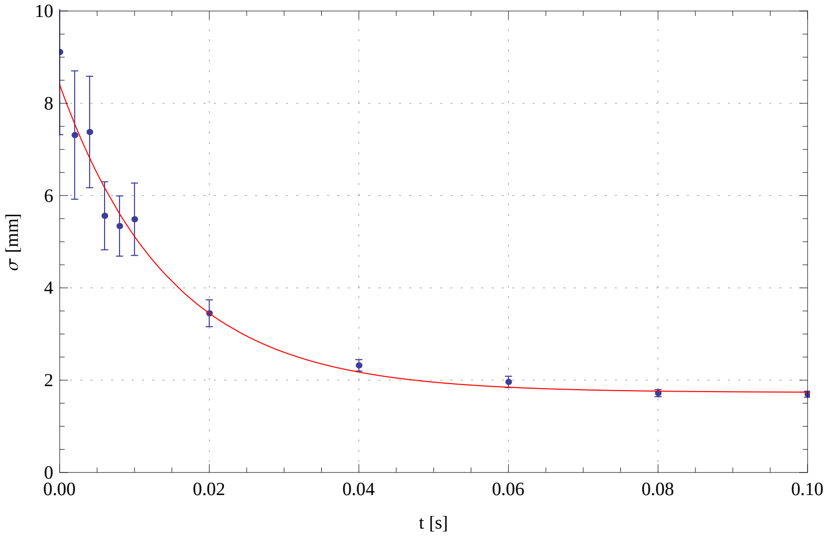

Figure 4.6: A typical compression curve showing the time evolution of the cloud width, $\sigma(\mathrm{t})$. The solid line is a fit using equation 4.27 giving $\Gamma = 67.9 \pm 6.2\ \mathrm{s}^{-1}$ and $\gamma = 118 \pm 19\ \mathrm{mm\ s}^{-1}$. The rotating wall was at a frequency 9.54 MHz and with a peak-to-peak amplitude of 0.5 V.

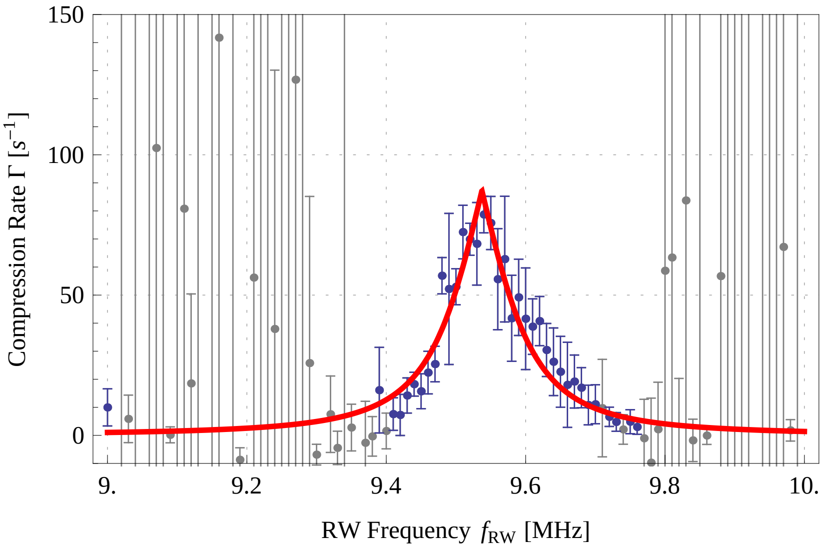

Figure 4.7: An example of a frequency response curve taken with a rotating wall peak-to-peak amplitude of 0.5 V. The solid line is a fit of the form given by equation 4.25 giving $\kappa = 349 \pm 17\ \mathrm{s}^{-1}$, $\delta = 83.4 \pm 6.1$ kHz and $f_0 = 9.5373 \pm 0.0027$ MHz;

for the data to be included in the fitting. Firstly, the fitted compression rate must be larger than the smallest resolvable compression rate[‡]. Secondly the error associated with the compression rate must be smaller than the compression rate. Although the second criterion is not strictly necessary it has been found to reduce the standard errors from the frequency response fit. In figure 4.7 the data-points which do not meet these criteria are shown in grey and are not used in fitting.

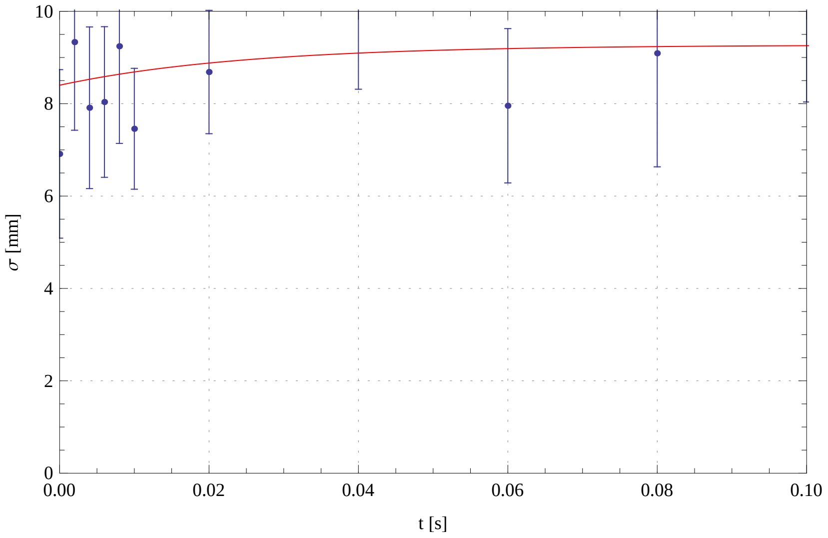

Figure 4.8: An example of a compression curve showing no variation of the cloud width, σ, as a function of compression time. The solid line is a fit using equation 4.27 giving $\Gamma = 40.0 \pm 88.6$ s^{-1} and $\gamma = 371 \pm 808$ mm s^{-1}. This demonstrates the problem with attempting to fit such a compression curve using an exponential. The rotating wall was at a frequency of 9.04 MHz and had a peak-to-peak amplitude of 0.5 V.

4.2.2 Amplitude Dependence

The behaviour of δ, κ and $\omega_0 = 2\pi f_0$ for varying rotating wall peak-to-peak amplitudes has been investigated. It has been reported previously [26] that at high rotating wall amplitudes the positrons may be lost from the trap; presumably due to heating of the cloud. The rotating wall amplitudes here have been kept

---

[‡] This is taken as the reciprocal of half of the smallest time for which the rotating wall was applied during a measurement ($\Gamma \leq 1000$ s^{-1}).

below 1 V peak-to-peak in an attempt to minimise this potential problem. It may also be envisaged that at high amplitudes the positrons may gain enough energy to travel up the potential well into regions which deviate significantly from a harmonic form.

Figure 4.9 shows the fitted frequency response widths from a series of measurements with varying rotating wall peak-to-peak amplitudes. The direct proportionality of the frequency response width and rotating wall amplitude is supported in the data. This linear behaviour is in agreement with the prediction given by equation 4.24b. For a quantitative comparison with theory the fitted gradient of 203±10 kHz V^{-1} must be corrected for the attenuation introduced by the phase splitters, detailed in section 2.2, and for the peak-to-peak amplitude, and so the corrected gradient is 63±4 kHz V^{-1}.

Figure 4.10 shows the electrodes which form the second stage of the accumulator along with the on-axis potential used for these studies. In an attempt to calculate a theoretical value for the gradient of the linear fit shown in figure 4.9, an expansion of equation 3.60 up to the linear term about a point $z = z_c$ may be used:

$$\begin{aligned} u(z = z_c, r \ll r_0, \theta) &= V_r \frac{2\sqrt{2}}{\pi L} \Bigg(\Big(\sum_{m=0}^{\infty} \frac{\sin(k_m z_0)\cos(k_m z_c)}{I_1(k_m r_0)} \Big) \\ &\quad - \Big(\sum_{m=0}^{\infty} \frac{k_m \sin(k_m z_0)\sin(k_m z_c)}{I_1(k_m r_0)} \Big) (z - z_c) \\ &\quad + \mathrm{O}(z - z_c)^2 \Bigg) r \cos(\omega_r t + \theta), \end{aligned} \tag{4.28}$$

The base of the potential well is located 3 mm from the centre of the rotating wall electrode, thus $z_c = 3$ mm. The electrodes used $r_0 = 20.5$ mm, $z_0 = 12.5$ mm and $L = 8z_0$ (as suggested by [57]), result in a coefficient of the linear term of 589 s^{-2}. Using the system parameters ($f_z = 9.59$ MHz, $B = 50$ mT) with this linear term coefficient gives a predicted gradient of 23 kHz V^{-1}. This is not really an accurate estimate of the gradient given that the cloud is estimated to be 5 mm in length. Using $z_c = 5.5$ mm gives a linear term coefficient of 1053 s^{-2} and hence a predicted gradient of 40 kHz V^{-1}. Given the crude nature of these approximations to this experiment these estimates are within reasonable agreement to the fitted (63±4) kHz V^{-1}. A plot of the linear coefficient as a function of z_c shows the coefficient increasing almost linearly until the edge of the rotating wall electrode (see figure 4.11) This calculation offers others wishing to use an asymmetric rotating dipole field a chance to estimate, at least to an order of magnitude, the frequency range, δ, over which their rotating wall will show compression.

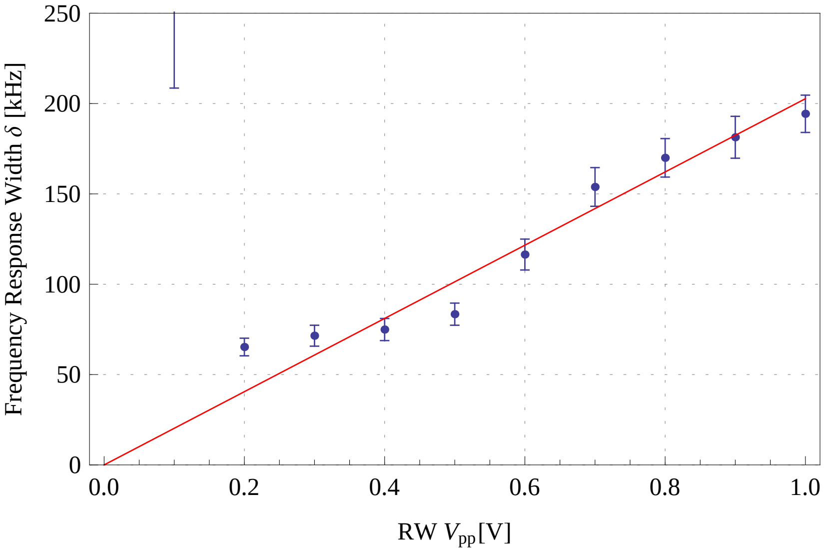

Figure 4.9: The frequency response width, δ, as a function of the applied rotating wall amplitude. The linear fit (red) has a gradient of 203±10 kHz V^{-1}.

Figure 4.12 shows that the rotating wall frequency corresponding to maximum compression rate, f_0, is independent of the rotating wall amplitude (within error) as predicted by equation 4.25. The actual f_0 value of 9.5351±0.0015 MHz is a little off a value calculated from the on axis potential and the applied magnetic field of 9.62 MHz. This 0.1% deviation is most likely due to inaccuracies in the voltages applied to the electrodes as the amplifiers are not calibrated to a sufficient accuracy.

It might be expected that the viscous drag co-efficient, κ, be related to the inelastic scattering cross section and pressure of the cooling gas used. The data presented in figure 4.13 shows that the viscous drag coefficient has a strong dependence on the rotating wall amplitude. Reference [59] compares the energy

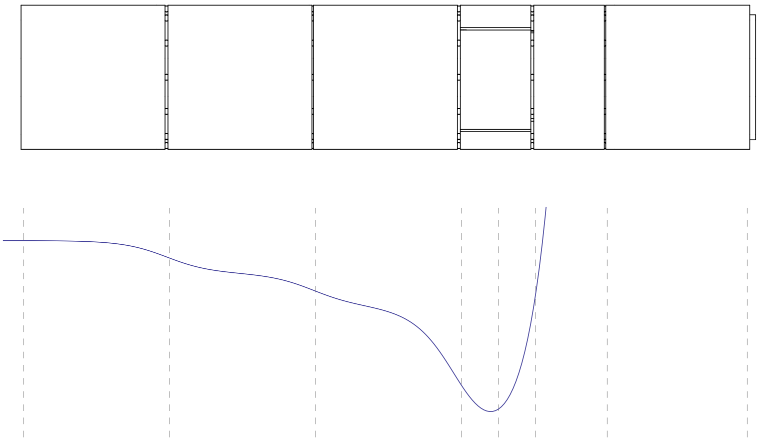

Figure 4.10: The second stage of the positron accumulator. Top: Electrodes. Bottom: the axial potential during compression.

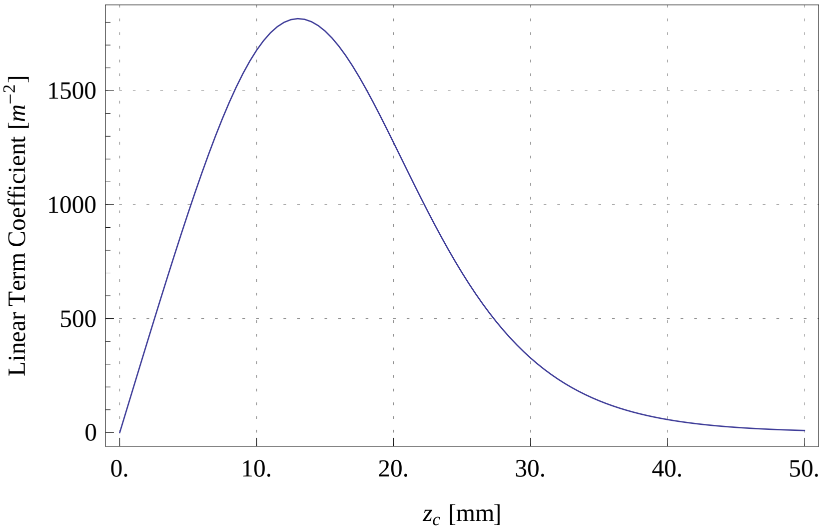

Figure 4.11: The variation of the linear coefficient as given in equation 4.28 as a function of the offset position, z_c. ($r_0 = 20.5$ mm, $z_0 = 12.5$ mm and $L = 8z_0$)

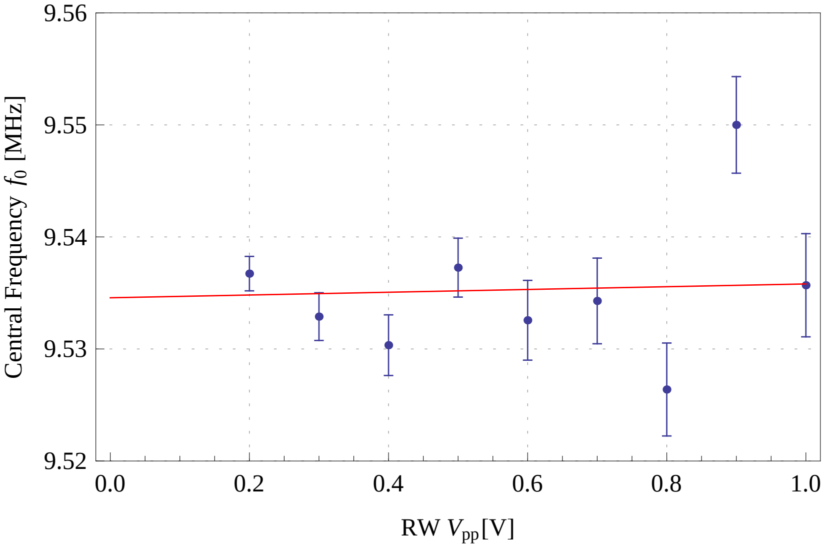

Figure 4.12: The central frequency, f_0, as a function of the applied rotating wall amplitude.

dependence of the inelastic scattering cross sections of both electron and positron impact with carbontetrafluoride (CF_4), which is also often used as a cooling gas in positron accumulators. The high electronegativity of fluorine (3.98[§]) compared with that of carbon (2.55) means that the bond has a strong dipole moment. As discussed in [60] the ν_3 inelastic scattering cross section for both positrons and electrons is similar, most likely due to the large charge transfer between the carbon and fluorine atoms. To date no experimental data measuring the inelastic scattering cross section of low energy positrons on SF_6 has been published. The same arguments as presented in [60], however, may be extended to the S-F Bond as sulphur also has a low electronegativity (2.58) comparable to that of carbon. Figure 4.14 shows a comparison of the Born-dipole approximation with that of experimental results for low energy electrons scattering on SF_6. It is qualitatively similar to the variation of the viscous drag coefficient with rotating wall amplitude, a result which may be indicative of the shortcomings of the viscous drag model. In reality the positrons will experience an acceleration in the time between collisions due to the electric field and will therefore tend to a finite mean energy.

[§] As measured on the Pauling electronegativity scale

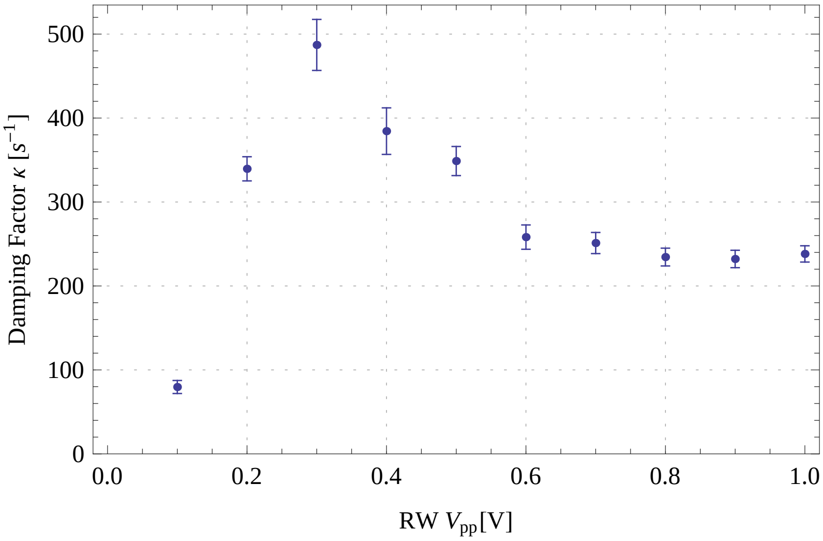

Figure 4.13: The damping coefficient, κ, as a function of the applied rotating wall amplitude.

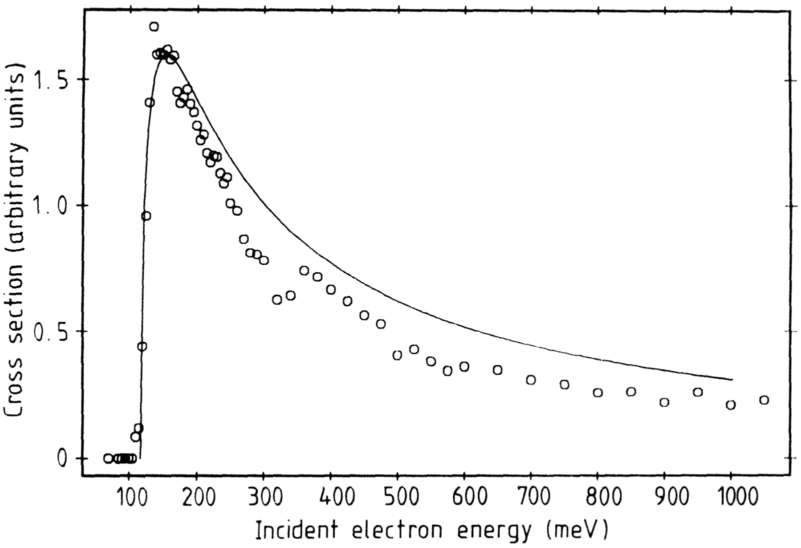

Figure 4.14: A comparison of the prediction of the Born direct point-dipole mechanism for ν_3 excitation with experimental data for low-energy electron scattering by SF_6. The maximum in the calculated cross section has been scaled roughly to the maximum of the experimental data [58].

4.2.3 Well Shape Dependence

By varying the potential applied to electrode 4 (E4 in figure 2.5) it is possible to modify the well shape and hence the bounce frequency of the trapped particles. The trap potential can be calculated either using an analysis similar to that presented in section 3.3 or by using a finite difference approach to solve Laplace's equation as is done by many pieces of proprietary software. Using Simion® the on-axis potential was calculated for varying values of potential applied to E4 and, by producing a quadratic fit about the potential minimum, it was possible to calculate the bounce frequency a particle in the trap would exhibit.

It was later realised that changing the potential applied to E4 not only modified the well shape but also the position of the potential minimum. This would modify the effective amplitude of the rotating dipole as given by the linear expansion in equation 4.28. The quadratic fits to the simulated on-axis potential allowed an estimate of the offset of the trap minimum relative to the centre of the rotating wall electrode, z_c, to be made. The offset positions, z_c, linear coefficients, a_z, and predicted bounce frequencies, f_z, as the voltage on E4 is varied are tabulated in table 4.3.

Table 4.3: Calculated offsets of well base to the centre of the rotating wall electrode, z_c, the resultant linear coefficients given by equation 4.28, a_z and the predicted axial bounce frequencies, f_z, as the voltage applied to E4 is varied.

E4 Potential [V]	z_c [mm]	a_z [s^{-1}]	f_z MHz
27.0	2.1	414	10.26
27.5	2.5	492	9.92
28.0	3.0	589	9.59
28.5	3.5	685	9.20
29.0	4.1	799	8.79
29.5	4.8	928	8.32
30.0	5.7	1088	7.79
30.5	6.7	1255	7.18
31.0	8.0	1449	6.43
31.5	9.7	1649	5.49

The frequency scans produced may be seen in appendix C. In addition to the movement of the potential minimum, the shallower wells allow particles to travel further into the anharmonic region of the potential, causing an increased broadening of the frequency response width as well as producing an asymmetric shape. This effect is most noticeable in the latter graphs given in appendix C.

By assuming a magnetic field of 50 mT and that the maximum compression rate is obtained when $f_0 = f_z + f_m$ it is possible to determine the bounce frequency of the particle from the fitted values of f_0. This has been done in producing figure 4.15 and is compared with the value calculated by using a quadratic fit to the on axis potential. The deviation between the calculated and measured frequencies may be accounted for by the poor calibration of the amplifiers used to apply the potentials on the accumulator electrodes.

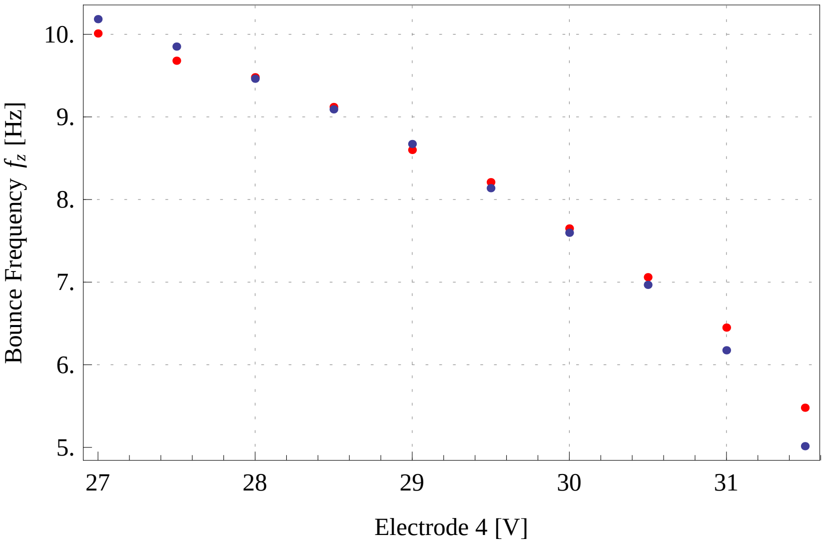

Figure 4.15: The variation of bounce frequency, f_z, as the potential applied to E4 is varied: calculated (red) and determined from the fits to the frequency scans (blue).

Figure 4.16 shows the variation of the fitted compression widths with the bounce frequency; both determined from the fits shown in appendix C. It was only possible to vary the bounce frequency over half a decade while still maintaining an acceptable signal, and so it is difficult to prove the power law dependence predicted by equation 4.24b. In an attempt to demonstrate the $\omega_z^{-\frac{1}{2}}$ dependence given in equation 4.24b, the data was plotted on a log-log scale and a linear fit produced.

The linear fit gave a gradient, and hence power law dependence, of -1.80±0.23. The difference between this value and the expected -0.5 may be accounted for, as alluded to earlier, by the variation of the position of the potential minimum of the trap. In an attempt to compensate for this effect the same data are plotted in figure 4.18 with the ordinate values divided by the linear coefficients given in table 4.3. When plotted on a log-log scale, this compensated data gives a power law dependence of -0.33±0.27, however as may be seen from figure 4.19 this does not represent a satisfactory fit. This does however illustrate that the power law dependence of this dataset is dominated by the shifting of the potential minimum.

In summary, the experiments described in this chapter support the theoretical formalism which has been developed. The frequency response shapes are cusps which are described the form given in equation 4.25. The linear dependence of the frequency response width with rotating wall amplitude predicted by the model is supported by experimental results. It is evident from the variation of the fitted damping parameter with rotating wall amplitude that the simple Stokes' viscous drag model is failing to capture some of the physics of this system. The shortcomings of the Swansea positron accumulator to approximate the theoretical model set-up is apparent in the measurements taken in which the potential on an electrode (E4) has been varied in order to modify the trapping potential. Modifications to the accumulator are suggested in the concluding chapter which may overcome these problems.

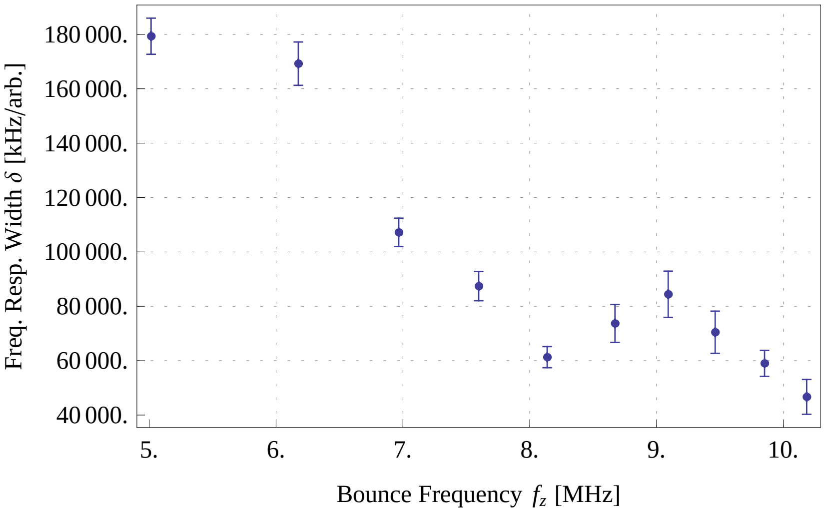

Figure 4.16: The frequency response width, δ, as a function of the measured bounce frequency, f_z.

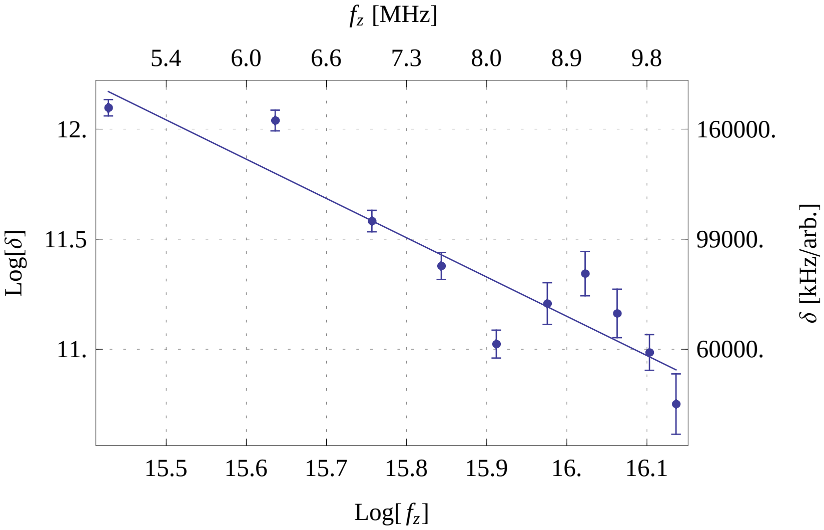

Figure 4.17: The frequency response width, δ, as a function of the measured bounce frequency, f_z, presented on a logarithmic scale. The linear fit gives a gradient of -1.80±0.23 on the logarithmic scale.

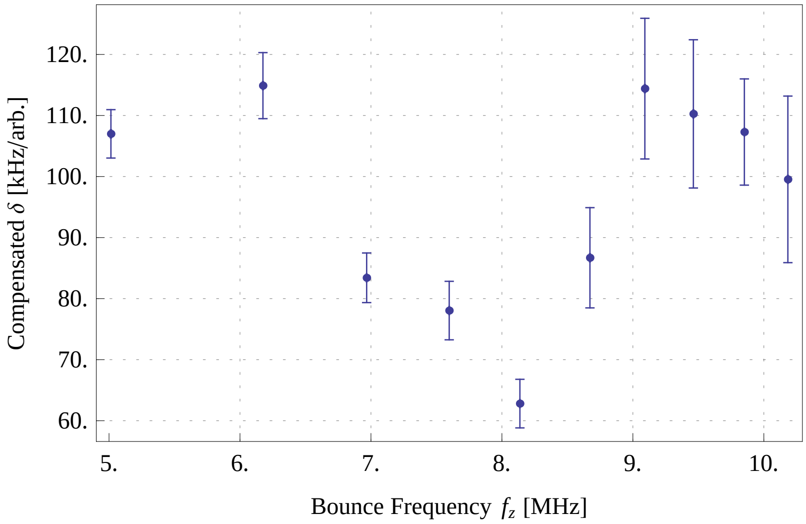

Figure 4.18: The frequency response width, δ, divided by the linear coefficients, a_z (given in table 4.3) as a function of the measured bounce frequency, f_z.

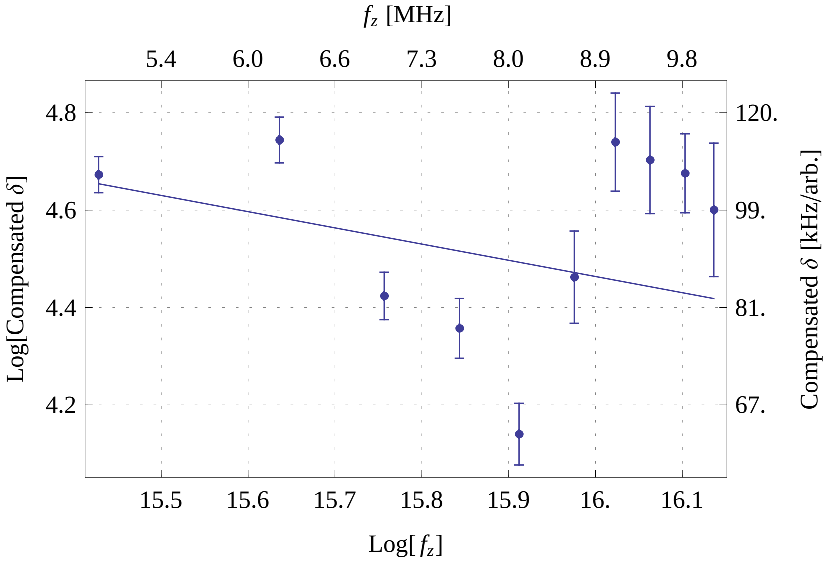

Figure 4.19: The frequency response width, δ, divided by the linear coefficients, a_z (given in table 4.3) as a function of the measured bounce frequency, f_z, on a logarithmic scale. The linear fit gives a gradient -0.33±0.27 on the logarithmic scale.

Chapter 5

Accumulation Experiments

“Nid da lle gellid gwell - *(It is) not good where it could be better*”

— *John Llewellyn Jones (c. 2000)*

The improved accumulation yield caused by the application of the rotating wall electric field has been presented elsewhere [26, 27]. These measurements, which involve the application of the rotating wall during the accumulation stage, are extremely interesting from an applications point of view, but are quite difficult to interpret. Unlike the results presented in the previous chapter, positrons were continually added to the trap and thus the results are a convolution of the rotating wall and accumulation effects.

5.1 Improvements in Accumulated Yield

5.1.1 Cooling Gas Pressure Effects

Accumulation curves were taken for varying pressures of the buffer, N_2, and cooling, SF_6, gases both with and without the rotating wall electric field applied during accumulation. An analysis as detailed in section 3.2 was performed on the accumulation data to obtain values for the trap storage parameter, n_∞, loss rate, λ, and accumulation rate, R.

5.1.1.1 Accumulation without Rotating Wall

As shown in section 3.2 molecular nitrogen is an excellent buffer gas, however, it is a poor cooling gas. Conversely sulphurhexafloride is an excellent cooling gas, but a poor buffer gas (see table 3.2). The results of this experiment, as presented in figure 5.1 (top), shows that increasing the SF_6 pressure does not significantly modify the capture efficiency, and hence the accumulation rate remains unchanged within experimental uncertainty.

To a first order approximation the loss rate of the trap with the additional gas is predicted to behave as

$$\lambda = CP_{N_2} + DP_{SF_6} \tag{5.1}$$

Where C and D are related to the Z_{eff} (the effective number of electrons, see section 5.1.2) and transverse diffusion coefficient of the positron in the N_2 and SF_6 respectively. Figure 5.1 (middle) shows a plot of the loss rate as the buffer and cooling gas pressures are varied. The lifetime of the trap is diminished by an increased cooling gas pressure due to increased annihilation and radial transport.

5.1.1.2 Accumulation with Rotating Wall

The same experiments as presented in the previous section were performed, but now with a rotating wall electric field applied with an amplitude of 2 V at a frequency of 9.75 MHz. These rotating wall settings had been found previously to have a significant effect on accumulation.

It would be expected that the rotating wall electric field would have little or no effect on the accumulation rate of the trap. Experimental results support this as shown in figure 5.2 (Top). There is a slight deviation of the results corresponding to an SF_6 pressure of 1×10^{-6} mbar which may be due to the moderator efficiency as these measurements were taken over two days. The moderator efficiency was not monitored at this time.

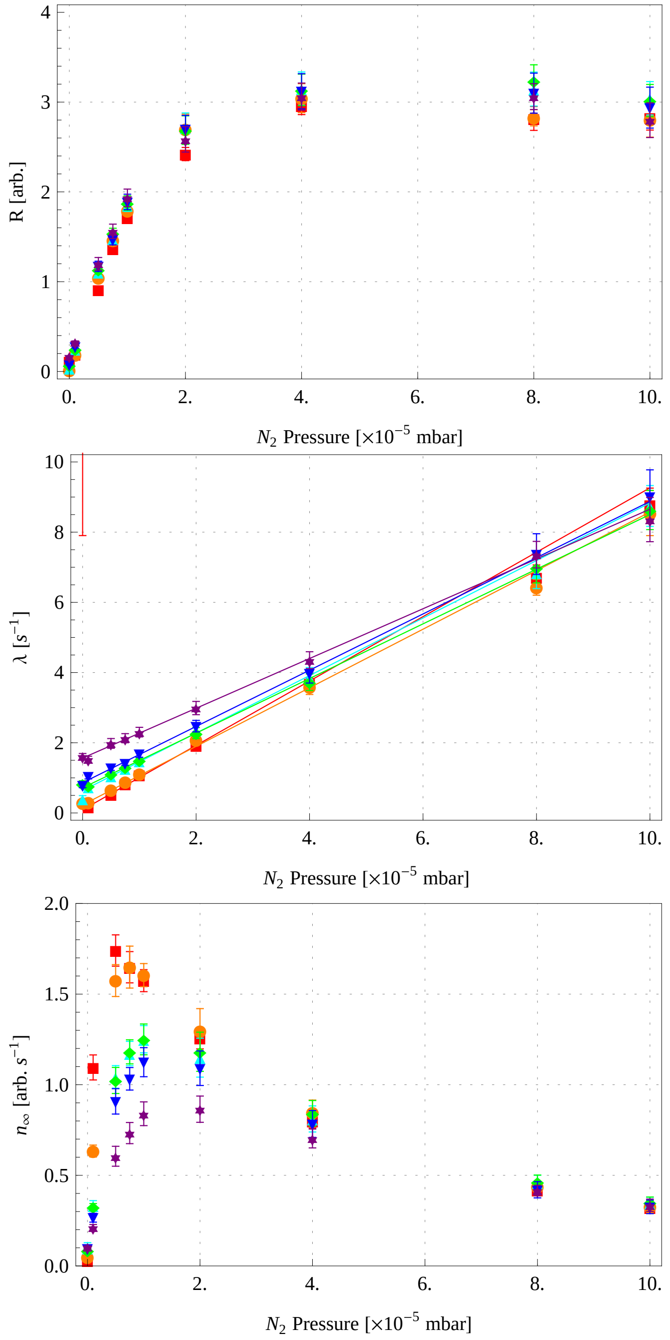

Figure 5.1: The accumulation rate R (top), loss rate λ (middle) and saturation level n_∞ (bottom) as a function of buffer and cooling gas pressure without the application of the rotating wall. (P_{SF_6}: ■ 0 mbar; ● 1.0×10^{-6} mbar; ▲ 5.0×10^{-6} mbar; ◆ 7.5×10^{-6} mbar; ▼ 1.0×10^{-5} mbar; ★ 2.0×10^{-5} mbar .) The solid lines (middle) are linear fits of the form given in equation 5.1.

The loss rate of the trap still appears to have a linear behaviour at low cooling gas pressures, as can be seen in figure 5.2 (middle), however this linear dependence seems to be lost at the higher pressures. The reason for the deviation is as yet undetermined. The red dashed line in figure 5.2 (middle) is the linear fit to the trap loss rate for no SF_6 from figure 5.1 (middle). When no SF_6 is present the loss rate with the rotating electric field applied is increased, presumably due to heating, however is it drastically decreased when there is sufficient cooling gas.

Care must be taken when comparing the n_∞ values shown in Figures 5.1 (bottom) and 5.2 (bottom) as the accumulation rate, R, varied by a factor of around $1/3$ between the with and without rotating wall measurements. Despite this it may be concluded from the plots that, in this instance, using the rotating wall technique has increased the potential positron storage, n_∞, by more than a factor of 4.

5.1.2 Frequency Scans with Varying Rotating Wall Amplitude

The rotating wall was applied at frequency f_{RW} and amplitude V during accumulation using the potentials given in table 4.2 with buffer, N_2, and cooling, SF_6, gas pressures of 2×10^{-5} mbar; identical to the parameters used for the work presented in the previous chapter. After a time t the number of accumulated particles was determined by ejecting the positron cloud and measuring the resultant annihilation gammas using a CsI detector. A graph of $n(t)$ was fitted with the function given in equation 3.34 giving the accumulation rate, saturation number and loss rate. The results of these measurments as a function of the rotating wall frequency for a number of different amplitudes are shown in figure 5.3.

As expected figure 5.3 (top) shows that the accumulation rate is unaffected by the rotating wall as observed in the previous subsection. A satisfactory fit to the loss rate as a function of rotating wall frequency is given by

$$\lambda(f) = \Lambda \exp\left(-\Gamma(f)\tau_0\right) + \lambda_0 \tag{5.2}$$

where $\Gamma(f)$ is the function given by the compression theory in the previous chap-

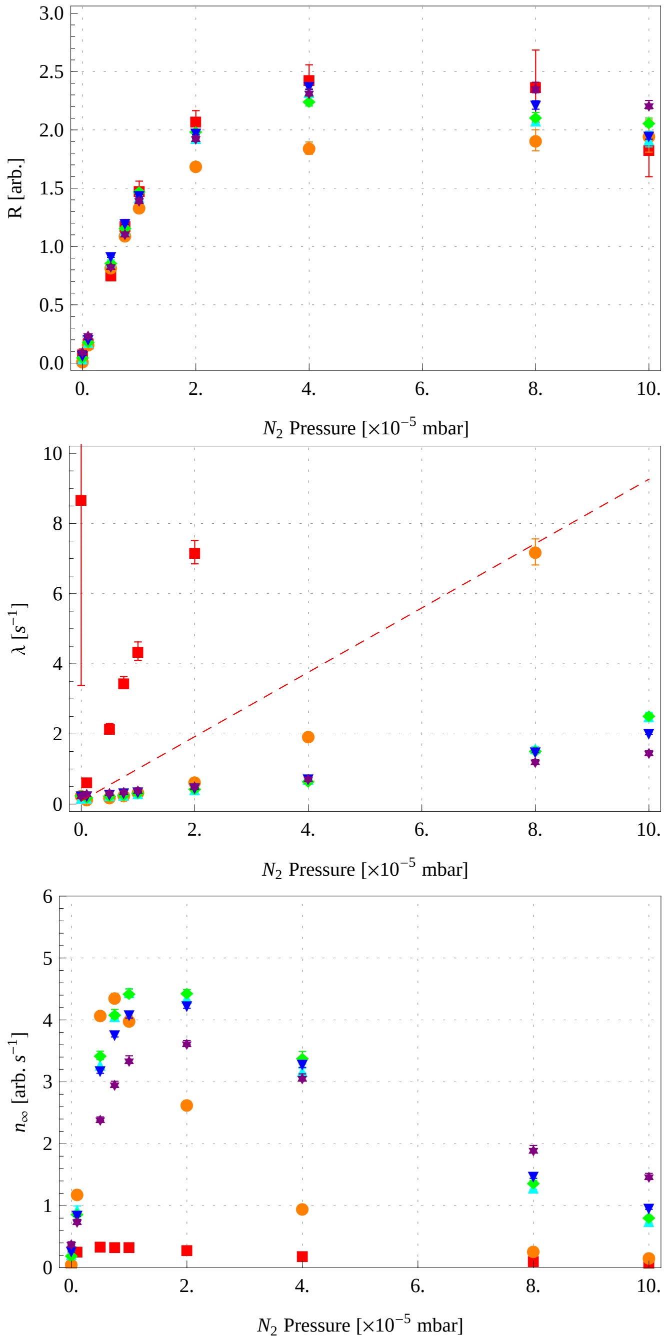

Figure 5.2: The accumulation rate R (top), loss rate λ (middle) and saturation level n_∞ (bottom) as a function of buffer and cooling gas pressure with the rotating wall applied during accumulation with an amplitude of 2 V and frequency of 9.75 MHz. (P_{SF_6}: 🟥 0 mbar; ● 1.0×10^{-6} mbar; ▲ 5.0×10^{-6} mbar; ◆ 7.5×10^{-6} mbar; ▼ 1.0×10^{-5} mbar; ★ 2.0×10^{-5} mbar .) The red dashed line (middle) is the linear fit to the trap loss rate for no SF_6 from figure 5.1 (middle).

ter: equation 4.25. In Figure 5.3 (middle) the data have been fitted with the above function. The values of central frequency and frequency response width were fixed at the values given by the amplitude frequency scans in section 4.2.2.

The combination $\Lambda + \lambda_0$ may be identified with the loss rate without the action of the rotating wall. If the rotating wall is able to counteract all radial loss then λ_0 is identified with the loss rate caused only by annihilation on the background gas. The free positron annihilation rate in the non-relativistic limit is given approximatly by [61]

$$\lambda_a \approx \pi r_0^2 c n_e, \tag{5.3}$$

where r_0 is the classical electron radius and n_e is the electron density in the vicinity of the positron. In a gas of atoms or molecules of number density n, the electron density is Zn where Z is the number of electrons bound to each molecule or atom. Thus if the atom/molecule-positron system were undistorted by the incoming positron the free annihilation rate would be given by

$$\lambda_a = \pi r_0^2 c n Z. \tag{5.4}$$

In reality the positron modifies the charge distribution in a way which typically enhances the electron density in its vicinity. This complicated effect may be approximated by replacing the true number of electrons bound to the atom or molecule, Z, by an effective number Z_{eff}. For a density ρ in Amagat[*] the annihilation rate is given by

$$\lambda_a = 0.201 \rho Z_{eff}, \tag{5.5}$$

where λ_a is in units of μs^{-1}.

Using the value of $\lambda_0 = 0.75$ s^{-1} from figure 5.3 (middle) and the Z_{eff} of SF$_6$ of 97, would suggest a pressure in the second stage of the accumulator of 3.8×10^{-5} mbar. During these measurements the cooling gas pressure was measured as 2.0×10^{-5} mbar using a cold-cathode ion gauge located in the annihilation plate cross. This ion gauge is calibrated with respect to nitrogen pressure and so a correction factor of 2.2 must be taken into account; thus the true SF$_6$ pressure in

---

[*] An Amagat is the number of ideal gas molecules per unit volume at 1 Bar and 273.15 K. This is equal to 2.69×10^{25} m^{-1} or the Loschmidt constant. It may be calculated from $\rho = \frac{P}{1\ Bar} \frac{T}{273.15\ K}$

this cross was around 4.4×10^{-5} mbar. Given that this pressure would be slightly higher than the pressure in the second stage of the accumulator, the accord between the measured and calculated pressures would support the identification of λ_0 with the annihilation limited lifetime. Further investigations are required to determine the origin of the time parameter, τ_0.

5.2 Optimisation for 10 Hz Operation

Given that the Swansea positron accumulator was designed to run optimally at 10 Hz to match the repetition rate of the pulsed lasers, these studies would be incomplete without investigating the optimum rotating wall parameters for 10 Hz operation. A series of measurements have been carried out to investigate the optimum parameters for 10 Hz operation when using the rotating wall during accumulation.

Figure 5.4 shows the effect on the positron signal as the buffer and cooling gas pressures are varied with the rotating wall applied during accumulation at a frequency of 9.75 MHz and amplitude of 2 V. The data for pressures above 5×10^{-6} mbar show that increasing the cooling gas pressure with these particular rotating wall settings has little effect on the accumulated number of particles. This is as expected given that the accumulator is operating at a rate which is far greater than the trap loss rate, λ. The optimum buffer gas pressure is around 4×10^{-5} mbar.

The results of a set of measurements for rotating wall frequency scans with varying amplitudes is shown in figure 5.5. The buffer and cooling gas pressures were both at 2×10^{-5} mbar. The central density was determined by masking the cloud with a circular aperture of radius 2 mm and measuring the transmitted number of positrons. The CsI detector used for these measurements was in an uncalibrated location and so the relative sizes of the total signals and central densities should not be quantitatively compared.

It may be seen that the total signal only increases by a factor of around $1/3$ across a band of frequencies centred around 9.4 MHz. The small increase in signal is again because the trap was operating at a rate which was greater than the loss rate of the trap. A rotating wall of at least 1 V is required for

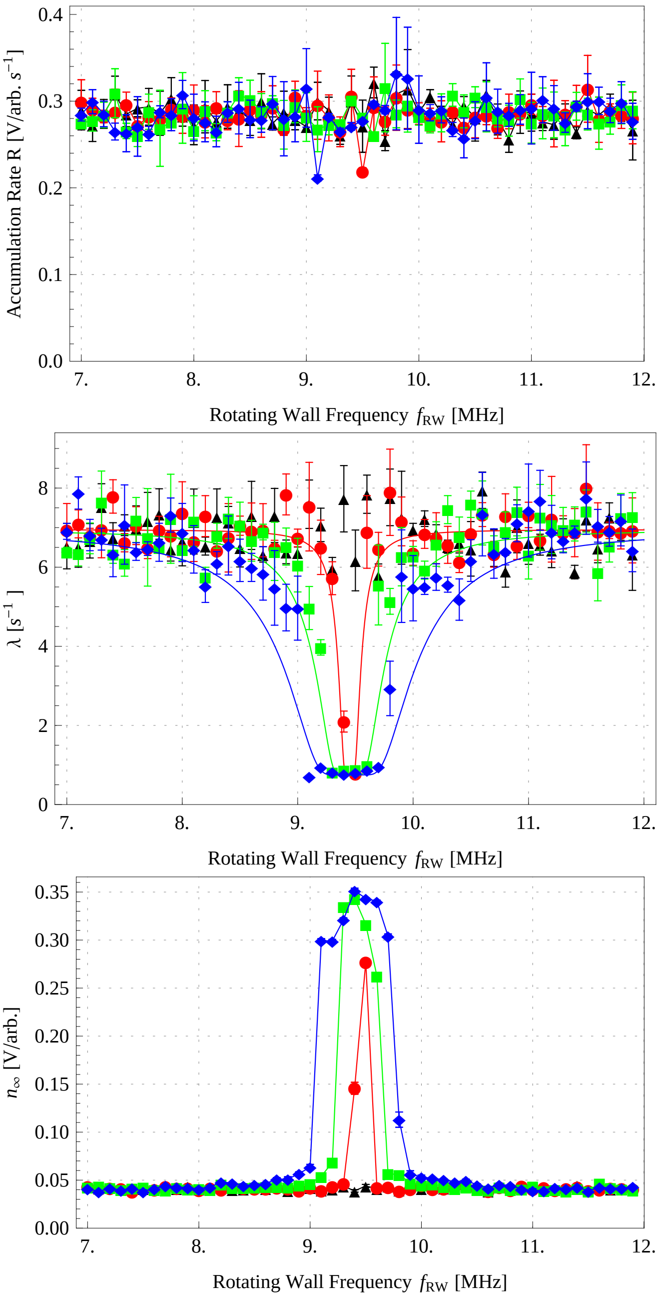

Figure 5.3: The accumulation rate R, trap loss rate λ and saturation level n_∞ for rotating wall frequency scans with varying amplitude applied during accumulation. The lines in the upper and lower images join the points to guide the eye. The lines on the middle image is a fit of the form given in equation 5.2. (Amplitudes: ▲ 0 V; ● 0.1 V; ■ 0.5 V; ◆ 1 V.)

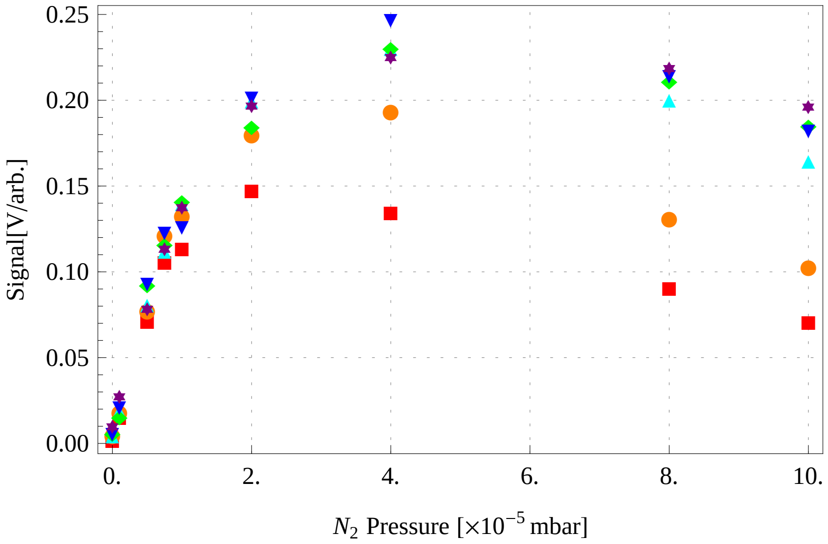

Figure 5.4: The positron signal at 10 Hz operation for varying buffer N_2 and cooling SF_6 gas pressures with the rotating wall applied with an amplitude of 2 V and frequency of 9.75 MHz during accumulation. (P_{SF_6}: ■ 0 mbar; ● 1.0×10^{-6} mbar; ▲ 5.0×10^{-6} mbar; ◆ 7.5×10^{-6} mbar; ▼ 1.0×10^{-5} mbar; ★ 2.0×10^{-5} mbar .)

a significant increase in the central density. The frequency corresponding to the maximum measured central density is close to the frequency corresponding to the maximum compression rate as measured in the previous chapter.

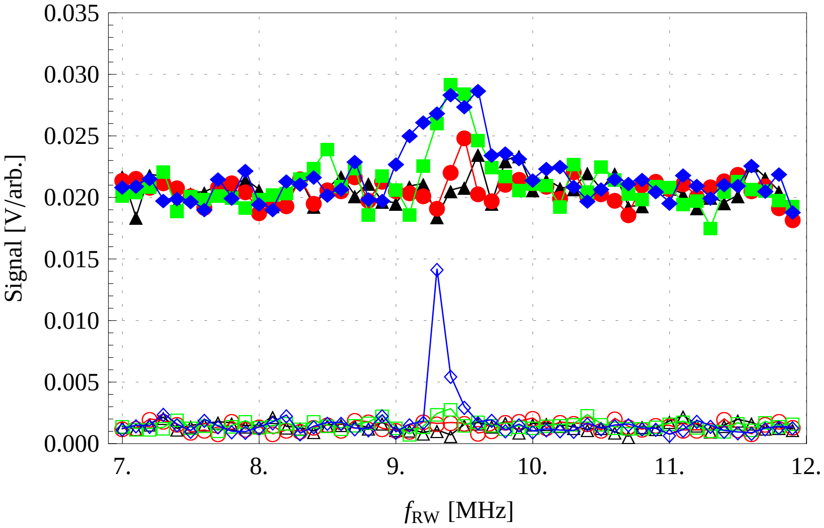

Figure 5.5: The positron signal at 10 Hz operation for rotating wall frequency scans performed at different amplitudes. (Amplitudes: ▲ 0 V; ● 0.1 V; ■ 0.5 V; ◆ 1 V .) Solid: Total signal; Hollow: Central Density. The CsI detector used for measuring the signals for the central density was in an uncalibrated location and so the total and central density signals should not be compared directly.

Chapter 6

Final Remarks

“The oldest, shortest words - ‘yes’ and ‘no’ - are those which require the most thought”

— *Pythagoras*

6.1 Conclusions

A model has been developed which successfully describes the frequency response of the compression rates as measured using the Swansea positron accumulator. The frequency response curves are cusp shaped with the maximum compression rate achieved when the rotating wall frequency is at the sum of the bounce and magnetron frequency of the trapped particle. Unlike Dehmelt’s side-band cooling, expansion is not observed at the so-called lower side-band when the rotating wall frequency is at the bounce frequency minus the magnetron frequency [44]. The accuracy to which the frequencies may be predicted is limited by the calibration of the amplifiers used to apply the potentials onto the accumulator electrodes, as well as the anharmonicities of the trap.

The width of the frequency response curves were found to be proportional to the rotating wall amplitude, in agreement with the theoretical model. By approximating the electric potential produced by a four-segment rotating wall electrode, an equation has been derived which may be used to find a very crude approximation for the constant of proportionality. Attempts to verify the effect of changing the bounce frequency by modifying the potential applied to the E4 electrode of the accumulator (see figure 2.5) failed, as this also moved the location of the base of the potential well. The Stokes' viscous drag model used to approximate the buffer gas cooling fails to capture some of the important physics of positron-molecule collisions. This is evident in the variation of the damping parameter, κ, observed as the rotating wall amplitude is varied. A possible solution to this problem is suggested in the future work section.

The application of the rotating wall electric field during accumulation was seen to have no effect on the accumulation rate, R, however it was shown to be very effective at increasing both the traps positron storage parameter n_∞ and the central density of the accumulated cloud. At frequencies near the optimum compression rate the trap lifetime was equal to the annihilation-limited lifetime on the cooling gas corresponding, in the case of the Swansea positron accumulator, to the potential storage parameter being increased by a factor of 7. It may therefore be concluded that, without the application of the rotating wall, radial transport is the dominant loss mechanism. The quantitative increase in central density is not attainable from the data, however qualitatively the central density of the positron cloud was seen to increase substantially at a frequency which coincided with the optimum compression frequency provided a sufficiently high rotating wall amplitude was applied.

At a 10 Hz repetition rate, the increase in particle number caused by the application of the rotating wall during accumulation was not as dramatic as the increase in potential storage because the accumulation time was less than the particle trap time. Even so, the application of the rotating wall caused a large increase in the central density when it was applied at the appropriate frequency. This increased density will prove useful for the laser-Ps experiments (detailed in section 1.2.1) and will allow easier transport of the cloud through narrow pumping restrictions.

6.2 Future Work and Applications

Prior to further studies it would be advisable that a new electrode structure be constructed which will allow electric potential configurations which will more closely match the theoretical model presented in section 4.1. The electrodes currently used in the Swansea positron accumulator should be redesigned as they are not ideally suited to precision Penning-type trap measurements as it is extremely difficult to produce a deep harmonic potential well. There are currently a number of methods which may be employed to design cylindrical Penning traps such that the harmonic region is maximised, including the use of compensation electrodes [57]. As well as replacing the electrodes used to create the potential well, it would be worthwhile installing two adjacent rotating wall electrodes, offset from each other by 180 degrees as this would enhance the linear term from the expansion and reduce the next significant term. A suggested schematic of the new electrode array is shown in figure 6.1.

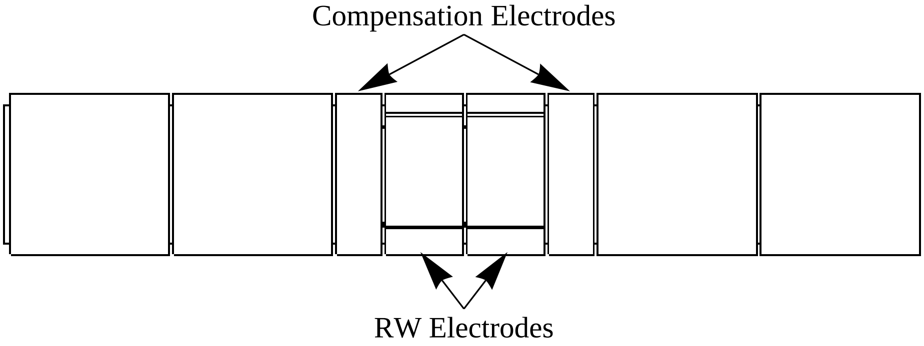

Figure 6.1: A Schematic of the recommended replacement electrode structure to be used for future work. The lengths of the electrodes should be calculated to maximise the harmonic region of the trap.

In addition to the new electrode array, an alternative cooling mechanism should be considered. Cooling methods such as cyclotron cooling and damping via an external circuit [44] are described, in most practical cases, by a term identical to the Stokes' viscous drag expression and will therefore offer a more precise test of the compression model developed in section 4.1. Rapid cyclotron cooling requires a high magnetic field and so the accumulated positrons would need to be transfered into the 5 T magnet currently used for high B-field studies. Cooling by the use of an external circuit should also be investigated. Furthermore, as mentioned in section 1.2.3, the Swansea positron group is interested in using positrons which are cooled via cyclotron radiation in a strong magnetic field to sympathetically cool magnesium ions. A good approximation of the cooling of a heavy ion on a light buffer gas is given by a Stokes' viscous drag term [62]. Using this system may offer an alternative method to test the axialisation model using the magnesium ion cloud rather than the positrons.

If the heating process caused by the application of the rotating wall could be better understood, then the variation of the damping parameter with the rotating wall amplitude (figure 4.13) might offer a method of measuring the low energy inelastic scattering cross sections of positron–molecule collisions. Temperature measurements could be achieved by slowly lowering the potential applied to the exit electrode (E5) and measuring the number of escaping positrons. The accurate determination of the pressure in the second stage will be a limiting factor for any measurements using the accumulator.

The accumulator with the application of the rotating wall offers a system which may be used to perform so-called swarm or drift measurements to determine the mobility of low energy positrons in gases. The potentials applied to the rotating wall may be switched off and the evolution of the cloud monitored by a series of phosphor screen images. The Swansea positron group has, on order, a new CCD camera which if coupled with a micro channel plate (MCP) would be ideally suited to these types of studies.

The characteristic equation governing the eigenvalues of the rotating wall system (equation 4.16) is a quartic equation. An approximation to the solution was found by fitting parameters to a form which closely matches the exact solution, however, it should be a future objective to find this by performing approximations to the roots of the quartic equation given the typical experimental hierarchy,

$$\sqrt{a} >> \omega_c > \Omega >> \omega_z >> \omega_m >> \kappa. \tag{6.1}$$

The measurements taken when the rotating wall was applied during accumulation are convoluted. Although a physically plausible analytic form for the behaviour of the lifetime of the trap when the rotating wall is applied during accumulation has been suggested, it has not been rigorously derived. Further investigations are necessary to verify this analytic form and to deduce its physical origin.

Appendix A

$\mathbf{V}^{\pm}$ Decoupling of the Cyclotron and Magnetron motions

Using the definition of the $\mathbf{V}^{\pm}$ coordinates given in equation 3.13 the magnetron and cyclotron motions of a particle in a penning trap may be decoupled. The derivation of equation 3.14, which shows this, is presented here.

$$\begin{aligned}
\dot{\mathbf{V}}^{\pm} &= \ddot{\boldsymbol{r}} - \omega_{\mp}\hat{\boldsymbol{z}} \times \dot{\boldsymbol{r}} \\
&= \left(\Omega_c - \omega_{\mp}\right)\hat{\boldsymbol{z}} \times \left(\mathbf{V}^{\pm} + \omega_{\mp}\hat{\boldsymbol{z}} \times \boldsymbol{r}\right) + \tfrac{\omega_z^2}{2}\boldsymbol{r} \\
&= \left(\Omega_c - \omega_{\mp}\right)\hat{\boldsymbol{z}} \times \mathbf{V}^{\pm} + \left(\Omega_c - \omega_{\mp}\right)\omega_{\pm}\hat{\boldsymbol{z}} \times \left(\hat{\boldsymbol{z}} \times \boldsymbol{r}\right) + \tfrac{\omega_z^2}{2}\boldsymbol{r} \\
&= \omega_{\pm}\hat{\boldsymbol{z}} \times \mathbf{V}^{\pm} + \omega_{\pm}\omega_{\mp}\left(\left(\cancelto{0}{\hat{\boldsymbol{z}} \cdot \boldsymbol{r}}\right)\hat{\boldsymbol{z}} - \left(\cancelto{1}{\hat{\boldsymbol{z}} \cdot \hat{\boldsymbol{z}}}\right)\boldsymbol{r}\right) + \tfrac{\omega_z^2}{2}\boldsymbol{r} \\
&= \omega_{\pm}\hat{\boldsymbol{z}} \times \mathbf{V}^{\pm} - \omega_{\pm}\omega_{\mp}\boldsymbol{r} + \tfrac{\omega_z^2}{2}\boldsymbol{r} \\
&= \omega_{\pm}\hat{\boldsymbol{z}} \times \mathbf{V}^{\pm} - \tfrac{1}{4}\left(\Omega_c^2 - \left(\Omega_c^2 - 2\omega_z^2\right)\right)\boldsymbol{r} + \tfrac{\omega_z^2}{2}\boldsymbol{r} \\
&= \omega_{\pm}\hat{\boldsymbol{z}} \times \mathbf{V}^{\pm}
\end{aligned}$$

Appendix B

Compression Rates for Varying Amplitude

This appendix presents the frequency scans, along with fits of the form given in equation 4.25, for the data presented in section 4.2.2.

Table B.1: The fitted Parameters of the compression rate frequency scans for different rotating wall peak-to-peak amplitudes

V_{pp} [V]	κ [s^{-1}]	δ [kHz]	f_0 [MHz]
0.1	79.7 ± 7.8	450 ± 240	9.597 ± 0.034
0.2	340 ± 14	65.3 ± 4.9	9.5367 ± 0.0015
0.3	487 ± 30	71.5 ± 5.8	9.5329 ± 0.0021
0.4	384 ± 28	74.9 ± 6.1	9.5303 ± 0.0027
0.5	349 ± 17	83.4 ± 6.1	9.5373 ± 0.0026
0.6	258 ± 14	116.4 ± 8.6	9.5326 ± 0.0036
0.7	251 ± 83	154 ± 11	9.5343 ± 0.0038
0.8	234 ± 11	170 ± 11	9.5264 ± 0.0041
0.9	232 ± 10	181 ± 12	9.5500 ± 0.0043
1.0	179.7 ± 9.5	160 ± 10	9.5472 ± 0.0050

$V_{\mathrm{pp}} = 0.1\mathrm{V}$

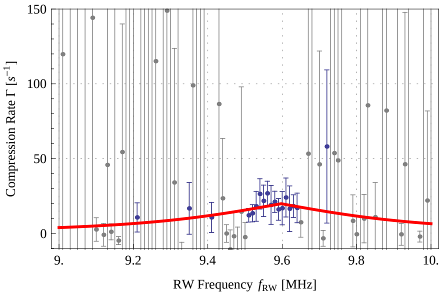

$V_{\mathrm{pp}} = 0.2\mathrm{V}$

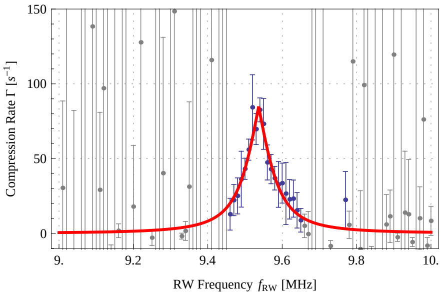

$V_{\mathrm{pp}} = 0.3\mathrm{V}$

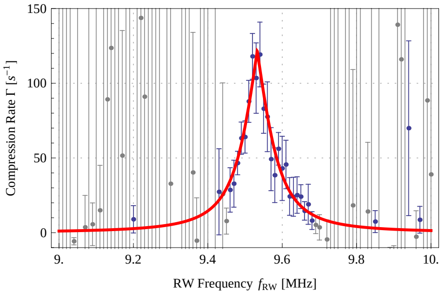

$V_{\mathrm{pp}} = 0.4\mathrm{V}$

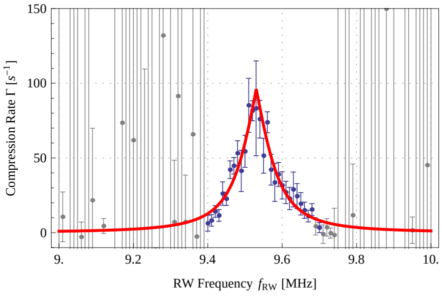

$V_{\mathrm{pp}} = 0.5\mathrm{V}$

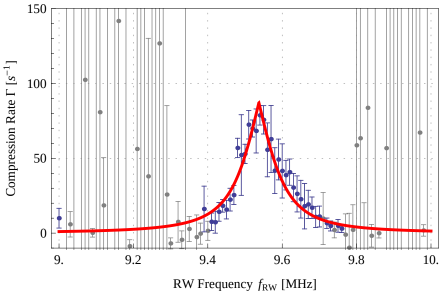

$V_{\mathrm{pp}} = 0.6\mathrm{V}$

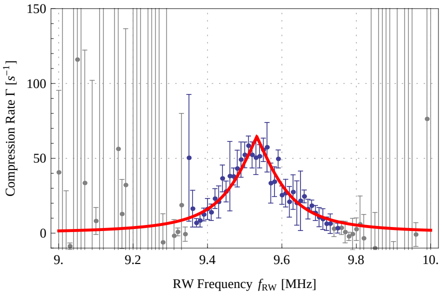

$V_{\mathrm{pp}} = 0.7\mathrm{V}$

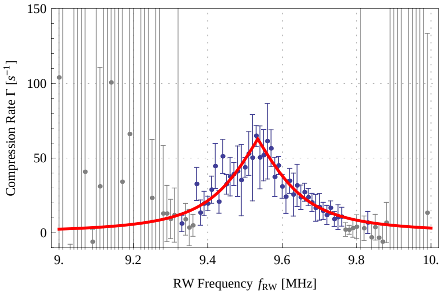

$V_{\mathrm{pp}} = 0.8\mathrm{V}$

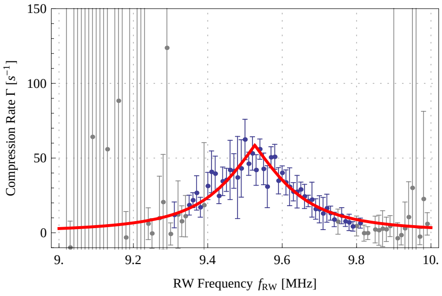

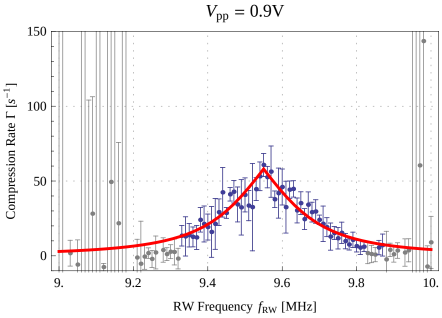
$V_{\text{pp}} = 0.9\text{V}$
Compression Rate Γ $[s^{-1}]$
150
100
50
0
9.
9.2
9.4
9.6
9.8
10.
RW Frequency f_{RW} [MHz]

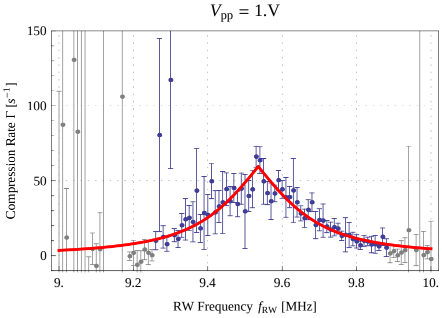
$V_{\text{pp}} = 1.\text{V}$
Compression Rate Γ $[s^{-1}]$
150
100
50
0
9.
9.2
9.4
9.6
9.8
10.
RW Frequency f_{RW} [MHz]

Appendix C

Compression Rates for Varying Well Shape

This appendix contains the frequency scans, along with fits of the form given in equation 4.25, for the data presented in section 4.2.3.

Table C.1: The fitted Parameters of the compression rate frequency scans with a varying potential applied to electrode E4

V_{E4} [V]	κ [s^{-1}]	δ [kHz]	f_0 [MHz]
27.0	757 ± 83	46.7 ± 6.4	10.2205± 0.0030
27.5	842 ± 47	59.0 ± 4.8	9.8860 ± 0.0016
28.0	439 ± 38	70.5 ± 7.8	9.4940 ± 0.0032
28.5	399 ± 37	84.4 ± 8.5	9.1210 ± 0.0035
29.0	826 ± 73	73.7 ± 7.0	8.6990 ± 0.0031
29.5	1590 ± 120	61.3 ± 3.9	8.1610 ± 0.0020
30.0	1571 ± 86	87.4 ± 5.4	7.6182 ± 0.0025
30.5	1727 ± 68	107.2 ± 5.2	6.9845 ± 0.0022
31.0	1363 ± 40	169.2 ± 8.0	6.1889 ± 0.0033
31.5	1091 ± 33	179.3 ± 6.6	5.0235 ± 0.0041

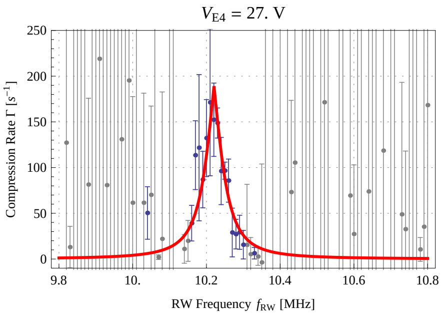
V_{E4} = 27. V
Compression Rate Γ [s^{-1}]
250
200
150
100
50
0
9.8
10.
10.2
10.4
10.6
10.8
RW Frequency f_{RW} [MHz]

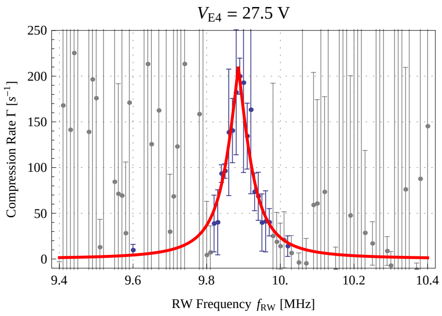
V_{E4} = 27.5 V
Compression Rate Γ [s^{-1}]
250
200
150
100
50
0
9.4
9.6
9.8
10.
10.2
10.4
RW Frequency f_{RW} [MHz]

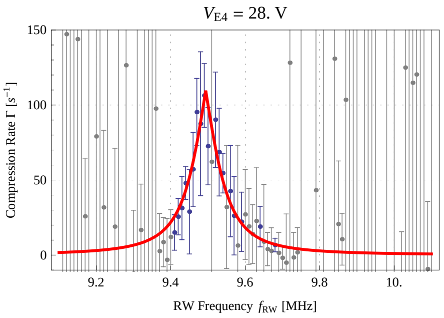
V_{E4} = 28. V
Compression Rate Γ [s^{-1}]
150
100
50
0
9.2
9.4
9.6
9.8
10.
RW Frequency f_{RW} [MHz]

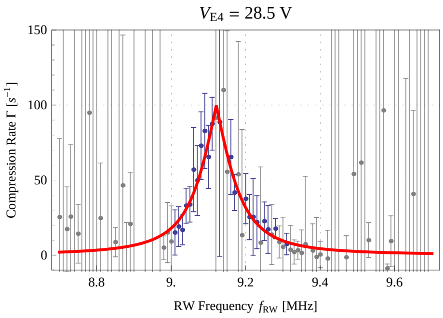
V_{E4} = 28.5 V
Compression Rate Γ [s^{-1}]
150
100
50
0
8.8
9.
9.2
9.4
9.6
RW Frequency f_{RW} [MHz]

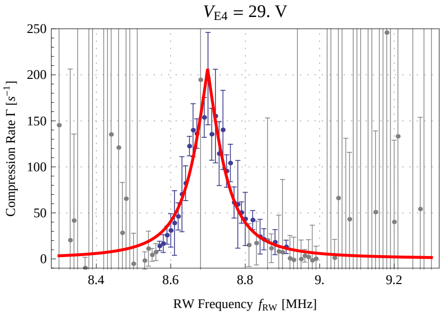
V_{E4} = 29. V
Compression Rate Γ [s^{-1}]
250
200
150
100
50
0
8.4
8.6
8.8
9.
9.2
RW Frequency f_{RW} [MHz]

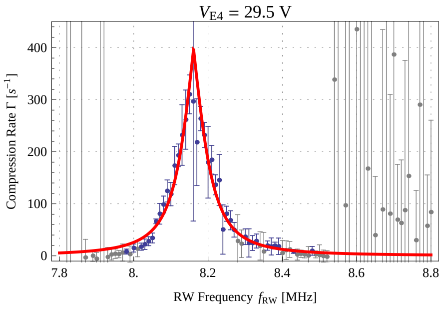
V_{E4} = 29.5 V
Compression Rate Γ [s^{-1}]
400
300
200
100
0
7.8
8.
8.2
8.4
8.6
8.8
RW Frequency f_{RW} [MHz]

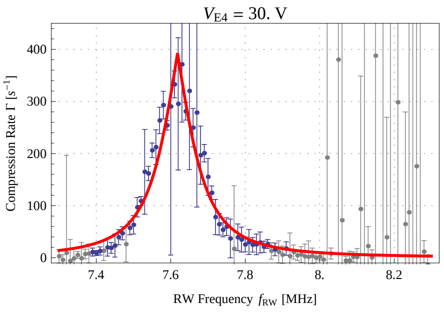
V_{E4} = 30. V
Compression Rate Γ [s^{-1}]
400
300
200
100
0
7.4
7.6
7.8
8.
8.2
RW Frequency f_{RW} [MHz]

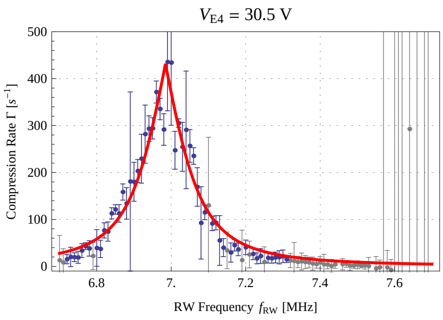
V_{E4} = 30.5 V
Compression Rate Γ [s^{-1}]
500
400
300
200
100
0
6.8
7.
7.2
7.4
7.6
RW Frequency f_{RW} [MHz]

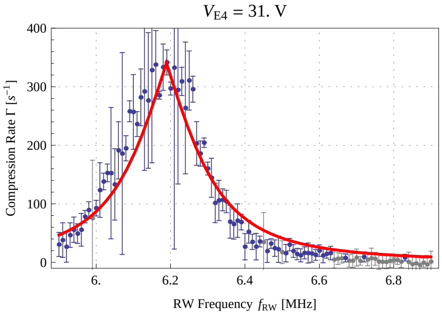
V_{E4} = 31. V
Compression Rate Γ [s^{-1}]
400
300
200
100
0
6.
6.2
6.4
6.6
6.8
RW Frequency f_{RW} [MHz]

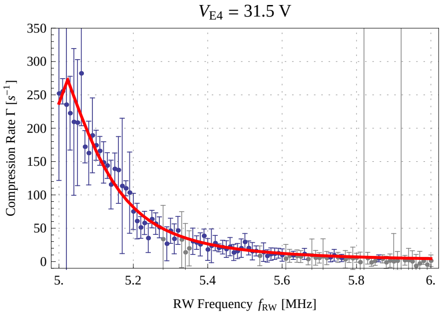
V_{E4} = 31.5 V
Compression Rate Γ [s^{-1}]
350
300
250
200
150
100
50
0
5.
5.2
5.4
5.6
5.8
6.
RW Frequency f_{RW} [MHz]

Bibliography

[1] A. Schuster, “Potential matter–a holiday dream,” *Nature*, vol. 58, p. 367, Aug 1898.

[2] P. Dirac, “Quantised singularities in the electromagnetic field,” *Proc. Roy. Soc. A*, vol. 133, Aug 1931.

[3] C. D. Anderson, “The positive electron,” *Phys. Rev.*, vol. 43, pp. 491–494, Mar 1933.

[4] P. M. S. Blackett and G. P. S. Occhialini, “Some Photographs of the Tracks of Penetrating Radiation,” *Proceedings of the Royal Society of London. Series A*, vol. 139, no. 839, pp. 699–726, 1933.

[5] S. Mohorovićič, “Möglichkeit neuer elemente und ihre bedeutung für die astrophysik,” *Astronomische Nachrichten*, vol. 253, no. 4, pp. 93–108, 1934.

[6] A. E. Ruark, “Positronium,” *Phys. Rev.*, vol. 68, p. 278, Dec 1945.

[7] M. Deutsch, “Evidence for the formation of positronium in gases,” *Phys. Rev.*, vol. 82, pp. 455–456, May 1951.

[8] O. Chamberlain, E. Segrè, C. Wiegand, and T. Ypsilantis, “Observation of antiprotons,” *Phys. Rev.*, vol. 100, pp. 947–950, Nov 1955.

[9] G. Baur, G. Boero, A. Brauksiepe, A. Buzzo, W. Eyrich, R. Geyer, D. Grzonka, J. Hauffe, K. Kilian, M. LoVetere, M. Macri, M. Moosburger, R. Nellen, W. Oelert, S. Passaggio, A. Pozzo, K. Rhrich, K. Sachs, G. Schepers, T. Sefzick, R. S. Simon, R. Stratmann, F. Stinzing, and M. Wolke, “Pro-

duction of antihydrogen," *Physics Letters B*, vol. 368, no. 3, pp. 251 – 258, 1996.

[10] G. Blanford, D. C. Christian, K. Gollwitzer, M. Mandelkern, C. T. Munger, J. Schultz, and G. Zioulas, "Observation of atomic antihydrogen," *Phys. Rev. Lett.*, vol. 80, pp. 3037–3040, Apr 1998.

[11] C. A. Bertulani and G. Baur, "Antihydrogen production and accuracy of the equivalent photon approximation," *Phys. Rev. D*, vol. 58, p. 034005, Jun 1998.

[12] M. Amoretti, C. Amsler, G. Bonomi, A. Bouchta, P. Bowe, C. Carraro, C. L. Cesar, M. Charlton, M. J. T. Collier, M. Doser, V. Filippini, K. S. Fine, A. Fontana, M. C. Fujiwara, R. Funakoshi, P. Genova, J. S. Hangst, R. S. Hayano, M. H. Holzscheiter, L. V. Jørgensen, V. Lagomarsino, R. Landua, D. Lindelof, E. L. Rizzini, M. Macri, N. Madsen, G. Manuzio, M. Marchesotti, P. Montagna, H. Pruys, C. Regenfus, P. Riedler, J. Rochet, A. Rotondi, G. Rouleau, G. Testera, A. Variola, T. L. Watson, and D. P. van der Werf, "Production and detection of cold antihydrogen atoms," *Nature*, vol. 419, pp. 456–459, 2002.

[13] W. Bertsche, A. Boston, P. Bowe, C. Cesar, S. Chapman, M. Charlton, M. Chartier, A. Deutsch, J. Fajans, M. Fujiwara, R. Funakoshi, K. Gomberoff, J. Hangst, R. Hayano, M. Jenkins, L. Jørgensen, P. Ko, N. Madsen, P. Nolan, R. Page, L. Posada, A. Povilus, E. Sarid, D. Silveira, D. van der Werf, Y. Yamazaki, B. Parker, J. Escallier, and A. Ghosh, "A magnetic trap for antihydrogen confinement," *Nuclear Instruments and Methods in Physics Research Section A: Accelerators, Spectrometers, Detectors and Associated Equipment*, vol. 566, no. 2, pp. 746 – 756, 2006.

[14] G. Gabrielse, P. Larochelle, D. Le Sage, B. Levitt, W. S. Kolthammer, R. McConnell, P. Richerme, J. Wrubel, A. Speck, M. C. George, D. Grzonka, W. Oelert, T. Sefzick, Z. Zhang, A. Carew, D. Comeau, E. A. Hessels, C. H. Storry, M. Weel, and J. Walz, "Antihydrogen production within a penning-ioffe trap," *Phys. Rev. Lett.*, vol. 100, p. 113001, Mar 2008.

[15] "Hans G Dehmelt, Autobiography." Nobel Prize Page, 06 2010.

[16] D. Wineland and H. Dehmelt, "Line shifts and widths of axial, cyclotron and g-2 resonances in tailored, stored electron (ion) cloud," *International Journal of Mass Spectrometry and Ion Physics*, vol. 16, no. 3, pp. 338 – 342, 1975.

[17] H. G. Dehmelt, "Entropy reduction by motional sideband excitation," *Nature*, vol. 262, p. 777, 1976.

[18] T. M. O'Neil, "Plasmas with a single sign of charge," *AIP Conference Proceedings*, vol. 175, no. 1, pp. 1–7, 1988.

[19] X.-P. Huang, F. Anderegg, E. M. Hollmann, C. F. Driscoll, and T. M. O'Neil, "Steady-state confinement of non-neutral plasmas by rotating electric fields," *Phys. Rev. Lett.*, vol. 78, pp. 875–878, Feb 1997.

[20] F. Anderegg, E. M. Hollmann, and C. F. Driscoll, "Rotating field confinement of pure electron plasmas using trivelpiece-gould modes," *Phys. Rev. Lett.*, vol. 81, pp. 4875–4878, Nov 1998.

[21] A. W. Trivelpiece and R. W. Gould, "Space charge waves in cylindrical plasma columns," *Journal of Applied Physics*, vol. 30, no. 11, pp. 1784–1793, 1959.

[22] R. G. Greaves and C. M. Surko, "Inward transport and compression of a positron plasma by a rotating electric field," *Phys. Rev. Lett.*, vol. 85, pp. 1883–1886, Aug 2000.

[23] J. R. Danielson and C. M. Surko, "Torque-balanced high-density steady states of single-component plasmas," *Phys. Rev. Lett.*, vol. 94, p. 035001, Jan 2005.

[24] R. G. Greaves and J. M. Moxom, "Compression of trapped positrons in a single particle regime by a rotating electric field," *Physics of Plasmas*, vol. 15, no. 7, p. 072304, 2008.

[25] D. L. Eggleston and T. M. O'Neil, "Theory of asymmetry-induced transport in a non-neutral plasma," *Physics of Plasmas*, vol. 6, no. 7, pp. 2699–2704, 1999.

[26] P. Watkeys, *Towards laser excitation of positronium and advances in positron accumulation techniques.* PhD thesis, Swansea University, 2008.

[27] C. Baker, *Studies of magnetized positronium and of positron dynamics in a rotating dipolar electric field.* PhD thesis, Swansea University, 2010.

[28] M. Charlton, "Antihydrogen production in collisions of antiprotons with excited states of positronium," *Physics Letters A*, vol. 143, no. 3, pp. 143 – 146, 1990.

[29] T. F. Gallagher, "Rydberg atoms," *Reports on Progress in Physics*, vol. 51, no. 2, p. 143, 1988.

[30] B. Griffiths, *Development of a high-powered tuneable laser system for spectroscopic studies of trace elements and positronium.* PhD thesis, University of Wales Swansea, 2005.

[31] J. Estrada, T. Roach, J. N. Tan, P. Yesley, and G. Gabrielse, "Field ionization of strongly magnetized rydberg positronium: A new physical mechanism for positron accumulation," *Phys. Rev. Lett.*, vol. 84, pp. 859–862, Jan 2000.

[32] C. J. Baker, D. P. van der Werf, D. C. S. Beddows, P. R. Watkeys, C. A. Isaac, S. J. Kerrigan, M. Charlton, and H. H. Telle, "Weakly bound positron-electron pairs in a strong magnetic field," *Journal of Physics B: Atomic, Molecular and Optical Physics*, vol. 41, no. 24, p. 245003, 2008.

[33] B. M. Jelenković, A. S. Newbury, J. J. Bollinger, W. M. Itano, and T. B. Mitchell, "Sympathetically cooled and compressed positron plasma," *Phys. Rev. A*, vol. 67, p. 063406, Jun 2003.

[34] M. Amoretti, C. Amsler, G. Bazzano, G. Bonomi, A. Bouchta, P. D. Bowe, C. Canali, C. Carraro, C. L. Cesar, M. Charlton, M. Doser, A. Fontana, M. C. Fujiwara, R. Funakoshi, P. Genova, J. S. Hangst, R. S. Hayano, I. Johnson,

L. V. Jørgensen, A. Kellerbauer, V. Lagomarsino, R. Landua, E. L. Rizzini, M. Macr, N. Madsen, G. Manuzio, M. Marchesotti, D. Mitchard, F. Ottone, H. Pruys, C. Regenfus, P. Riedler, A. Rotondi, G. Testera, A. Variola, L. Venturelli, Y. Yamazaki, D. P. van der Werf, and N. Zurlo, "Antihydrogen production temperature dependence," *Physics Letters B*, vol. 583, no. 1-2, pp. 59 – 67, 2004.

[35] H. F. Powell, D. M. Segal, and R. C. Thompson, "Axialization of laser cooled magnesium ions in a penning trap," *Phys. Rev. Lett.*, vol. 89, p. 093003, Aug 2002.

[36] J. Clarke, *The generation and manipulation of low energy positrons.* PhD thesis, University of Wales Swansea, 2005.

[37] K. F. Canter, P. G. Coleman, T. C. Griffith, and G. R. Heyland, "Measurement of total cross sections for low energy positron-helium collisions. (positron backscattering from metal surface)," *Journal of Physics B: Atomic and Molecular Physics*, vol. 5, no. 8, p. L167, 1972.

[38] A. Vehanen, K. G. Lynn, P. J. Schultz, and M. Eldrup, "Improved slow-positron yield using a single crystal tungsten moderator," *Applied Physics A: Materials Science and Processing*, vol. 32, pp. 163–167, 1983.

[39] E. M. Gullikson and A. P. Mills, "Positron dynamics in rare-gas solids," *Phys. Rev. Lett.*, vol. 57, pp. 376–379, Jul 1986.

[40] J. A. P. Mills and E. M. Gullikson, "Solid neon moderator for producing slow positrons," *Applied Physics Letters*, vol. 49, no. 17, pp. 1121–1123, 1986.

[41] K. G. Lynn, E. Gramsch, S. G. Usmar, and P. Sferlazzo, "Development of a cone-geometry positron moderator," *Applied Physics Letters*, vol. 55, no. 1, pp. 87–89, 1989.

[42] R. Khatri, M. Charlton, P. Sferlazzo, K. G. Lynn, J. A. P. Mills, and L. O. Roellig, "Improvement of rare-gas solid moderators by using conical geometry," *Applied Physics Letters*, vol. 57, no. 22, pp. 2374–2376, 1990.

[43] Proxitronic, *Phosphor Screens.* online manual.

[44] L. S. Brown and G. Gabrielse, "Geonium theory: Physics of a single electron or ion in a penning trap," *Rev. Mod. Phys.*, vol. 58, pp. 233–311, Jan 1986.

[45] G. Gabrielse, X. Fei, K. Helmerson, S. L. Rolston, R. Tjoelker, T. A. Trainor, H. Kalinowsky, J. Haas, and W. Kells, "First capture of antiprotons in a penning trap: A kiloelectronvolt source," *Phys. Rev. Lett.*, vol. 57, pp. 2504–2507, Nov 1986.

[46] G. Gabrielse, X. Fei, L. A. Orozco, R. L. Tjoelker, J. Haas, H. Kalinowsky, T. A. Trainor, and W. Kells, "Thousandfold improvement in the measured antiproton mass," *Phys. Rev. Lett.*, vol. 65, pp. 1317–1320, Sep 1990.

[47] R. S. Van Dyck, P. B. Schwinberg, and H. G. Dehmelt, "New high-precision comparison of electron and positron g factors," *Phys. Rev. Lett.*, vol. 59, pp. 26–29, Jul 1987.

[48] J. R. Sapirstein, E. A. Terray, and D. R. Yennie, "Radiative-recoil corrections to muonium and positronium hyperfine splitting," *Phys. Rev. D*, vol. 29, pp. 2290–2314, May 1984.

[49] W. Neuhauser, M. Hohenstatt, P. E. Toschek, and H. Dehmelt, "Localized visible Ba^+ mono-ion oscillator," *Phys. Rev. A*, vol. 22, pp. 1137–1140, Sep 1980.

[50] F. J. Grieman, B. H. Mahan, and A. O'Keefe, "The laser induced fluorescence spectrum of trapped CD^+," *The Journal of Chemical Physics*, vol. 72, no. 7, pp. 4246–4247, 1980.

[51] J. Clarke, D. P. van der Werf, M. Charlton, D. Beddows, B. Griffiths, and H. H. Telle, "Developments in the trapping and accumulation of slow positrons using the buffer gas technique," *Non-neutral plasma physics V: Workshop on Non-Neutral Plasmas*, vol. 692, no. 1, pp. 178–183, 2003.

[52] R. G. Greaves and J. Moxom, "Design and performance of a trap-based positron beam source," *Non-neutral plasma physics V: Workshop on Non-Neutral Plasmas*, vol. 692, no. 1, pp. 140–148, 2003.

[53] T. J. Murphy and C. M. Surko, "Positron trapping in an electrostatic well by inelastic collisions with nitrogen molecules," *Phys. Rev. A*, vol. 46, pp. 5696–5705, Nov 1992.

[54] J. Clarke, D. P. van der Werf, B. Griffiths, D. C. S. Beddows, M. Charlton, H. H. Telle, and P. R. Watkeys, "Design and operation of a two-stage positron accumulator," *Review of Scientific Instruments*, vol. 77, no. 6, p. 063302, 2006.

[55] R. G. Greaves and C. M. Surko, "Positron trapping and the creation of high-quality trap-based positron beams," *Nuclear Instruments and Methods in Physics Research Section B: Beam Interactions with Materials and Atoms*, vol. 192, no. 1-2, pp. 90 – 96, 2002.

[56] J. D. Jackson, *Classical Electrodynamics.* Wiley, 1999.

[57] J. Estrada, *Cold Trapped Positrons and Progress to Cold Antihydrogen.* PhD thesis, Massachusetts Institute of Technology, 2002.

[58] J. Randell, D. Field, S. L. Lunt, G. Mrotzek, and J. P. Ziesel, "Low-energy electron scattering by SF_6," *Journal of Physics B: Atomic, Molecular and Optical Physics*, vol. 25, no. 12, p. 2899, 1992.

[59] J. P. Marler and C. M. Surko, "Systematic comparison of positron- and electron-impact excitation of the ν_3 vibrational mode of CF_4," *Phys. Rev. A*, vol. 72, p. 062702, Dec 2005.

[60] J. Marler, G. Gribakin, and C. Surko, "Comparison of positron-impact vibrational excitation cross sections with the born-dipole model," *Nuclear Instruments and Methods in Physics Research Section B: Beam Interactions with Materials and Atoms*, vol. 247, no. 1, pp. 87 – 91, 2006. Low-Energy Positron and Positronium Physics - Proceedings of the XIII International Workshop on Low-Energy Positron and Positronium Physics.

[61] M. Charlton and J. Humberston, *Positron Physics.* Cambridge University Press, 2001.

[62] A. Kellerbauer, M. Amoretti, G. Bonomi, P. D. Bowe, C. Canali, C. Carraro, C. L. Cesar, M. Charlton, M. Doser, A. Fontana, M. C. Fujiwara, R. Funakoshi, P. Genova, R. S. Hayano, I. Johnson, L. V. Jørgensen, V. Lagomarsino, R. Landua, E. Lodi Rizzini, M. Macrí, N. Madsen, D. Mitchard, P. Montagna, L. G. C. Posada, A. Rotondi, G. Testera, A. Variola, L. Venturelli, D. P. van der Werf, Y. Yamazaki, and N. Zurlo, "Sideband cooling of ions in a non-neutral buffer gas," *Phys. Rev. A*, vol. 73, p. 062508, Jun 2006.